

School of Science
Department of Physics and Astronomy
Master Degree in Physics

Magnetic Resonance Fingerprinting (MRF) for low field NMR: preliminary study

Supervisor:
Prof.ssa Claudia Testa

Submitted by:
Giovanni Vito Spinelli

Co-supervisor:
Dr. Leonardo Brizi
Dr. Marco Barbieri

Academic Year 2019/2020

Contents

Introduction	1
1 Theoretical Background	3
1.1 Nuclear Magnetic Resonance (NMR)	3
1.1.1 Resonance condition	3
1.1.2 Nuclear spin magnetization	7
1.1.3 NMR signal and relaxation	9
1.2 NMR in Inhomogeneous Fields	14
1.2.1 Evolution of the magnetization during a pulse sequence	15
1.2.2 General evolution of \mathbf{M} : separation into coherence pathways	17
1.2.3 Numerical Derivation of the NMR Signal	21
1.2.4 Investigating the spatial distributions of inhomogeneous fields	23
1.3 Magnetic Resonance Fingerprinting: State of Art	27
1.3.1 Acquisition	29
1.3.2 Dictionary	33
1.3.3 Pattern Recognition	34
1.3.4 Final considerations	36
2 Materials and Methods	39
2.1 Experimental Approach	40
2.1.1 NMR Apparatus	40
2.1.2 NMR Sequences	47
2.1.3 Samples Analyzed	58
2.2 Simulation Approach	58
2.2.1 MARSS program	59
2.3 Data Analysis	62
2.3.1 UpenWin software	62
2.3.2 Double-Angle Method	64
2.3.3 Fourier Transform	65
2.3.4 $B_0 - B_1$ Correlation Map - 2D FFT	66
2.3.5 Creating a LUT for the simulations	70
2.3.6 Signal comparison with RMSE	71

3 Results and Discussion	73
3.1 First tests and sequences validation	74
3.1.1 B_0 off-resonance distribution	75
3.1.2 B_1 estimation using Double-Angle Method	77
3.1.3 B_1 distribution and its correlation with B_0	77
3.2 Investigating the best parameters for simulations	82
3.2.1 ANGLE Approach	83
3.2.2 Constant bSSFP	92
3.2.3 Alternate bSSFP	93
3.2.4 MRF	95
3.3 Case of study: Rubber	98
3.3.1 $B_0 - B_1$ distribution	98
3.3.2 FID 1-Pulse	100
3.3.3 Constant bSSFP	101
3.3.4 Alternate bSSFP	103
3.3.5 MRF	106
Conclusion	113
A KEA-II NMR designed sequences	117
B MARSS sequences	121
Bibliography	125

Introduction

Nuclear Magnetic Resonance (NMR) techniques are widely used in physics, chemistry, biology, and medicine because of their capacity to provide detailed information about many different material properties.

NMR procedures are usually limited to a qualitative or "weighted" analysis of a restricted set of material properties. A specific material can provide different signal behaviours depending on many factors, including experimental set up. However, NMR experiments can also provide quantitative information about material properties. In general, standard protocols give information on one single parameter at a time, and many confounding factors have to be overcome due to experimental conditions. Furthermore, a reduction in scan times is desirable. Hence, purely qualitative magnetic resonance acquisitions remain the standard today, particularly in clinical MRI [1].

Nevertheless, several attempts have been performed to develop NMR quantitative multiparametric acquisition techniques. The most promising approach is the *Magnetic Resonance Fingerprinting* (MRF). This approach was born and has been developed for clinical application, performing magnetic resonance imaging (MRI) analysis in vivo [2] with intense magnetic fields, generated by appropriate scanners and coils¹.

In this thesis work, a MRF-based sequence was developed ex novo in laboratory, using low magnetic fields, to perform an NMR quantitative multiparametric analysis in vitro.

MRF uses a pseudo randomized pulse sequences that cause the signals from different materials to have a unique signal evolution or *fingerprint* that is simultaneously a function of the multiple material properties under investigation, making the acquisition procedure faster than standard protocols. After the acquisition, a pattern recognition algorithm finds the fingerprint content within a properly created signals dictionary, and finally this is translated into quantitative measurements of magnetic parameters of interest.

The potential of this technique consists of quantitatively examine many NMR parameters simultaneously, and, in addition it reduces the acquisition time in comparison with standard protocols. Moreover, the use of pattern recognition algorithms for post-processing makes MRF robust to noise and other experimental confounding factors [2].

The aim of this work was to design an MRF-based sequence in laboratory, using low field NMR. The sequence was programmed on an NMR console, called KEA-II, which allows to control the pulse transmission and the signal acquisition by the coil using a

¹Intensity of B_0 in MRI: 0.2 – 11.7 T. Scanners widely used in clinical studies produce magnetic fields of 1.5 – 3 T [3]. Greater values are used in research.

suited software. To successfully implement MRF, preparatory NMR experiments were designed and performed. Specifically, a pulse sequence to estimate the correlation between the static magnetic field (B_0) and the radio frequency excitation field (B_1) has been implemented. This step has been fundamental because the complex evolution of the NMR signal cannot be correctly analyzed without accounting for the inhomogeneity of magnetic fields, which is not considered in clinical scanners due to high homogeneity within each voxel.

Moreover, each experimental result has been validated by means of simulations using a toolbox developed on Matlab called MARSS, which allows to simulate the magnetization evolution in an NMR experiment. Experimental NMR sequences signals were compared to the simulated ones using the RMSE metric.

In addition, to simulate the complex evolution of the NMR signal generated by a pseudo-random sequence affected by the magnetic fields inhomogeneity, it is necessary to measure the intrinsic relaxation times of the analyzed sample. This measurements was conducted performing other NMR specific sequences (the Inversion Recovery sequence and the CPMG one). The relaxation time values were derived analyzing experimental signals by the means of another specific software, called UpenWin.

In the first part of this thesis the basis of NMR theory are described. In particular a focus on NMR in inhomogeneous fields is presented to describe how the experimental conditions could affect the evolution of NMR signal. Finally, the state of art of MRF is introduced including recent techniques and their applications.

The second chapter of the thesis is dedicated to the presentation of the experimental apparatus, the simulation methods, all the NMR sequences developed, and the data analysis.

The results are reported and discussed in the third chapter. The experiments to characterize the inhomogeneities of the magnetic fields were analyzed and the resultant $B_0 - B_1$ correlation were implemented into the simulation. At the end the MRF-based sequence for low-field NMR apparatus was programmed in the dedicated console and the acquired signal was validated in comparison with the synthetic one. The thesis work demonstrates that an accurate analysis of the correlation between $B_0 - B_1$ allowed to validate each experimental result, and specifically the MRF designed sequence, which provided a correct estimate of the intrinsic relaxation times of a rubber sample. These preliminary results on the MRF technique allow to hypothesize interesting applications in the field of applied physics to medicine and to cultural heritage.

Chapter 1

Theoretical Background

1.1 Nuclear Magnetic Resonance (NMR)

Nuclear magnetic resonance (NMR) is a physical phenomenon in which nuclei in a magnetic field are perturbed by a *radio frequency pulse* and they respond by producing an electromagnetic signal with a frequency characteristic of the magnetic field on the nucleus.

This process involves nuclei that undergo energetic transitions between energy levels of angular momentum¹.

In 1938, Isidor Rabi, extending the Stern-Gerlach experiment, measured and described for the first time nuclear magnetic resonance in molecular beams [4] and for this work was awarded the Nobel Prize in Physics [5].

Currently, the term nuclear magnetic resonance refers to phenomena occurring in condensed matter, rather than in essentially non-interacting atom bundles (as for the Rabi's experiment), moreover, the term refers to phenomena in which transitions are detected by the absorbed energy by pulses of a radio-frequency field. For this reason, the first observations of the NMR phenomenon are attributable to two different groups of researchers, which conducted experiments independently one from each other in 1946: E. Purcell, H. C. Torrey and R. Pound, in Harvard, using paraffin [6] and F. Bloch, W. W. Hansen, and M. Packard, in Stanford, using water [7]. These observations led Purcell and Bloch to Nobel Prize in Physics, which they shared in 1952 [8].

1.1.1 Resonance condition

For the nuclear magnetic resonance phenomenon to occur, it is necessary that the atomic nuclei have magnetic moment, so that they can interact with a magnetic field, usually constant and homogeneous, \mathbf{B}_0 . This interaction leads to the achievement of an order between energy levels, favored by the action of the magnetic field, and counteracted by the action of thermal agitation (kT).

¹Energy in the order of thermal energy: $kT \sim 25meV$.

When an atomic nucleus interacts with an uniform and constant magnetic field, \mathbf{B}_0 , its nuclear magnetic moment, $\boldsymbol{\mu}$, tends to orient itself in the direction of the magnetic field. Hence, the external magnetic field exerts a torque on the magnetic moment:

$$\boldsymbol{\tau} = \boldsymbol{\mu} \times \mathbf{B}_0 \quad (1.1)$$

This causes the (*precession*) of $\boldsymbol{\mu}$ about the direction of the magnetic field force lines, with a precise angular frequency ν_0 , called *Larmor frequency*, which depends only on the nuclear species and on the intensity of the magnetic field \mathbf{B}_0 .

From a macroscopic point of view, this is manifested by the formation of a nuclear magnetization of equilibrium, \mathbf{M} , which it can be detected in order to find information about the system.

The detection consists in manipulating the magnetization by providing energy to the system. This energy must fulfill the *resonance condition*. With a suitable hardware system it can be possible to track the magnetization evolution during the return to equilibrium.

In a nuclear magnetic resonance experiment the measured signal, in arbitrary units, is revealed by a coil, as an electric signal induced in it by the change in magnetic flux produced by the motion of the nuclear magnetization, $\mathbf{M}(t)$ in a reference frame rotating with the resonance frequency.

Its intensity has the same units as the nuclear magnetic moment (J/T), which is proportional to the spin \mathbf{I} of the nuclear species n with spin :

$$\boldsymbol{\mu} = \gamma_n \frac{h}{2\pi} \mathbf{I} \quad (1.2)$$

where γ_n is the gyromagnetic ratio of the nuclear species n , which characterized it (its unit is MHz/T).

So in order to nuclear magnetic resonance to occur is necessary that nuclei have $\mathbf{I} \neq 0^2$.

Considering a system with a single spin, the Hamiltonian operator in quantum mechanics that corresponds to energy is $\mathbf{H}_z = -\gamma\hbar\mathbf{I}_zB_0$.

Due to the presence of an external magnetic field the *Zeeman effect* occurs, which consists of splitting or shifting of spectral lines. The energy levels are defined by the eigenvalues of the Hamiltonian operator [9]:

$$E_m = -\gamma\hbar m B_0 \quad (1.3)$$

where $-I \leq m \leq +I$.

Taking the case of hydrogens in water for example, the energy difference between the two different levels of energy, which, i.e., involves the transitions from one level to the other one, is $\Delta E = \gamma\hbar B_0$. Thus, providing to the system the energy $h\nu_0$ as electromagnetic waves in order to be equal to ΔE , the *resonance condition* (and, i.e., the *Larmor frequency*) is obtained:

$$\Delta E = \gamma\hbar B_0 = h\nu_0 = 2\pi\hbar\nu_0 = \hbar\omega_0 \quad \Rightarrow \quad \omega_0 = \gamma B_0 \quad (1.4)$$

²Nuclei most commonly used in biomedicine are e.g. 1H with spin = 1/2 and $\gamma/2\pi = 42.58 MHz/T$, ^{13}C with spin = 1/2 and $\gamma/2\pi = 10.71 MHz/T$, ^{19}F with spin = 1/2 and $\gamma/2\pi = 40.08 MHz/T$.

For example, for ${}^1\text{H}$ nuclei with $B = 1\text{T}$, $\nu = (\gamma/2\pi)B = 42.6\text{MHz}$. The frequency is in MHz , so it is the range of radio waves in the electromagnetic spectrum.

When we place a sample inside a volume of space in which a uniform magnetic field \mathbf{B}_0 is applied, it is interesting to observe how the splitting of energy levels occurs. This follows the *Boltzmann distribution*.

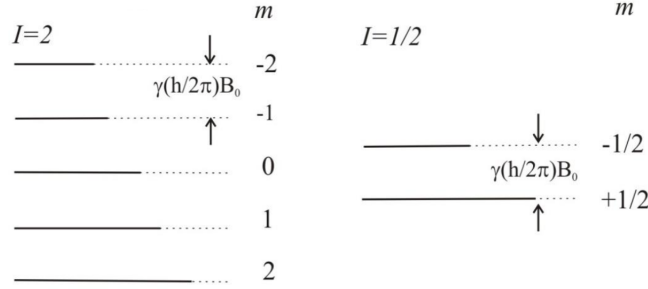


Figure 1.1: Energy level diagram for spins experiencing a Zeeman Hamiltonian. In the figure on the left $I = 2$, while in the figure on the right $I = 1/2$. The bold line schematically represents the relative population in each state for an ensemble of systems in thermal equilibrium.

Nuclei are distributed on the $2I + 1$ energy levels following the Boltzmann distribution, where the levels of minor energy are the most populated

$$\frac{n_{m-1}}{n_m} = \exp \left\{ -\frac{\hbar\omega_0}{k_B T} \right\} \quad (1.5)$$

with k_B Boltzmann's constant ($1.38 \cdot 10^{-23}$ J/K) and h the Planck's constant ($6.63 \cdot 10^{-34}$ Js). In a B_0 of magnitude of $1.5 - 2$ T (so with a frequency of 100 MHz), the exponent is in the order of 10^{-5} , i.e., $k_B T \gg \hbar\nu$ and the difference in the population of the energy levels is proportional to the magnitude of B_0 . This result is known as *Curie law*. In this condition, the nuclear spin magnetization per volume unit is a vector with the same direction and verse of \mathbf{B}_0 and with a magnitude of:

$$M_0 = N \frac{\gamma^2 \hbar^2 I(I+1)}{3k_B T} B_0 \quad (1.6)$$

This result can be obtained studying the population of the energy levels. Considering nuclei with spin $I = 1/2$ for the sake of simplicity, there are $2I + 1 = 2 \cdot \frac{1}{2} + 1 = 2$ possible states, with $m = +1/2$ (spin up) and $m = -1/2$ (spin down). The energy difference is $\Delta E = \gamma \hbar B_0$ and the populations per volume unit of the two levels are indicated as N_+ and N_- . The total number of nuclei per volume unit is $N = N_+ + N_-$, which are distributed following the Boltzmann distribution:

$$\frac{N_+}{N_-} = \exp \left\{ \frac{\Delta E}{kT} \right\} = \exp \left\{ \frac{\hbar\gamma B_0}{kT} \right\} \quad (1.7)$$

from which:

$$N_+ = \frac{N}{1 + \exp(-\gamma\hbar B_0/kT)} \quad N_- = \frac{N}{1 + \exp(+\gamma\hbar B_0/kT)} \quad (1.8)$$

and the equilibrium magnetization is proportional to the surplus of spins up on spins down

$$M_0 = \mu(N_+ - N_-) \quad (1.9)$$

where μ is the nuclear magnetic moment. Thus

$$M_0 = N\mu \frac{1 - \exp(-\gamma\hbar B_0/kT)}{1 + \exp(-\gamma\hbar B_0/kT)} = N\mu \tanh\left(\frac{\gamma\hbar B_0}{2kT}\right) \quad (1.10)$$

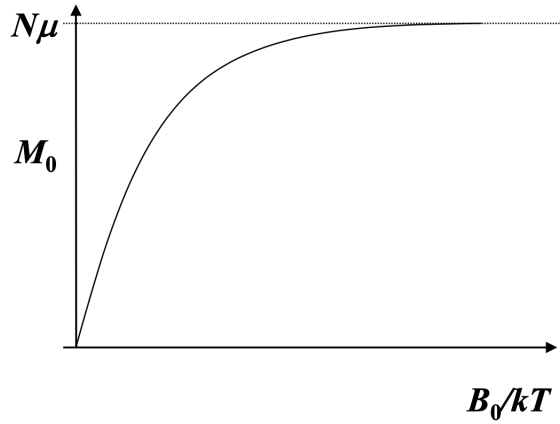


Figure 1.2: M_0 evolution.

Hence, M_0 is generally not proportional to the applied field, however the dependence on B_0/kT is linear for low magnetic fields (a condition that is always generally verified in experimental practice). For high fields, the magnetization saturates at $N\mu$, corresponding to the full orientation of all magnetic dipoles with the field. If the above condition is satisfied³, i.e.

$$\hbar\gamma B_0 \ll 2kT \quad (1.11)$$

the tanh function can be approximated at the first order:

$$M_0 = \frac{N\mu\hbar\gamma}{2kT} B_0 = \frac{N\hbar^2\gamma^2}{4kT} B_0 \quad (1.12)$$

with $\mu = \hbar\gamma I = \frac{1}{2}\hbar\gamma$. If the spin is $I = 1/2$ the Curie law becomes the Equation 1.6.

Thus, nuclei are distributed on the energy levels, occupying first the lower energy levels. An equilibrium magnetization per volume unit results, with the same direction and

³To satisfy the condition 1.11 for 1H nuclei in ambient temperature is sufficient that $B_0 < 7000T$. The condition can be not respected if the temperature is very low, in the order of mK .

verse of \mathbf{B}_0 . At the quantum level, considering the irradiation of the system with photons at the resonance condition, the absorption probability is equal to the stimulated emission probability, however, because the lowest energy level is the most populated, there is a net absorption of energy, which leads to an alteration of the equilibrium magnetization vector. All information of the system can be extracted by the return of the equilibrium of the nuclear magnetization after these alterations.

1.1.2 Nuclear spin magnetization

In an experiment, the motion of the set of spins can be described in terms of the motion of nuclear magnetization vector. The motion equation is:

$$\frac{d\mathbf{M}}{dt} = \gamma \mathbf{M} \times \mathbf{B}_0 \quad (1.13)$$

which refers to precession of \mathbf{M} about a magnetic field \mathbf{B}_0 with angular velocity $\boldsymbol{\omega}_0 = \gamma \mathbf{B}_0$.

The precession occurs when \mathbf{M} is not aligned to \mathbf{B}_0 , so, in order to move the vector \mathbf{M} and exciting the system to observe then the return of \mathbf{M} to equilibrium and to extract information about the system, a magnetic field \mathbf{B}_1 , perpendicular to \mathbf{B}_0 and oscillating to frequency ω_0 must be applied.

Considering \mathbf{B}_0 aligned to z -axis of a reference frame, if a \mathbf{B}_1 perpendicular to \mathbf{B}_0 , which precesses about z -axis with the same angular velocity of \mathbf{M} (resonance condition) is applied, \mathbf{M} is moved from equilibrium (aligned to z -axis) of an angle proportional to the time of the radio frequency pulse⁴. This angle is called *flip angle* and is equal to:

$$\alpha = \gamma B_1 t \quad (1.14)$$

This process, described in a laboratory frame, shows a precession of the nuclear spin magnetization around \mathbf{B}_0 toward xy plane with a helical shape (Figure 1.3).

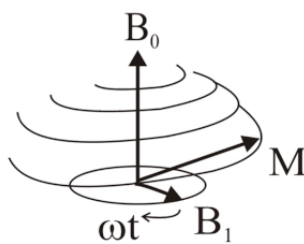


Figure 1.3: Evolution of the nuclear spin magnetization, in the laboratory frame, in the presence of a longitudinal field, \mathbf{B}_0 , and a transverse rotating field, \mathbf{B}_1 . When $\omega = \omega_0$ the magnetization vector simultaneously precesses about \mathbf{B}_0 at ω_0 and about \mathbf{B}_1 at ω_1 .

⁴The moving does not occur instantaneously, but lasts for the duration of the radio frequency pulse applied.

The M components in this frame are:

$$\begin{aligned} M_x(t) &= M_0 \sin(\omega_1 t) \sin(\omega_0 t) \\ M_y(t) &= M_0 \sin(\omega_1 t) \cos(\omega_0 t) \\ M_z(t) &= M_0 \cos(\omega_1 t) \end{aligned} \quad (1.15)$$

It is convenient to describe this system in another reference frame which rotates at Larmor frequency, where \mathbf{B}_1 is stationary, the effective longitudinal field, \mathbf{B}_0 , is zero on resonance and only the precession about \mathbf{B}_1 is apparent with angular velocity $\omega_1 = \gamma \mathbf{B}_1$ (Figure 1.4).

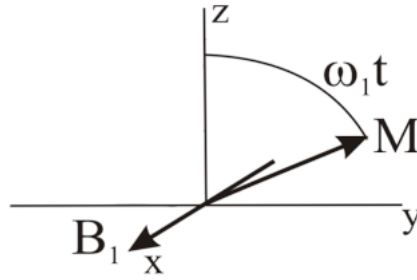


Figure 1.4: Evolution of the nuclear spin magnetization in the rotating frame.

It is important to notice that if the radio frequency pulse is off-resonance ($\omega \neq \omega_0$), in the rotating frame \mathbf{B}_0 is not completely zero and there is a residual field along z -axis equal to $\mathbf{B}_0 - \omega/\gamma$. The precession is about an effective field, \mathbf{B}_{eff} obtained as a vector sum of \mathbf{B}_1 and $\mathbf{B}_0 - \omega/\gamma$ (Figure 1.5).

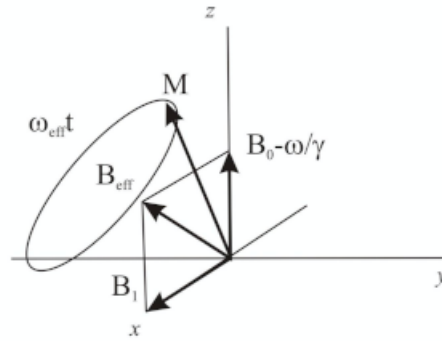


Figure 1.5: Evolution of the nuclear spin magnetization in the rotating frame after an off-resonance radio frequency pulse.

The capacity to rotate \mathbf{M} will not be optimized and maximized (i.e., not all spins of the system will be flipped with the same angle).

1.1.3 NMR signal and relaxation

The M precesses to 0 with an exponential process, so the NMR signal revealed by a coil is a damped sine wave called *Free Induction Decay (FID)*, which is proportional to the intensity of the magnetization component in the xy plane. The damping is due to the fact that, once on xy plane, the spins begin to lose phase coherence as a result of *spin-spin interactions*.

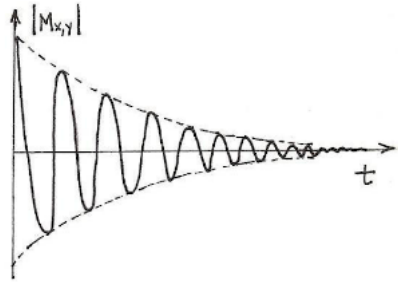


Figure 1.6: Free Induction Decay (FID).

After the radio frequency pulse, the spin system returns to *thermal equilibrium*, characterized by:

$$\begin{aligned} M_z(\text{equilibrium}) &= M_0 \\ M_{xy}(\text{equilibrium}) &= 0 \end{aligned} \quad (1.16)$$

The return to equilibrium after an excitation pulse is called relaxation and the physical processes which regulate it are different for the longitudinal component and the transverse component of magnetization. The first one is an energetic process type, where spins yield their energy to lattice, returning to thermal equilibrium, instead the second one is an entropic process type, which corresponds to decoherence of the transverse nuclear spin magnetization. The initial phase coherence of nuclear spins is lost, until the phases are eventually disordered and there is no net M_{xy} . This is due to random fluctuations of the local magnetic field which lead to random variations in the instantaneous NMR precession frequency of different spins.

Hence, for the case of longitudinal magnetization, after shutting down the radio frequency pulse, the return to equilibrium depends on velocity of the redistribution of spins on energy levels following Boltzmann distribution, so it is proportional to difference between longitudinal equilibrium magnetization and longitudinal magnetization itself and it decreases in time:

$$\frac{dM_z(t)}{dt} = -\frac{(M_z(t) - M_0)}{T_1} \quad (1.17)$$

where T_1 is the longitudinal (or spin-lattice) relaxation time, which represents the decay constant for the recovery of the z component of the nuclear spin magnetization towards its thermal equilibrium value.

Also in the case of transverse magnetization, the return to equilibrium depends on difference between the component itself and its equilibrium value (0), so in the rotating

frame:

$$\frac{dM_{xy}(t)}{dt} = -\frac{1}{T_2}M_{xy}(t) \quad (1.18)$$

where T_2 is the transverse (or spin-spin) relaxation time, which refers to the decay constant for the component of \mathbf{M} perpendicular to \mathbf{B}_0 .

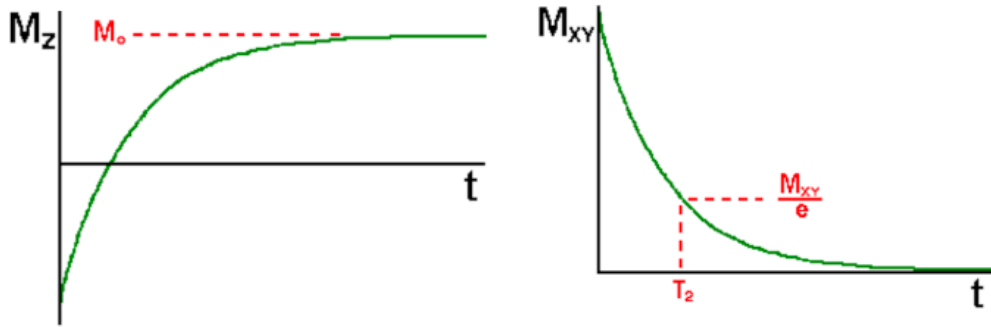
Because T_2 relaxation involves only the phase coherence loss between spins, instead T_1 relaxation involves an energy transfer and also a phase coherence loss, it's always true that $T_2 \leq T_1$.

Equations (1.17) and (1.18) are called *Bloch equations* and are used to calculate the nuclear magnetization as a function of time. The evolution of magnetization is described by the solutions of Bloch equations (shown in Figure 1.7):

$$M_z(t) = M_z(0)e^{-\frac{t}{T_1}} + M_0(1 - e^{-\frac{t}{T_1}}) \quad (1.19)$$

and

$$M_{xy}(t) = M_{xy}(0)e^{-\frac{t}{T_2}} \quad (1.20)$$



(a) If the flip angle α of the radio frequency pulse is 180° , the initial value of magnetization is $M_z(0) = -M_0$, so

$$M_z(t) = M_0(1 - 2e^{-\frac{t}{T_1}}).$$

(b) $M_{xy}(t) = M_{xy}(0)e^{-\frac{t}{T_2}}$.

Figure 1.7: Evolution of the components of the magnetization vector.

In the real case of transverse relaxation, \mathbf{B}_0 inhomogeneity contributes to dephasing, because it is not possible to have a \mathbf{B}_0 completely homogeneous in all the space of interest. This is due to slightly different local magnetic fields which lead to spins to not precess with the same frequency. And this is manifested as a loss of signal. The signal goes to 0 with a decay constant time smaller than T_2 , and the relaxation is faster. But the decoherence because of magnetic field inhomogeneity is not a true "relaxation" process. It is not random, but dependent on the location of the molecule in the magnet. For molecules that aren't moving (considering the diffusion process neglected), the deviation from ideal

relaxation is consistent over time, and the signal can be recovered by performing a specific NMR sequence⁵.

The correspondent relaxation time constant is T_2^* , which is usually smaller than T_2 and is related to it by this equation:

$$\frac{1}{T_2^*} = \frac{1}{T_2} + \frac{1}{T_{inhom}} = \frac{1}{T_2} + \gamma\Delta B_0 \quad (1.21)$$

where γ is the gyromagnetic ratio and ΔB_0 is the difference in strength of the locally varying field.

The formation of the FID is due to the application of a single pulse, but most of the sequences are based on the application of more than one pulse. The description of each sequence used for this work can be found in Section 2.1.2, but hereafter it is mentioned the generation of echo signals and it is described how the signal evolves.

Hahn Echo

Two successive radio frequency pulses produce a *spin echo* (SE) and the time between the application of the first pulse and the peak of the spin echo signal is an important NMR parameter, called *echo time* (TE). The discovery of this result came from Erwin Hahn in 1949 [10].

The spin echo represents the refocusing of spin phase information apparently lost during the decay of the FID. By the application of a second radio frequency pulse it is possible to refocus a certain dephased components of the original FID into a spin echo. This is possible because many of the T_2^* processes that produced the decay of the FID are symmetrically reversible, hence most of the signal, after the first pulse, it is not destroyed, but it becomes "disorganized" (i.e., the individual spins comprising it lose their phase coherence).

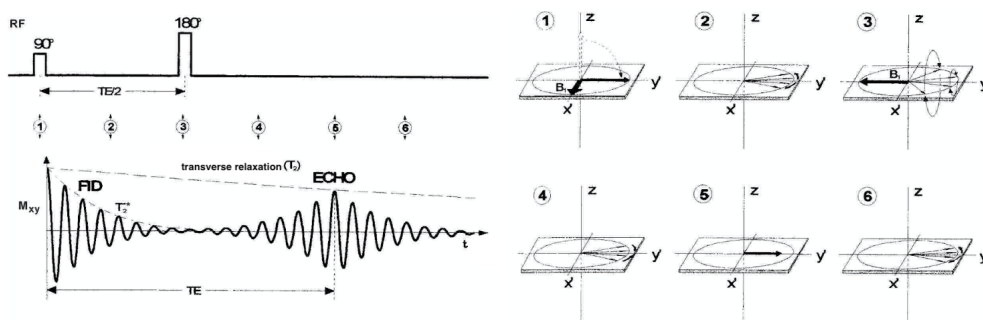


Figure 1.8: Spin echo generation.

The generation of echo is shown in Figure 1.8. It is obtained by the application of a first 90° pulse (at the Larmor frequency), which tips the magnetization vector (i.e., the individual spins comprising it) into the transverse plane (image ① in the

⁵Spin echo sequence, which is described in the paragraph below.

vector representation in Figure 1.8 (b)). At this point, as seen before, due to the local inhomogeneities in the B_0 field, some spins groups may precess faster (and gain phase) relative to others (image ② in the vector representation in Figure 1.8 (b)). Then a 180° pulse is applied which turns the entire system on its head (image ③ in the vector representation in Figure 1.8 (b)). After the flip, faster spins will be at the back of the pack. All spins become to refocus (image ④ in the vector representation in Figure 1.8 (b)) and eventually, during a *free evolution period* (i.e., period without the application of a pulse), spin at the back catch up with the slower spins. This is obtained in the center of the spin echo signal (image ⑤ in the vector representation in Figure 1.8 (b)) at the time *Echo Time* (TE), which is corresponds to the double of the time which elapses between the two radio frequency pulses. After the peak, the system once again dephases, with faster spins that leave the slower ones behind (image ⑥ in the vector representation in Figure 1.8 (b)).

It is important to notice that spin echoes are formed each time two successive radio frequency pulses of any flip angle are applied. Using pulses with flip angles specified before (90° and 180°), the resultant spin echo is called *Hahn echo*. This combination is typically the most used one because it produces the maximum possible echo signal.

Stimulated Echo

By the application of three or more pulses the generation of a *stimulated echo* (STE) is obtained.

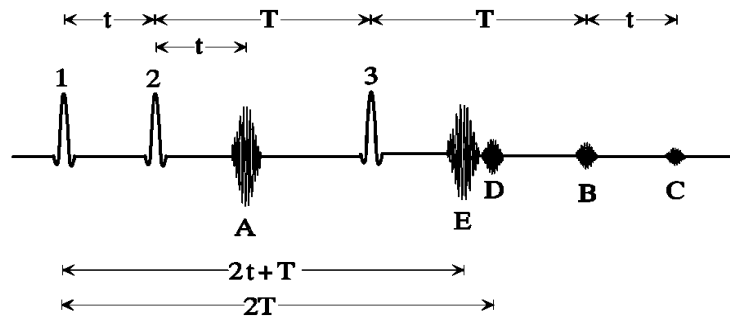


Figure 1.9: Stimulated echo generation.

In Figure 1.9 is shown a sequence based on three radio frequency pulses (1, 2 and 3) which generates five echoes (A, B, C, D and E). A, B and C are Hahn echoes, generated by each possible pair of radio frequency pulses. Specifically, echo A is generated by pulses 1 and 2, echo B is generated by pulses 2 and 3 and finally echo C is generated by pulses 1 and 3.

Echo D is called *secondary spin echo* and it is obtained by the application of the third pulse on spins of echo A. In particular, at the center peak of echo A spins in the transverse plane have once again been brought into phase. Between the center of the peak of echo A and the third pulse, these spins dephased by the T_2^* effects. Then the

third pulse flips over some of these spins, allowing them to rephase and refocus into echo *D*. The third pulse is located exactly midway between echoes *A* and *D*.

Echo *E* is the *stimulated echo* (STE). The description of how it is generated is based on a spin-phase diagram (shown in Figure 1.10), where it was considered, for the sake of simplicity, only four spins (*a*, *b*, *c* and *d*).

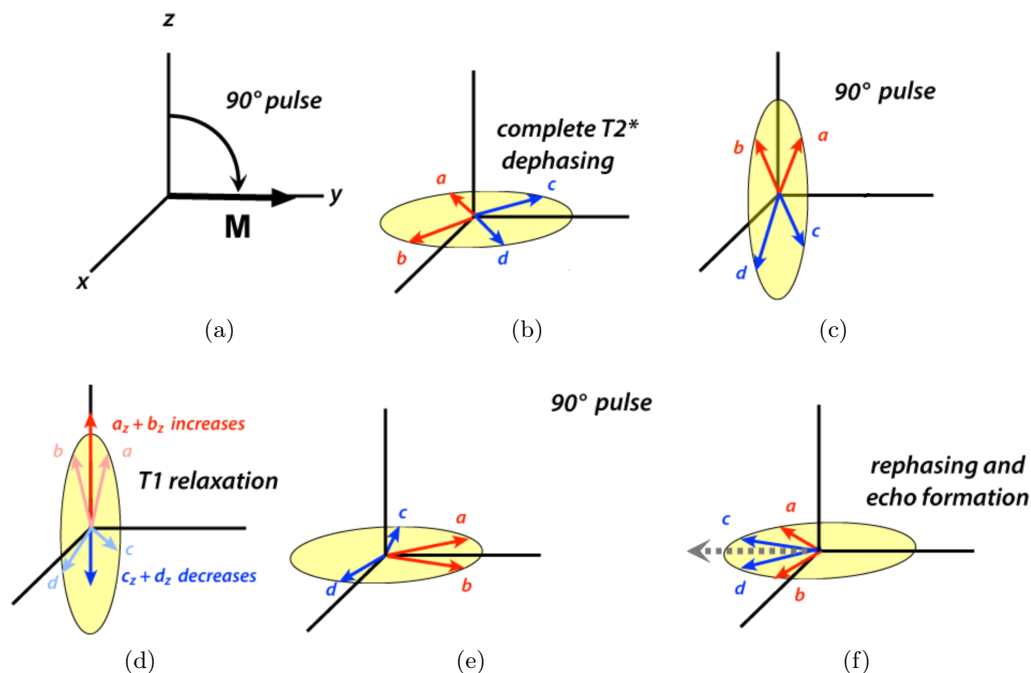


Figure 1.10: Formation of a stimulated echo after the application of three 90° pulses.

After the application of the first 90° pulse (Figure 1.10 (a)), the four spins begin to dephase on the transverse plane (Figure 1.10 (b)). Spins *b* and *d* are in local fields higher than \mathbf{B}_0 and precess faster than the Larmor frequency, gaining phase. Instead, spins *a* and *c* are in local fields lower than \mathbf{B}_0 and precess slightly slower, losing phase. Spins are selected in order to form pairs (*a*-*b* and *c*-*d*) where each element has local field offsets of the same magnitude but opposite polarities, hence they lose or gain phase correspondent to their partner at the same relative rates. The second pulse is also a 90° one and it tips the dephased spins into the vertical plane (*xz*) (Figure 1.10 (c)). It is necessary to consider only the *z*-components of the spins at this step for the stimulated echo. These components do not precess, but remain aligned around the direction of \mathbf{B}_0 . The T_1 relaxation occurs with a resulting net growth in components along the $+z$ -axis (Figure 1.10 (d)). For this reason stimulated echo have a T_1 -weighting. After the last 90° pulse, the *z*-components are flipped back into the transverse plane (*xy*) and the precession occurs (Figure 1.10 (e)). Each spin rephase along the *y*-axis and the *stimulated echo* is generated (Figure 1.10 (f)). Not all the components come into phase at exactly the same time, so the amplitude is lower and it is spread out more widely in time.

Obviously, increasing the number of the pulses lead to increase exponentially the number of echoes, e.g., for 4 radio frequency pulses the number of echoes after the last pulse is 13. The equation governing the number of echoes after the n th pulse is:

$$N_{echoes} = \frac{(3^n - 1)}{2}$$

1.2 NMR in Inhomogeneous Fields

It is useful to observe and describe how nuclear spin magnetization (and thus the signal) behaves in the presence of inhomogeneous fields. This is one of the fundamental aspect addressed in this work.

In the configuration studied in this work, low intensity fields are used and it is unrealistic to think that the analyzed samples may be affected by homogeneous fields. In fact, magnetic fields inhomogeneities can depend on many factors, such as non-ideal experimental conditions (considering devices and electronics problems) or they can arise from intrinsic magnetic susceptibility discontinuities in samples. This problem represents a hurdle for applications of high-resolution NMR.

When samples are studied in the presence of an inhomogeneous \mathbf{B}_0 field, the spectral bandwidth of the spin system easily exceeds the field intensity \mathbf{B}_1 and all radio frequency pulses act as selective pulses. The spatial dependence of both the resonance frequency and the amplitude of the radio frequency field does not make it possible to impart a uniform rotation to all excited spins, leading to a distribution of flip angles across the sample.

Considering a sequence where a first pulse is applied in order to define a 90° rotation of all spins of the sample (on-resonance condition), a 90° rotation of the magnetization in a specific part of the volume of the sample will be obtained and the magnetization in near volumes will experience an α rotation quickly departing from the desired angle. Thus, in those volumes, the longitudinal magnetization will not completely convert into transverse magnetization (assuming the pulse is applied to the sample in thermal equilibrium), i.e., a part of the magnetization will remain along the longitudinal axis. These two types of magnetization evolve in completely different ways during a subsequent free evolution period and they are referred to as different coherence pathways.

While longitudinal magnetization relaxes with T_1 and is not affected by the presence of a field gradient, transverse magnetization relaxes with T_2 and is spread out by a B_0 gradient. Moreover, whereas the transverse magnetization generated by a single pulse has a phase proportional to the phase of the pulse, the remaining longitudinal magnetization has no memory of such phase.

The dynamic of the magnetization is first described in the $\{M_x, M_y, M_z\}$ basis set. Then, a basis set more convenient is described, separating the magnetization into different coherence pathways created by the inhomogeneities.

1.2.1 Evolution of the magnetization during a pulse sequence

A nuclear magnetic resonance experiment consists in a pulse sequence that can be thought as a succession of two types of events: radio frequency pulses and free evolution periods. The results of each of these events can be represented by a rotation matrix of dimension 3×3 . Hence, the evolution of the magnetization vector and its components, $\mathbf{M}(t) = (M_x, M_y, M_z)$ under a sequence composed of n events is described by the product of n matrices:

$$\mathbf{M}(t) = \prod_{i=1}^n R_{\hat{\eta}_i}(\epsilon_i) \mathbf{M}(0) \quad (1.22)$$

where $\mathbf{M}(0) = (0, 0, M_0)$ is the equilibrium magnetization, $\mathbf{M}(t)$ is the magnetization at a time t after the application of the sequence [11]. The $R_{\hat{\eta}_i}$ refers to rotations by an angle ϵ_i about an axis $\hat{\eta}_i$. Considering the application of a B_1 field, with frequency ω_{rf} and a phase ϕ , the magnetization precesses about an effective field of amplitude

$$B_{eff} = \sqrt{B_1^2 + \Delta B_0^2} \quad (1.23)$$

which is tilted with respect to the z -axis by an angle

$$\theta = \tan^{-1}(B_1/\Delta B_0) \quad (1.24)$$

where $\Delta B_0 = B_0 - \omega_{rf}/\gamma$. A representation of the precession of the magnetization about the effective field is shown in Figure 1.11 for a radio frequency pulse with phase $\phi = \pi/2$. The effective flip angle during a pulse of duration t_p is given by:

$$\alpha_{eff} = \gamma B_{eff} t_p \quad (1.25)$$

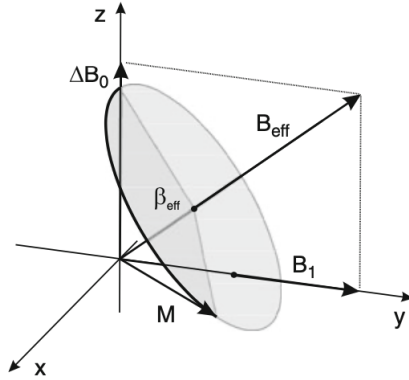


Figure 1.11: Precession of the magnetization about the effective field B_{eff} during the application of a B_1 (with phase $\pi/2$) and offset resonance $\Delta\omega_0 = \gamma\Delta B_0$.

The three components of the magnetization after the radio frequency pulse can be derived by rotating the vector about B_{eff} by α_{eff} . In this case it is convenient to change

the frame, using a local frame, where z -axis corresponds to direction and verse of B_{eff} and the x -axis lying in the plane defined by the vectors B_{eff} and B_1 . The general rotation after a radio frequency pulse with phase ϕ is given by:

$$\mathbf{A} = \begin{pmatrix} \cos(\theta) \cos(\phi) & \cos(\theta) \sin(\phi) & -\sin(\phi) \\ -\sin(\phi) & \cos(\phi) & 0 \\ \sin(\theta) \cos(\phi) & \sin(\theta) \sin(\phi) & \cos(\theta) \end{pmatrix} \quad (1.26)$$

Now that the vector is in the new basis, it is rotated by an angle α_{eff} about B_{eff} by applying the following matrix:

$$\mathbf{B} = \begin{pmatrix} \cos(\alpha_{eff}) & -\sin(\alpha_{eff}) & 0 \\ \sin(\alpha_{eff}) & \cos(\alpha_{eff}) & 0 \\ 0 & 0 & 1 \end{pmatrix} \quad (1.27)$$

At this point, applying the inverse rotation, the magnetization vector is transformed back to the original system:

$$\mathbf{A}^{-1} = \begin{pmatrix} \cos(\theta) \cos(\phi) & -\sin(\phi) & \sin(\theta) \cos(\phi) \\ \cos(\theta) \sin(\phi) & \cos(\phi) & \sin(\theta) \sin(\phi) \\ -\sin(\theta) & 0 & \cos(\theta) \end{pmatrix} \quad (1.28)$$

The total effect of radio frequency pulse is calculated as the product of these three matrices:

$$\mathbf{P} = \mathbf{A}^{-1} \mathbf{B} \mathbf{A} \quad (1.29)$$

Considering the free evolution periods, the magnetization evolves precessing about the offset field ΔB_0 with a frequency $\Delta\omega_0$ (Figure 1.12) and the components of the vector after a time τ are:

$$\mathbf{M}(t + \tau) = \mathbf{E} \mathbf{M}(t) \quad (1.30)$$

where

$$\mathbf{E} = \begin{pmatrix} e_2(\tau) \cos(\Delta\omega_0\tau) & e_2(\tau) \sin(\Delta\omega_0\tau) & 0 \\ e_2(\tau) \sin(\Delta\omega_0\tau) & e_2(\tau) \cos(\Delta\omega_0\tau) & 0 \\ 0 & 0 & e_1(\tau) \end{pmatrix} \quad (1.31)$$

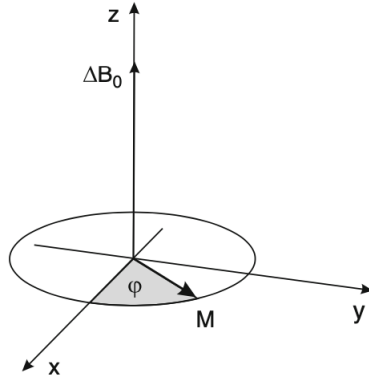


Figure 1.12: Precession about ΔB_0 during the free evolution period, which is simply a rotation about the z -axis.

The factors $e_1(\tau) = e^{-\tau/T_1}$ and $e_2(\tau) = e^{-\tau/T_2}$ describes the effects of longitudinal and transverse relaxation during the free evolution periods. These effects are typically neglected during radio frequency pulses. The e_1 factor includes T_1 attenuation, but does not take into account the magnetization created during each free evolution period. The new magnetization after a free evolution period τ can be included adding a vector $\mathbf{M}_{new}(\tau) = (0, 0, 1 - e^{-\tau/T_1})$ to the resultant magnetization at the end of the evolution period. After a free evolution period τ , the magnetization is given by $\mathbf{M}(t + \tau) = \mathbf{E}\mathbf{M}(t) + \mathbf{M}_{new}(\tau)$.

The evolution of the magnetization vector at any time of a sequence can be derived by applying the correct number of rotations to the initial vector.

The strategy to integrate the total signal response of a spin system to a particular sequence requires partitioning of the sample into small voxels where a uniform resonance frequency and RF amplitude can be defined.

1.2.2 General evolution of \mathbf{M} : separation into coherence pathways

The magnetization, once a large number of pulses (with an arbitrary phase) is applied, begin to evolve in completely different ways during a subsequent free evolution period. The longitudinal and transverse magnetization are referred to as different coherence pathways. In this general case, a description in the previous basis set is not convenient, so it is necessary to introduce another basis set, where the magnetization is split into three coherence states:

$$\begin{aligned} M_{+1} &= M_x + iM_y \\ M_{-1} &= M_x - iM_y \\ M_0 &= M_z \end{aligned} \tag{1.32}$$

The index $+1$ designates a transverse magnetization component which is defocussing during the particular period between two radio frequency pulses. The index -1 is used for the transverse component of the magnetization which is refocussing and the index 0 refers to the longitudinal magnetization component. The history of a particular component is

indicated by an appropriate array of indices [12]. Using these variables, the evolution under free precession of duration τ has only diagonal elements [13]:

$$\begin{pmatrix} M_{+1}(\tau) \\ M_{-1}(\tau) \\ M_0(\tau) \end{pmatrix} = \begin{pmatrix} e_2 e^{i\Delta\omega_0\tau} & 0 & 0 \\ 0 & e_2 e^{-i\Delta\omega_0\tau} & 0 \\ 0 & 0 & e_1 \end{pmatrix} \begin{pmatrix} M_{+1}(0) \\ M_{-1}(0) \\ M_0(0) \end{pmatrix} \quad (1.33)$$

where e_1 and e_2 are the factors which describe the attenuation by relaxation as defined previous section⁶. The matrix presents only diagonal elements, so coherence pathways are not mixed during free precession: M_{+1} and M_{-1} are multiplied by a phase term that depends on the offset frequency.

Radio frequency pulses mix in general all the states:

$$\begin{pmatrix} M_{+1}(t_p) \\ M_{-1}(t_p) \\ M_0(t_p) \end{pmatrix} = \begin{pmatrix} \Lambda_{+1,+1} & \Lambda_{+1,-1} & \Lambda_{+1,0} \\ \Lambda_{-1,+1} & \Lambda_{-1,-1} & \Lambda_{-1,0} \\ \Lambda_{0,+1} & \Lambda_{0,-1} & \Lambda_{0,0} \end{pmatrix} \begin{pmatrix} M_{+1}(0) \\ M_{-1}(0) \\ M_0(0) \end{pmatrix} \quad (1.34)$$

For a radio frequency pulse of phase ϕ and duration t_p , the matrix elements $\Lambda_{l,m}$ for an arbitrary frequency offset $\Delta\omega_0$, radio frequency field amplitude B_1 and effective nutation frequency $\Omega = \gamma B_{eff}$ are given by [13] [14]:

$$\begin{aligned} \Lambda_{+1,+1} &= \frac{1}{2} \left\{ \left(\frac{\omega_1}{\Omega} \right)^2 + \left[1 + \left(\frac{\Delta\omega_0}{\Omega} \right)^2 \right] \cos(\Omega t_p) \right\} + i \left(\frac{\Delta\omega_0}{\Omega} \right) \sin(\Omega t_p) \\ \Lambda_{0,0} &= \left(\frac{\Delta\omega_0}{\Omega} \right)^2 \left(\frac{\omega_1}{\Omega} \right)^2 \cos(\Omega t_p) \\ \Lambda_{+1,0} &= \frac{\omega_1}{\Omega} \left\{ \frac{\Delta\omega_0}{\Omega} [1 - \cos(\Omega t_p)] - i \sin(\Omega t_p) \right\} e^{+i\phi} \\ \Lambda_{0,+1} &= \frac{1}{2} \frac{\omega_1}{\Omega} \left\{ \frac{\Delta\omega_0}{\Omega} [1 - \cos(\Omega t_p)] - i \sin(\Omega t_p) \right\} e^{-i\phi} \\ \Lambda_{+1,-1} &= \frac{1}{2} \left(\frac{\omega_1}{\Omega} \right)^2 [1 - \cos(\Omega t_p)] e^{+i2\phi} \\ \Lambda_{-1,-1} &= \Lambda_{+1,+1}^* \\ \Lambda_{-1,0} &= \Lambda_{+1,0}^* \\ \Lambda_{0,-1} &= \Lambda_{0,+1}^* \\ \Lambda_{-1,+1} &= \Lambda_{+1,-1}^* \end{aligned} \quad (1.35)$$

The three states are mixed only during the application of the pulses, and, as said before, the history of a particular component is indicated by an appropriate array of numbers $q_0, q_1, q_2, \dots, q_N$, where q_k denotes the coherence after the k th pulse [12]. For example, after applying N radio frequency pulses separated by free evolution periods of duration t_k , the coherence pathways is:

$$M_{q_0, q_1, q_2, \dots, q_N} = \prod_{k=1}^N \Lambda_{q_k, q_{k-1}}^k \times \exp \left(i \Delta\omega_0 \sum_{k=1}^N q_k t_k \right) \times \exp \left(- \sum_{k=1}^N \left(\frac{q_k^2}{T_2} + \frac{1 - q_k^2}{T_1} \right) t_k \right) \quad (1.36)$$

where $q_0 = 0$ when the system is assumed to be initially in thermal equilibrium.

Each pathways depends on the phase of the radio frequency pulses via the coefficients of the matrix Λ^k that communicate the state before the k th pulse with the state after

⁶ $e_1 = e^{-\tau/T_1}$ and $e_2 = e^{-\tau/T_2}$

the pulse (e.g., if $q_{k-1} = -1$ and $q_k = +1$, the k th matrix element in the product of the equation 1.36, $\Lambda_{q_k, q_{k-1}}^k = \Lambda_{+1, -1}^k$, that depends on the phase of the k th radio frequency pulse as $e^{+i2\phi_k}$ (from equations 1.35)). A final phase factor is obtained after multiplying the Λ^k coefficients defining the pathway. This factor depends on the phase of radio frequency pulses in a characteristic way. This phase can be used to define a correct phase cycle to cancel unwanted terms. Moreover, the phase accumulated during free precession periods is simply added or subtracted depending on the sign of q_k , if during the k th interval the magnetization is stored as longitudinal magnetization $q_k = 0$ and no phase is accumulated.

The coherence pathway generates an echo if after N pulses there is time t_N when the condition $\sum_{k=1}^N q_k t_k = 0$ is fulfilled. Moreover, if the times t_k are much larger than T_2^* , the FID generated by the pulse k will be completely dephased during t_k and will not contribute to the signal detected in posterior free evolution times. When the magnetization is flipped on the transverse plane for the first time by the pulse N , the condition $\sum_{k=1}^N q_k t_k = 0$ is not fulfilled during the period T_N . It should be retained for the signal calculation during t_N , because it does generate a signal that starts dephasing after the pulse, and depending on the timing of the sequence, may interfere with the desired signal. The last member of the equation 1.36 represents the attenuation of the magnetization during the relaxation.

Moreover, all pathway have a twin pathway containing the same information, so it is not necessary to take them into account in the signal calculation and it is done by selecting from the paths generating echoes only those ending with $q_N = +1$. As a convention, only the coherence $+1$ contributes to the signal. Only the pathway where the magnetization evolves always as longitudinal magnetization ($M_{0,0,0,\dots,0}$) does not have a twin pathway. This result can be written with this relation:

$$M_{-q_0, -q_1, -q_2, \dots, -q_N} = M_{q_0, q_1, q_2, \dots, q_N}^* \quad (1.37)$$

The total signal can be derived as

$$S_{Re} + iS_{Im} = \sum_{q_1, \dots, q_{N-1}} Re(M_{q_0, q_1, q_2, \dots, +1}) + iIm(M_{q_0, q_1, q_2, \dots, +1}) \quad (1.38)$$

Now, to better understand how to proceed at the time of selecting a particular pathway it is shown, for example, a sequence with three arbitrary pulses with phases ϕ_1 , ϕ_2 and ϕ_3 respectively. Thus, pathways that generate signal during each evolution time are considered. A scheme with the coherence pathways is shown in Figure 1.13. The first pulse generates $3^1 = 3$ pathways, but as said before, only M_{+1} contributes to the signal, so the FID (FID_1) is generated only from that. Once the second pulse is applied after a time t_1 , there is a split in $3^2 = 9$ pathways. Now, to understand which pathway generates a signal during t_2 , it needs to identify the pathways with $q_2 = +1$. The possibilities are $M_{0,+1,+1}$, $M_{0,-1,+1}$ and $M_{0,0,+1}$. The first one is the magnetization flipped on the transverse plane by the first pulse, which is not affected by the second one. If $t_1 \gg T_2^*$, this pathway does not generate any signal during t_2 , because at the time the second pulse is applied, the coherence is fully dephased.

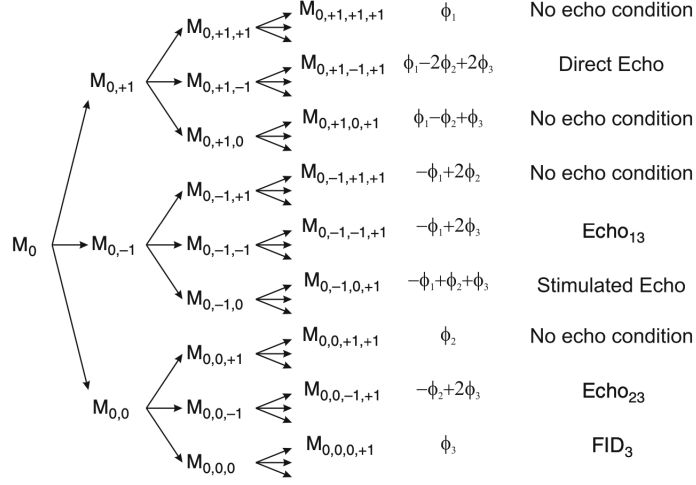


Figure 1.13: Coherence pathways generated by the application of three arbitrary pulses separated by times t_1 and t_2 .

The second pathway refers to magnetization which defocuses during t_1 and refocuses during t_2 , generating an echo. The last pathway describes the magnetization which remains along z -axis after the first pulse, but it is flipped on the transverse plane by the second one, generating a FID after the second pulse (FID_2). Last two paths interfere during t_2 and to separate them it is necessary that the phase of the pulses must be cycled. The phase of the echo for these two pathways depends on the radio frequency pulses phases as $-\phi_1 + 2\phi_2$ (from the equation 1.36). In addition, the phase of the FID_2 only depends on the phase of the second pulse as ϕ_2 ⁷.

Eventually, the last pulse splits the nine pathways in $3^3 = 27$. Nine of them end with $q_3 = +1$, but only five can generate a signal [10]. Paths which generate signal if $t_2 > t_1$ are shown in Figure 1.13, where there also is their dependence on the phases of the radio frequency pulses. The first echo, called *direct echo* (DE), is formed by the magnetization that is always in the transverse plane. The second one is formed by the magnetization which defocused during the first two evolution periods and then it refocuses during the third one (E13). The third echo is a *stimulated echo* (STE), formed by the magnetization that defocused during first free evolution period, then is stored as longitudinal magnetization during the second one and finally it refocused during t_3 after being converted in transverse magnetization by the third pulse. The fourth one is derived by the magnetization flipped on the transverse plane by the second pulse and which is refocused after the third pulse (E23). Finally, the fifth path describes a signal generated by the third pulse (FID_3). The phase cycle needed to select the stimulated

⁷To cancel FID_2 is used a phase cycle which combines two experiments where the phase of the first pulse is incremented from 0 to π . This implies that the echo changes its phase in π , but the FID_2 remains unchanged. If the receiver phase is also changed from 0 to π , the echoes are added constructively and the FID_2 s are canceled. This cycle is called *add-subtract phase cycle*.

ϕ_1	ϕ_2	ϕ_3	ϕ_{DE}	ϕ_{E13}	ϕ_{STE}	ϕ_{E23}	ϕ_{F3}	ϕ_{rec}
0	0	0	0	0	0	0	0	0
π	0	0	π	π	π	0	0	π
0	π	0	0	0	π	π	0	π
π	π	0	π	π	0	π	0	0

Table 1.1: Phase cycle to select the stimulated echo generated by a three-pulse sequence.

echo out of the five interfering signals is shown on Table 1.1. It is also shown the phase of each signal for each combination of phases chosen for the pulses. Considering that the STE has to be added constructively, the receiver phase is cycled following the phase shift of this path. The other signals are averaged out after the four scans. Changing the phase cycle it is possible to select other pathways. Using this formalism allow to us to identify interfering signals and to design phase cycles to disentangle them from the desired pathway. Moreover, it is easier to take into account of the effect by diffusion attenuation for each path. Because, if the relaxation can be easily described by both formalisms (with multiplicative factors attenuating the magnetization during the free evolution periods), to consider instead the effect of diffusion it is necessary to know the type of coherence during previous evolution periods to identify if the generated echo has evolved as a direct echo or as a stimulated one. The diffusion attenuation due to the two type of echo is different [10] and each pathways must be weighted by a different diffusion factor. This approach needs the division of a pathway into segments that form sequence of the form $(-1, +1), (-1, -1, +1, +1)$, or higher known as single, double, or higher Hahn echoes and sequence of the form $(-1, 0, \dots, 0 + 1), (-1, -1, 0, \dots, 0 + 1, +1)$ or higher, known as single, double, or higher stimulated echoes, respectively. The diffusion attenuation factor for each of these segments can be calculated once the type of echo and the timing are defined, thus the total attenuation after N pulses is the product of the attenuation factors [13][14].

The new magnetization generated during the free evolution period is not included in this calculation. The new magnetization generated during the evolution time t_k will be $\mathbf{M}^k = (0, 0, 1 - e^{-t_k/T_1})$ and it will have to be taken into account only from the $(k+1)$ th pulse on [13]. The magnetization generated in free evolution times set after the first pulse usually is eliminated by the add or subtract phase cycle of the first pulse⁸.

1.2.3 Numerical Derivation of the NMR Signal

The signal in a NMR experiment depends on the geometry of the magnet and surface coil which generate the static and radio frequency fields respectively. To calculate the total signal induced in the coil the volume is subdivided into small voxels where defined \mathbf{B}_0 and \mathbf{B}_1 can be assumed. The response is derived for every voxel using the rotations defined previously and the total value is obtained by an integration over the volume, providing a weight for each contribution of voxels given by the detection efficiency of the

⁸In sequences used to measure the T_1 this is not valid, because the magnetization generated during the evolution period subsequent to the preparation interval is the desired one.

coil. Thus it is fundamental the knowledge of the spatial distribution of both fields.

The \mathbf{B}_0 field generated by an array of permanent blocks and iron yokes can be derived by means of finite element methods (*FEM*)⁹. The \mathbf{B}_1 field instead can be obtained by the integration of the *Biot-Savart equation* for the defined coil geometry¹⁰. But this solution, which can be applied in most cases, does not take into account the possible distortion of the \mathbf{B}_1 field due to, e.g., the presence of metallic components in the vicinity of the coil. A more exact solution need the use of finite element calculations also for the coil. When both magnetic field vectors are known at every voxel, the evolution of the magnetization vector in each voxel can be calculated. Considering \mathbf{B}_0 to define the local z -axis in the voxel and because both fields may change in magnitude and direction from voxel to voxel, the component of \mathbf{B}_1 perpendicular to static field (\mathbf{B}_0): $(B_1)_{xy} = |\mathbf{B}_0 \times \mathbf{B}_1|/B_0$ is used to calculate the effect of the pulse at each voxel.

The coil excites the sample during the experiment, but also it defines the sensitivity of the sensor to detect the NMR signal from each volume element. This involves the reduction of the contribution from voxels with weak $(B_1)_{xy}$ in a twofold way: first, just part of the magnetization is flipped into the transverse plane and, second, it is detected with less efficiency. Considering the reciprocity principle [16], the contribution to the total signal from each voxel can be derived considering that the electromotive force induced in the coil by the oscillating magnetization component M_{xy} placed at r is

$$\xi = -\partial/\partial t\{(B_1/i)_{xy}M_{xy}exp(i\omega_0 t)\} \quad (1.40)$$

where the efficiency during the detection of the signal is proportional to $(B_1)_{xy}$ per unit of current. The total complex signal in the rotating frame can be obtained in arbitrary units by the integration of the contribution of the transverse magnetization $M_{xy} = M_x + iM_y$ at each voxel as

$$S(t) \propto (B_1/i)_{xy} \int_{V_s} M_{xy}(r) dr^3 \quad (1.41)$$

with the components of the magnetization that are derived at the time of the acquisition by applying to the initial magnetization $\mathbf{M}_0 = (0, 0, 1)$ the rotations that describe the NMR sequence.

⁹The FEM is a numerical method for solving partial differential equations in two or three space variables. The FEM subdivides a large system into smaller, simpler parts that are called finite elements to solve a problem. So it is performed a particular discretization in the space dimensions by the construction of a mesh of the object: the numerical domain for the solution, which has a finite number of points. The finite element method formulation of a boundary value problem finally results in a system of algebraic equations. Thus this method approximates the unknown function over the domain. The simple equations that model these finite elements are then assembled into a larger system of equations that models the entire problem. The FEM then uses variational methods from the calculus of variations to approximate a solution by minimizing an associated error function [15].

¹⁰The law of Biot-Savart in the most general case of non filiform circuits of any shape is:

$$\mathbf{B}(\mathbf{r}) = \frac{\mu_0}{4\pi} \int \int \int_V \frac{(\mathbf{J}dV) \times \mathbf{r}'}{|\mathbf{r}'|^3} \quad (1.39)$$

where \mathbf{r}' is the vector from dV to the observation point \mathbf{r} , dV is the volume element and \mathbf{J} is the current density vector in that volume.

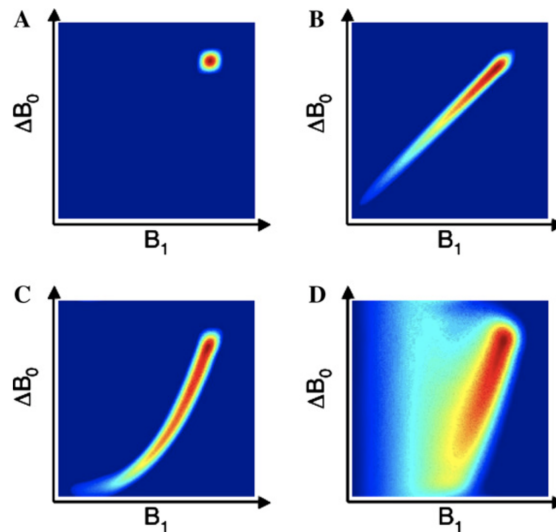


Figure 1.14: Schematic $\Delta B_0 - B_1$ field correlation functions. (A) homogeneous fields, (B) linear correlation, (C) non-linear correlation, and (D) "realistic" correlation for a single-sided system. Figure taken from the article [21].

1.2.4 Investigating the spatial distributions of inhomogeneous fields

As said before, to calculate the NMR signal is fundamental the knowledge of the spatial distribution of both fields. In addition, this will lead to a correct representation and characterization of the setup for the simulations, necessary condition to validate designed sequences. Studying the evolution of the signal in inhomogeneous fields is a problem well-known in literature for NMR spectroscopy performed with single-sided sensors [17][18][19]. However, as mentioned before, this does not represent a problem in MRI, because the high magnitude of the applied fields. But, in the case of this work, where low fields are applied, it is necessary to understand the spatial distribution and correlation between the two inhomogeneous fields.

In Figure 1.14 are shown some schematic correlations between fields. The first case (A) represents the ideal condition, which are typically achieved in standard high-field NMR experiments. It is clear that there is a very narrow correlation in both the ΔB_0 and B_1 dimensions. The second case (B) shows a narrow linear correlation and corresponds to the conditions for which the standard z -rotation pulses are effective¹¹. The last case (D) shows in a schematic way the correlation for a single-sided equipment with some, but very

¹¹Between each detected point in the FID, z -rotation pulses are applied in opposition to the phase dispersion originating from the inhomogeneous static field B_0 . The central problem for the performance of this technique is the capacity of the pulses to exactly refocus the phase dispersion induced by the static field inhomogeneity ΔB_0 . The degree of rotation depends in a controlled way on the magnitude of the field B_1 . Through spatial matching of ΔB_0 and B_1 , conditions can be achieved where the pulse z -rotation is opposed by free evolution in the inhomogeneous static field producing nutation echoes [20]. A FID-like signal is generated by repeating the z -rotation pulse and the free evolution period while recording the nutation echo maxima through stroboscopic acquisition.

broad, correlation. Achieving a perfect linear correlation with a designed experiment could be very difficult, however a non-linear correlation like the one shown in the third case (C) is not unreasonable. Many methods were proposed (e.g., tuning of the parameters of the adiabatic pulses as a means to provide refocusing even when the correlation between the fields is non-linear [22]). For this reason designing z -rotation pulses for non linear correlation it is important for the realization of a controlled NMR experiment. And the correct designing can be done understanding the correlation between the two fields, in order to correctly modify pulses and to improve the refocusing for the condition given by the sample-, magnet-, and RF-coil geometry.

In order to investigate the correlation between the two fields it is used the formalism introduced in previous sections. Considering a static field \mathbf{B}_0 applied on a system of non-interacting spin-1/2 nuclei with gyromagnetic ratio γ . A RF magnetic field \mathbf{B}_1 is used to manipulate the magnetization vector, \mathbf{M} . This field applied is in the plane perpendicular to \mathbf{B}_0 and it oscillates with a frequency ω_{RF} . The *Larmor frequency* will be $\omega_0 = -\gamma B_0$, the *frequency-offset* $\Delta\omega_0 = \omega_0 - \omega_{RF}$ and the RF amplitude will be quantified by $\omega_1 = -\gamma B_1$. The nutation frequency Ω is given by $\Omega = \sqrt{\Delta\omega_0^2 + \omega_1^2}$.

At this point, using the Cartesian formalism (the first introduced, in section 1.2.1) and recalling the rotation matrix 1.31, the free precession of the magnetization vector is described as $\mathbf{M}(t) = \mathbf{\Lambda}\mathbf{M}(0)$. With $\mathbf{\Lambda}$:

$$\mathbf{\Lambda} = \begin{pmatrix} \Lambda_{xx} & \Lambda_{xy} & \Lambda_{xz} \\ \Lambda_{yx} & \Lambda_{yy} & \Lambda_{yz} \\ \Lambda_{zx} & \Lambda_{zy} & \Lambda_{zz} \end{pmatrix} = \begin{pmatrix} \cos(\Delta\omega_0 t) & -\sin(\Delta\omega_0 t) & 0 \\ \sin(\Delta\omega_0 t) & \cos(\Delta\omega_0 t) & 0 \\ 0 & 0 & 1 \end{pmatrix} \quad (1.42)$$

in a frame rotating with the frequency of \mathbf{B}_1 (ω_{RF}) around z . Recalling the coefficients 1.35, the calculation of the Λ_{jk} of the rotation matrix for the evolution of \mathbf{M} during a pulse of length t_p and phase ϕ is given by the:

$$\begin{aligned} \Lambda_{xx} &= \frac{(\Delta\omega_0^2 \Omega^2) \cos(\Omega t_p) + \omega_1^2 \{1 + [1 - \cos(\Omega t_p)] \cos(2\phi)\}}{2\Omega^2} \\ \Lambda_{yy} &= \frac{(\Delta\omega_0^2 \Omega^2) \cos(\Omega t_p) + \omega_1^2 \{1 - [1 - \cos(\Omega t_p)] \cos(2\phi)\}}{2\Omega^2} \\ \Lambda_{zz} &= \frac{\Delta\omega_0^2 + \omega_1^2 \cos(\Omega t_p)}{\Omega^2} \\ \Lambda_{xy} &= \frac{\omega_1^2 [1 - \cos(\Omega t_p)] \sin(2\phi)}{2\Omega^2} - \frac{\Delta\omega_0 \sin(\Omega t_p)}{\Omega} \\ \Lambda_{yx} &= \frac{\omega_1^2 [1 - \cos(\Omega t_p)] \sin(2\phi)}{2\Omega^2} + \frac{\Delta\omega_0 \sin(\Omega t_p)}{\Omega} \\ \Lambda_{xz} &= \frac{\Delta\omega_0 \omega_1 [1 - \cos(\Omega t_p)] \cos(\phi)}{\Omega^2} + \frac{\omega_1 \sin(\Omega t_p) \sin(\phi)}{\Omega} \\ \Lambda_{zx} &= \frac{\Delta\omega_0 \omega_1 [1 - \cos(\Omega t_p)] \cos(\phi)}{\Omega^2} - \frac{\omega_1 \sin(\Omega t_p) \sin(\phi)}{\Omega} \\ \Lambda_{yz} &= \frac{\Delta\omega_0 \omega_1 [1 - \cos(\Omega t_p)] \sin(\phi)}{\Omega^2} - \frac{\omega_1 \sin(\Omega t_p) \cos(\phi)}{\Omega} \\ \Lambda_{zy} &= \frac{\Delta\omega_0 \omega_1 [1 - \cos(\Omega t_p)] \sin(\phi)}{\Omega^2} + \frac{\omega_1 \sin(\Omega t_p) \cos(\phi)}{\Omega} \end{aligned} \quad (1.43)$$

Again, for a sequence with N pulses and free precession periods (neglecting relaxation and diffusion), the total rotation matrix is obtained by the product of the $\mathbf{\Lambda}$ for the individual events:

$$\mathbf{\Lambda}_{tot} = \prod_{n=1}^N \mathbf{\Lambda}_n \quad (1.44)$$

In inhomogeneous fields the signal can be derived from the equation 1.41. As seen, it depend on position \mathbf{r} , so, considering a spin system with density $\rho(\mathbf{r})$, the signal detected by the coil can be written as

$$S(t) = \int w(\mathbf{r})\rho(\mathbf{r})s(\mathbf{r}, t)d\mathbf{r} \quad (1.45)$$

where $s(\mathbf{r}, t) = m_x(\mathbf{r}, t) + im_y(\mathbf{r}, t)$ and $w(\mathbf{r})$ is the weighting function mentioned in section 1.2.3 for each volume element. In the simplest case $w(\mathbf{r})$ is proportional to $B_1(\mathbf{r})$ because the reciprocity theorem [16], but it could include information about, e.g., hardware and software frequency-selective filters or separate excitation and receiver RF coils which may be necessary in order to detect signal only from regions of space where the fields are correlated [23].

Supposing that changes in ω_{RF} are small enough not to affect the value of $w(\mathbf{r})$ appreciably, the signal can be rewritten

$$S(t) = \int \int P(\omega_0, \omega_1)s(\omega_0, \omega_1, t)d\omega_0d\omega_1 \quad (1.46)$$

where

$$P(\omega_0, \omega_1) = \int w(\mathbf{r})\rho(\mathbf{r})\delta[\omega_0 - \omega_0(\mathbf{r}), \omega_1 - \omega_1(\mathbf{r})]d\mathbf{r} \quad (1.47)$$

represents the field correlation function describing the searched correlation between the two fields \mathbf{B}_0 and \mathbf{B}_1 weighted by the density of spins and by the receiver sensitivity. Delta function is the *2D Dirac function*¹².

If the sample is homogeneous, $\rho(\mathbf{r})$ is finite and constant within the region of the sample and zero elsewhere. Thus, only regions that contain sample contribute to $P(\omega_0, \omega_1)$ (from equation 1.47). The idea is to eliminate the explicit space dependence in the expression for the signal. Because, neglecting the spin motion, the NMR signal can be derived when $P(\omega_0, \omega_1)$ and the spin response as a function of ω_0 and ω_1 are known. This is obtained without precise knowledge of the spatial variation of the magnetic fields. The function $P(\omega_0, \omega_1)$ will depend on the magnet and coil design, the sample shape, and to smaller extent on the electric and magnetic properties of the sample that can distort the fields [21].

The experiment to individuate the $P(\omega_0, \omega_1)$ function could be the following: a pulse sequence where the signal is detected during t_0 under free precession in the B_0 inhomogeneity. The pulse length of the excitation pulse t_1 is incremented in the indirect

¹²Considering a D -dimensional domain \mathbb{R}^D , where $\mathbf{r} = (x_1, x_2, \dots, x_D) \in \mathbb{R}^D$ is a D -dimensional vector, the generalized *Dirac Delta function* is defined as follow:

$$\delta^D(\mathbf{r}) = \begin{cases} +\infty & \text{for } \mathbf{r} = \mathbf{0} \\ 0 & \text{for } \mathbf{r} \neq \mathbf{0} \end{cases} \quad (1.48)$$

with

$$\int_{\mathbb{R}^D} \delta^D(\mathbf{r})d^D\mathbf{r} = 1 \quad (1.49)$$

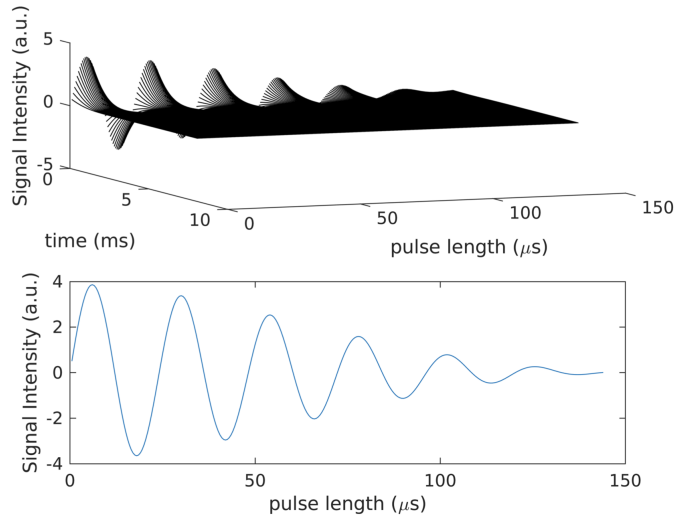


Figure 1.15: A simulation of *ANGLE* experiment. On the top is shown a 3D representation where FIDs are sampled along the *time*-axis and the t_1 or *pulse length* is incremented from $0\mu\text{s}$ to $\sim 150\mu\text{s}$. The signal intensity as a function of pulse length is on the bottom.

dimension. For each pulse length, a FID is acquired. This type of sequence is called *ANGLE* and it was used in this work to characterize the distribution of the fields and their correlation in the experiments. A more complete description of the sequence is in Section 2.1.2. A 2D scheme of the evolution of the signal sampled at each pulse length is shown in Figure 1.15. The excitation pulse generally is a *sinc*-function and the pulse has a square form¹³. With a pulse of this type, a frequency bandwidth (which should be centered in the Larmor frequency) is excited with the same amplitude.

Taking into account the off-resonance and finite RF power, the signal acquired as a function of the square excitation pulse length t_1 and the free evolution time t_0 is calculated inserting the relevant components of the rotation matrix in the equation 1.43

¹³The *Fourier Transform* of a normalized *sinc*-function $\text{sinc}(x) = \begin{cases} \frac{\sin(\pi x)}{\pi x} & \text{if } x \neq 0 \\ 1 & \text{if } x = 0 \end{cases}$ is equal to $\text{rect}(f)$:

$$\int_{-\infty}^{+\infty} \text{sinc}(t) e^{-2\pi i f t} dt = \text{rect}(f) \quad (1.50)$$

a box function which takes unit value in the interval $[-\frac{1}{2}, +\frac{1}{2}]$.

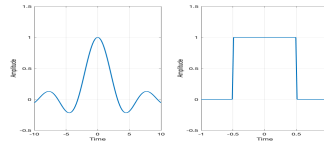


Figure 1.16: *sinc* and *rect* functions.

into equation 1.46 as

$$S(t_0, t_1) = \int \int P(\omega_0, \omega_1) \frac{\omega_1}{\Omega} \left\{ \sin(\Omega t_1) + i \frac{\Delta\omega_0}{\Omega} [1 - \cos(\Omega t_1)] \right\} e^{(i\Delta\omega_0 t_0)} d\omega_0 d\omega_1 \quad (1.51)$$

Calculating $S(t_0, t_1)$ it is possible to derive $P(\omega_0, \omega_1)$, because all the information about it are contained in $S(t_0, t_1)$. $P(\omega_0, \omega_1)$ could be calculated by assuming a grid of ω_0 and ω_1 values, and then adjust the value of $P(\omega_0, \omega_1)$ at each point using a computer algorithm until $S(t_0, t_1)$ from the equation 1.51 agrees experiment. However, a reasonable grid would contain on the order of 100×100 to 1000×1000 points and hence the same number of adjustable parameters. Obviously, this computational way is not practicable and it is necessary to reduce the number of unknowns.

If off-resonance effects can be neglected, i.e.,

$$\Delta\omega_0 \ll \omega_1 \quad (1.52)$$

the signal can be rewritten as

$$S(t_0, t_1) = \int \int P(\omega_0, \omega_1) \sin(\omega_1 t_1) e^{(i\Delta\omega_0 t_0)} d\omega_0 d\omega_1 \quad (1.53)$$

This represents the important condition that it is used in this work to derive the distribution and the correlation between magnetic fields.

In this ideal case $P(\omega_0, \omega_1)$ is determined through a *2D Fourier transform (2DFT)* of $S(t_0, t_1)$. But, if the static field inhomogeneity is on the same scale, or larger, than the maximum RF amplitude, the on-resonance condition is not fulfilled and is not possible to derive $P(\omega_0, \omega_1)$ from the *2DFT*. Performing a *2DFT* is enough to extract high resolution cross-sections or projections despite off-resonance artifacts [23][24]. The *2DFT* also provide quantitative estimates of in what $\omega_0 - \omega_1$ pairs $P(\omega_0 - \omega_1)$ is non-zero. Using the ANGLE experiment a trace of relevant $\omega_0 - \omega_1$ pairs can be extracted from the full space. This method is easier than the spatial mapping of the magnetic fields. Clearly, a more accurate determination of $P(\omega_0 - \omega_1)$ is possible using non-FT methods of data analysis, e.g., specific computational algorithm as the genetic algorithm¹⁴ or pulse sequences where the information about w_1 originates from adiabatic z -rotation pulses [26].

1.3 Magnetic Resonance Fingerprinting: State of Art

The goal of this thesis work is to investigate a *Magnetic Resonance Fingerprinting (MRF)* approach on low field devices with static magnetic field, B_0 . This technique represents an approach to data acquisition, post-processing and visualization that allows

¹⁴Genetic algorithms (GA) are randomized search algorithms developed in an effort to imitate the mechanics of natural selection. Genetic algorithms operate on string structures, like biological structures, which are evolving in time according to the rule of survival of the fittest by using a randomized yet structured information exchange (typically a specific fitness function is minimized). Thus, in every generation, a new set of strings is created, using parts of the fittest members of the old set [25].

the simultaneous non-invasive quantification of multiple important material properties (Figure 1.17).

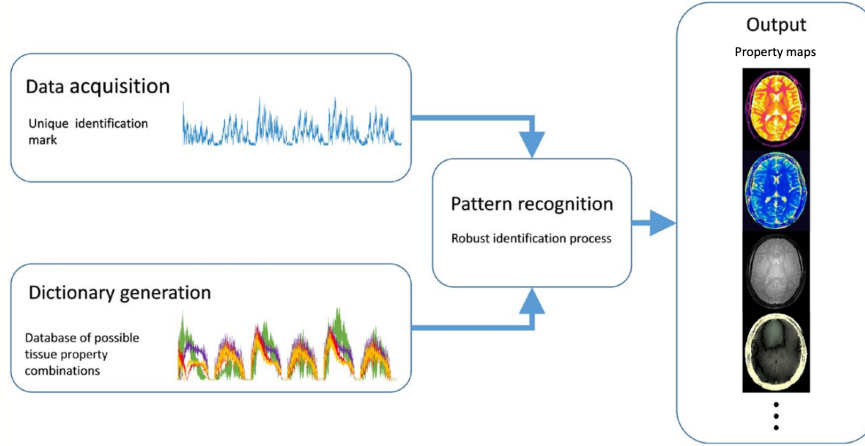


Figure 1.17: Magnetic Resonance Fingerprinting framework. Figure taken from the article [2].

Magnetic resonance fingerprinting technique is widely analyzed in literature, but its application it almost completely is on magnetic resonance imaging. This is due to the increasing interest in multiparametric quantitative imaging and to its wide-spread advantages in clinical applications.

The advantage of quantitative methods is that they provide the measure of physical properties, e.g., T_1 , T_2 , and diffusion coefficients. This leads to reduce the subjectivity. In fact, e.g., pathology results are traditionally provided by manual assessment. However, due to the complexity and heterogeneity, the manual analysis is relatively subjective and even leads to misdiagnosis [27]. This approach, due to the quantitative measurements, could provide more standardized and objective diagnosis comparing to manual inspection. Moreover, this technique could be very useful not only in diagnosis, but also for tissue characterization, follow-up, and therapeutic assessment [2]. In addition, most created methods measure a single properties at a time, but, to correctly characterize a pathology is often necessary to extract a combination of properties evaluated together [28]. Ideally, all property maps should be registered to one another. Acquiring a single tissue property involves to vary of a single acquisition parameter, keeping all others constant. Moreover, it is required that the magnetization must recover to the same initial state for each cycle, in order to keep constant the signal and avoid error in estimations. The main consequence is that times of acquisition are very long. However, different techniques were proposed to speed up the acquisition, but typically they have some problems, due to undesired tissue or system properties [29][30][31].

The MRF acquisition is made sensitive to multiple tissue properties by simultaneously varying multiple sequence parameters throughout the acquisition, such as the flip angle and phase of radio frequency pulses, the repetition time, echo time and sampling patterns. The result is a fingerprint-like signal evolution for combinations of desired tissue properties.

A *dictionary* is generated apart, containing simulated signal time courses for anticipated combinations of tissue properties using an appropriate signal model. Then, for each voxel, the fingerprint is compared with the dictionary to identify the best matching entry using pattern recognition methods and the value associated with the best dictionary match are assigned as the measured properties for that voxel. This matching give correct values even in the presence of undersampling artifacts, and allows for high acceleration factors to be used for individual time points, enabling high efficiency in the MRF acquisition [32].

Thus, MRF allows to potentially measure a wide variety of tissue properties. Moreover, there are many options for each component of the acquisition and reconstruction process. The most important ones will be described in this section.

In this work, the sequence was designed in laboratory for low field NMR, using a relaxometry apparatus which is described in the next Chapter, in Section 2.1.1. In this case, the main difference with respect the MRI devices, regards the $B_0 - B_1$ correlation. In fact, due to geometric characteristics of coils and scanners, such, e.g., the correlation between the dimensions of them, or the dimension of solenoids, or the shape of devices, the main assumption in MRI is that the influence of magnetic fields on tissues can be separately approximated as uniform in each voxel (this analysis is typically voxelwise). Obviously, there are magnetic fields inhomogeneities between adjacent voxels, and, there also are small inhomogeneities in a single voxel, because of the intrinsic magnetic susceptibility discontinuities in heterogeneous biological tissues, however, for the previous considerations, the magnetic fields can be considered homogeneous in each single voxel. Moreover, increasing the magnetic fields intensities lead to a decreasing of the dimensions of the voxel in which magnetic fields can be assumed uniform. Oldest MRI scanners were built containing long solenoids which are able to generate more homogeneous fields. Now, scanners are more compact to avoid claustrophobia problems in patients [33]. While, in the NMR case, due to the geometric characteristics of the devices used, and specifically to the correlation between the coil dimension and the sensitive volume, it is impossible to assume one single value for the B_0 and the B_1 fields in each voxel. For this main reason it was necessary to find a correct approach to estimate the $B_0 - B_1$ correlation in each voxel, using experimental sequences and simulation methods.

This type of study is a necessary starting point to extend then the sequence on single-sided NMR devices, i.e., the *MOUSE*, which has a magnet geometry which defines a flat sensitive slice with uniform gradient above the magnet's surface [34].

Before moving on to the description of the methods and materials used to carry out this study (Chapter 2), the state of the art of the MRF approach is presented in this section.

1.3.1 Acquisition

There are near-infinite possibilities for MRF-compatible pulse sequences so long as the goals of conducting an efficient experiment, in terms of signal-to-noise ratio (SNR) and scan time, and of ensuring the desired tissue properties are separable enough to be extracted with sufficient precision are satisfied [2].

The sequence implemented in the proof of principle of MRF by Ma et al. [1] is based

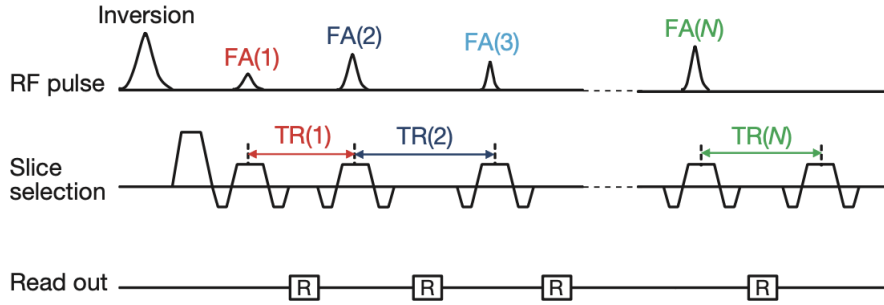


Figure 1.18: IR-bSSFP-based sequence. Figure taken from the article [2].

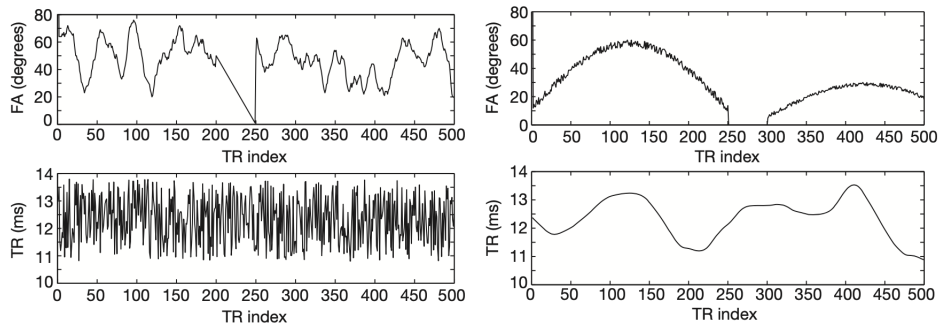


Figure 1.19: Two different flip angle and repetition times patterns. Figure taken from the article [1].

on an inversion recovery balanced steady state free precession (*IR-bSSFP*). And this also is the sequence implemented for this work. The description of these sequences can be found in Section 2.1.2. bSSFP sequence is highly suitable for MRF due to the high SNR, the high scan efficiency and the high sensitivity to T_1 , T_2 and off-resonance frequencies. The scheme of the sequence is shown in Figure 1.18. At the beginning, sequences studied used pattern with randomized value of flip angle and repetition time, like in Figure 1.19. Now, patterns are more regular, like in Figure 1.20. The expected signal evolution curves simulated for commonly tissues of the brain (white matter, grey matter, cerebrospinal fluid and fat) with the patterns in Figure 1.19 are shown in Figure 1.21, respectively. Each tissue has characteristic values of T_1 and T_2 , so each evolution of the signal describes a different shape, the fundamental assumption in MRF [1].

In imaging, these sequences are characterized by the application of magnetic field gradients in order to sample the k-space to reconstruct the image of the interest volume. The k-sampling can be done in different ways, e.g., following a Cartesian directions filling or starting from the center and going outwards in a diagonal way or in a spiral way. It is important to individuate a correct way to sample the k-space, avoiding undersampling and the creation of artifacts, exploiting symmetry for example. For example, after each

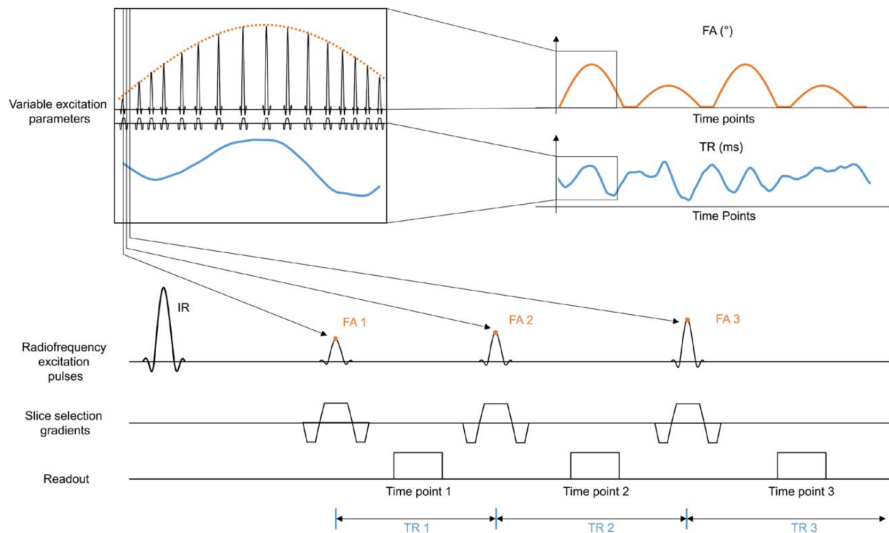


Figure 1.20: Scheme of IR-bSSFP-based sequence with more regular flip angle and repetition time patterns. Figure taken from the article [2].

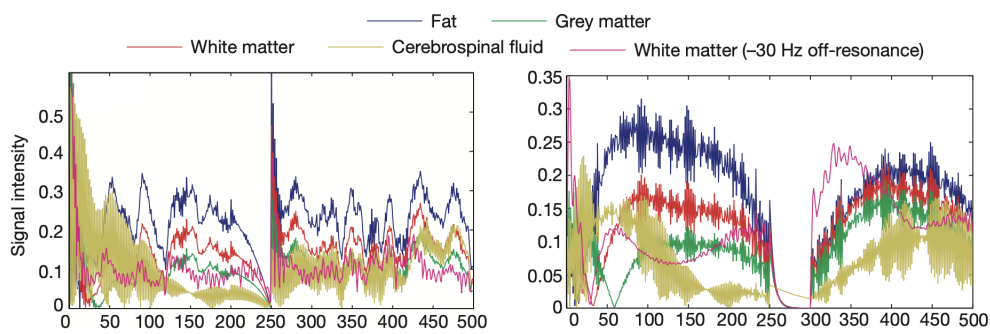


Figure 1.21: Signal evolution simulated using FA and TR patterns of Figure 1.19. Figure taken from the article [1].

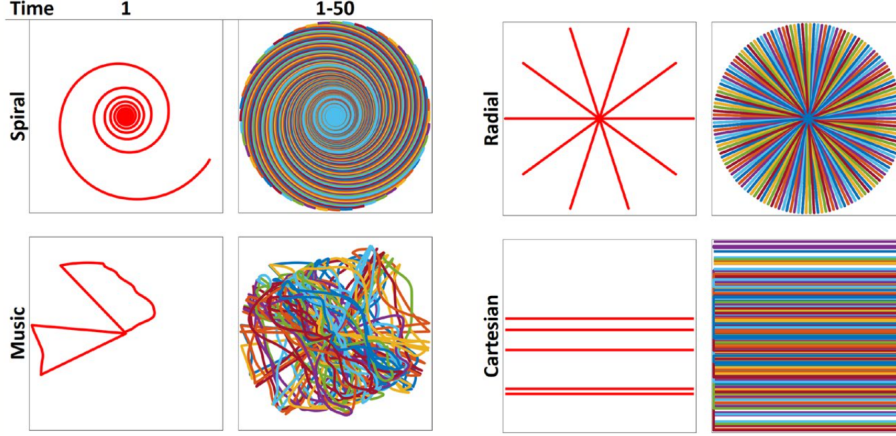


Figure 1.22: Examples of k-space sampling trajectories used by different MRF sequences: variable density *Spiral*; trajectory generated from a *Music* file (Yo Yo Ma playing Johann Sebastian Bach's Cello Suite No. 1) for the MRF-Music design; *Radial*; *Cartesian*. For each time point, the trajectory changes to generate undersampling artifacts that are incoherent with the tissues fingerprints. Figure taken from the article [2].

radio-frequency pulse in the sequence could be acquired a variable density spiral trajectory (Figure 1.22, first image) with uniform rotation ($360^\circ/48$) at each point, which allows the undersampling artifacts to have sufficient spatio-temporal incoherence.

One of the favorable properties of the bSSFP sequence is the ability to refocus spins of different off-resonance frequencies at $TE = TR/2$ in the steady state [35]. But, this characteristic could be lost due to the using of variable flip angles, variable repetition times and transient phase. An idea is to estimate TE and TR patterns based on the variable flip angle pattern, which maintains the spin echo-like refocusing characteristic of bSSFP. This work was presented by Assländer et al. [36]. The first condition on FA ensures the magnetization crosses the xz -plane at every RF pulse, without which there cannot be refocusing. TE and TR are calculated by the following equations (with initial condition $TE_0 = 0$):

$$TE_{i+1} = (TR_i - TE_i) \frac{\sin(\theta_i)}{\sin(\theta_{i+1})}$$

$$\max\{TE_{i+1}, (TR_i - TE_i)\} = \frac{\pi}{\text{bandwidth}} \quad (1.54)$$

where *bandwidth* refers to the desired bSSFP-based bandwidth in radians/second. The first equation in 1.54 exploits the property of the RF pulse to retain the Euclidean distance between the tips of the magnetization vectors of different isochromats¹⁵. Additionally, this neglects relaxation and uses the small dispersion angle approximation [36]. Using

¹⁵The word "isochromats" stands for "spins isochromats" (literally "spins of the same color") which refers to groups of individual spins that behave in a similar fashion. Since the spin isochromat represents not one (but many identical) protons, its behavior can be considered equivalent to a quantum average or expectation. The spin isochromat can therefore be treated as a macroscopic magnetization that can be analyzed according to the laws of classical electromagnetism rather than by those of quantum mechanics.

this system of equation a series of TR s that will produce a SE-like refocusing at the corresponding set of TE s for a given set of FA series is obtained [2].

However, as said before, a large number of acquisition sequences are developed to correct different possible errors. For example, in the case of banding artifacts when a wide range of off-resonant spins are present within the FOV (*field of view*) an approach based on the unbalanced SSFP was developed (*fast imaging with steady-state precision* [FISP]). Or a RF-spoiled gradient echo (GRE) based acquisition strategy, in which gradient and RF spoiling were used with an empirically chosen smooth variation of TE (range: 14 – 75ms) and the FA variation based on the FISP-MRF sequence to simultaneously measure T_1 and T_2^* [37].

1.3.2 Dictionary

The other fundamental aspect of this approach involves the dictionary. This is a sort of database containing simulated signal evolution generating by a predefined range of tissue-property combinations. Ideally, the dictionary, which is used to individuate and to assign the tissue properties to each pixel, should cover the largest possible range of physiologically relevant combinations of tissue properties, but typically, for computational reasons, a tradeoff between precision and reconstruction speed is reached [38] and the size is limited. Dictionary is generated only once for a given sequence pattern, except in cases where it needs to be dynamically adapted to the subject (e.g., cardiac or vascular fingerprinting).

The dictionary is generated by modeling the spin behavior during the acquisition [2]. Considering the bSSFP-based MRF sequences, the dictionary can be generated using the *Bloch equations* (1.17 and 1.18) [1], that model the effects of the pulses and timing of the sequence on a single isochromat resonating at a given frequency. The assumption for that approach proposed is that each voxel consists of a single isochromat. This approach using Bloch equations can also be applied to the FISP-based MRF, but with increased computation time [38]. However there is an efficient alternative consisting in extended phase graph formalism, which describes the spin system within a voxel as a discrete set of dephasing states. This is an efficient way to describe the evolution of spins affected by unbalanced gradients [39].

The dictionary generally is computed once and stored, but, as said before, there are some specific cases where it is required to compute the dictionary for each acquisition. For example, in the cardiac adaptation of MRF, the patient-specific sequence time is affected by heart rate variations and this must be taken into account and included in the dictionary, requiring that the dictionary is computed for each patient [40]. However, in the work of Hamilton et al., due to the relatively few number of properties needed for the FISP acquisition and the use of the extended phase graph formalism, only 12 seconds were needed to generate the dictionary.

1.3.3 Pattern Recognition

After acquiring and generating the dictionary the pattern recognition is used to identify the dictionary entry that best matches the tissue present in each voxel. The matching must be robust to artifacts due to undersampling and noise. A large number of reconstruction algorithms were developed, from the simplest template matching to more advanced non linear reconstructions. The main goals are to reduce aliasing artifacts (this lead to a reduction of the acquisition time and to an improvement in the accuracy in the estimated properties [36][41][42]) and to speed up the matching process [43].

Template matching

In Figure 1.23 is shown the matching approach proposed by Ma et al. [1], the template matching. The voxel fingerprint (i.e., the signal evolution of each voxel) is compared with all of the simulated fingerprints of different tissue types within the dictionary. The correlation comparison is done using the absolute value of inner product. The highest correlation represents the best match and the corresponding parameters are used for the respective location in the quantitative property maps [1]. Then, the proton density is calculated as the scaling factor between the voxel fingerprint and the corresponding unnormalized dictionary match.

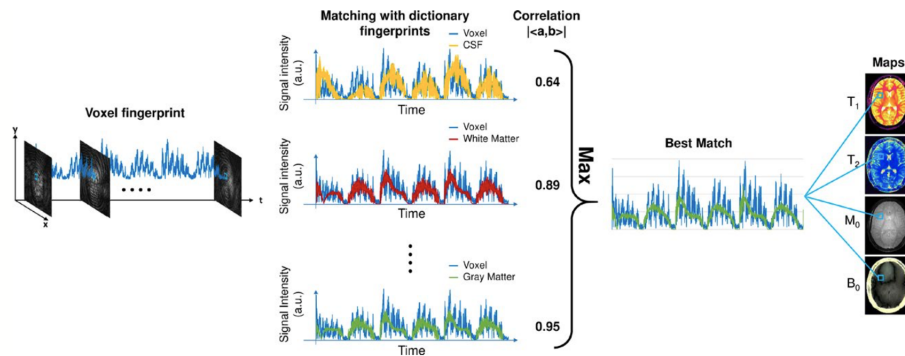


Figure 1.23: Template matching proposed in the first MRF review by Ma et al. Figure taken from the article [2].

The pattern recognition step can be programmed to be tolerant to errors. The properties of this tolerance depends on the algorithm applied. In the case of the template matching, there is a tolerance to undersampling artifacts, which are spatio-temporally incoherent and incoherent with the fingerprint time course [1]. The first incoherence as measured by the mutual coherence of the sensing matrix ensures that the signal from one pixel is not consistently bleeding to a second pixel, avoiding potential biases [44]. The second one as measured by correlation with the temporal subspace of the dictionary ensures that the combined interference from multiple locations does not appear like a tissue fingerprint. What does it really matter is the relative position as opposed to the absolute value of the metric, so the matching is tolerant to any error that lie in the

temporal null-space of the dictionary. Using this information, Ma et al. showed that the use of a single interleaf of a variable-density spiral trajectory for a single frame and the rotation of this interleaf by 7.5° from time frame to time frame generate undersampling artefacts that are temporally incoherent with the signal courses and sufficiently spatio-temporally incoherent with each other. Moreover, the template matching is tolerant to subject motion during the latter part of the acquisition, with the matching process that is still able to properly identify the tissue. If the motion occurs in the previous parts, the matching fails to reconstruct artifact-free property maps [45].

Finally, another important consideration is the assessment of the partial volume effect to quantitatively evaluate multiple components consisting of a single voxel. Supposing that the basis tissue are known a priori and only the weights for the corresponding tissue components vary from voxel to voxel across the imaging volume [1], the signal from a voxel can be calculated as

$$S_{voxel} = \sum_i D_i w_i \quad (1.55)$$

where S_{voxel} is the measured signal time course of the voxel, D_i is the signal evolution of the i th basis tissue component (generally 3 or 4 components) and w_i is the corresponding weight. The weights can be estimated by solving the equation 1.55 using the pseudoinverse to calculate for the weights [1] or a new partial volume dictionary can be generated in which atoms consist of various volume fraction combinations of signal evolutions of the basis tissue components. Thus, the volume fractions for the basis tissue components are treated as the unknown "tissue properties" instead of the underlying T_1 and T_2 . Pattern recognition is used to match the measured voxel signal with atoms of the partial volume dictionary to estimate unknown volume fractions.

Another alternative is not to assume that the basis tissue components are known a priori, so the D_i in the equation 1.55 represents the full dictionary.

To solve this highly undetermined and ill-conditioned inverse problem, McGivney et al. have proposed a Bayesian statistical framework with a sparsity-inducing prior. This approach was analyzed using numerical simulations and in vivo data [46].

Reducing matching time

An important aspect is that the property maps must be generated rapidly in clinical applications. Although template matching using the inner product is accurate, it can take several minutes to compute for a single slice, depending on dictionary size and the number of pixels [43]. A method proposed by McGivney et al. to reduce the computation time consists on the projection of the dictionary and voxel fingerprints to a lower-dimensional subspace along the time domain and on the performing the pattern matching in this lower-dimensional subspace [43]. The subspace can be determined by applying singular value decomposition (SVD) to the dictionary and using the k singular vectors associated with the largest singular values as the basis for the subspace. The selection of the subspace dimension, k , determines the tradeoff between reduction in computational time and loss of accuracy in estimated properties. This method consists in five steps: (1) SVD of the original dictionary is computed to find the singular vectors and singular values; (2) the

transformation matrix is generated using the k largest temporal singular vectors; (3) a compression of the dictionary is performed through the transformation matrix (only once); (4) the data acquired are projected to the lower-dimensional subspace using the transformation matrix; (5) pattern matching is applied on the new projected data and dictionary to estimate the tissue property maps. This method showed a reduction of time by a factor of 3.4 for bSSFP-based MRF acquisition (with $k = 200$) and a factor of 4.8 for a FISP-based MRF acquisition (with $k = 25$) with the mean error in estimated properties under 2%.

Another method to speed up the time is the fast group-matching algorithm [47]. In this method, dictionary entries are grouped based on correlation, and a representative fingerprint signal for each group was calculated based on the mean of all the atoms within the group. Once separated the dictionary, the steps performed are: (1) the correlation between the voxel fingerprint and each group's representative fingerprint is computed; (2) groups are pruned, based on relative or absolute correlation threshold; (3) SVD compression-based matching is applied on the atoms from the remaining groups to identify the voxel properties[43]. To achieve optimal reduction in computation time with minimal loss in accuracy, pruning criteria and the number of the groups are adjusted based on the dictionary. For a bSSFP-based MRF acquisition, the time for this method is smaller by about a factor greater than 10 compared with SVD compression method (for the first method 2.5s, for the second one 27s) and by about a factor greater than 70 compared with template matching (178s) with a mean relative error of the estimated tissue properties under 2%.

Obviously, factors to speed up are dependent on the MRF data, the dictionary size and the reconstruction parameters, so they can vary across different studies [2].

1.3.4 Final considerations

The MRF approach gives many degrees of freedom and a large amount of flexibility in the design of acquisition and sequence parameters, making it a challenging problem. Most of the methods described in this section were heuristically optimized. Optimization of acquisition and sequence parameters is an open question and active area of research with multiple groups focusing on the problem [2]. For example, recent works have explored optimization through improvement in incoherence of simulated dictionary fingerprints, genetic algorithm and Monte Carlo - based sequence simulations based approaches [48][49].

Another important aspect in the MRF approach is the k-space sampling. Designing the sampling trajectory is performed based on factors such as efficiency, sensitivity to systemic effects and imperfections and the spatial incoherence of undersampling artifacts. Spiral trajectories provide high k-space sampling efficiency and present spatially incoherent undersampling artifacts, but they are sensitive to gradient nonlinearities and physical effects, e.g., eddy currents. In practice, the trajectories are either separately measured or anticipated based on model and scanner specific parameters [50][51]. The Cartesian trajectory is the most stable with respect to errors due to system imperfection, but it presents the lowest spatial incoherence of undersampling artifacts and low sampling efficiency.

Finally, although MRF is a new framework, it shares similarities with other quantitative MR approaches. The few differences stand in the variation of multiple acquisition parameters to simultaneously probe multiple tissue properties, the pattern recognition and the combination of all of the subcomponents to formulate a complete framework. However, the MRF framework may not be the ideal option if the specific clinical question needs either estimation of a single property or a qualitative evaluation, as there are existing techniques that have been thoroughly optimized and validated to address these questions [2].

Chapter 2

Materials and Methods

The methods and the materials used for this work are presented in this chapter.

Firstly, an overview of the experimental setup and all devices is presented. An electromagnet is used to generate the B_0 low field and a coil is used to generate radio frequency pulses and then to detect the signal induced by the return to equilibrium of the magnetization. After a description of the JEOL device and the coil with the configuration setup of the laboratory, the KEA console is described. The console is part of the electronic of the relaxometry apparatus and it allows to control the pulse transmission and the signal acquisition by the coil. The KEA console is also connected to a PC, which allows to design all the NMR pulse sequences by the use of a specific software (Prospa). A brief mention of the programming language of the console is then reported.

Several sequences have been designed and performed in this work to analyze how to start a correct analysis on the possibility to implement a magnetic resonance fingerprinting first on low uniform field devices. The study could be extended then on single-sided devices. These sequences are: *FID-1 Pulse*, *ANGLE* to extract $\mathbf{B}_0 - \mathbf{B}_1$ distributions, *CPMG* and *Inversion Recovery* (IR) to extract T_2 and T_1 relaxation times respectively, *Balanced Steady State Free Precession* (bSSFP) both constant and alternate and, finally, the *magnetic resonance fingerprint* sequence, which is based on an *IR-bSSFP*.

Then, the two analyzed samples are described, *EDTA*¹, an aminopolycarboxylic acid and a sample of rubber, of the eraser-type.

Once implemented a sequence on the NMR console, it is necessary to validate it. A correct validation is performed comparing results obtained from experiments with the ones obtained by the simulations. To simulate all sequences *MARSS* was used, which is a program developed on Matlab by Dr. Stanislav Sykora and Dr. Marco Barbieri [52]. This program allow to simulate the NMR processes that happen in analyzed samples when a specific pulse sequence is applied to them. Thus, a description of *MARSS* and Matlab methods is specified in the second section of this chapter.

Finally, the data analysis methods are reported, including the *OpenWin*, which is the software used to extract the relaxation times of the samples, methods to analyze the

¹ $C_{10}H_{16}N_2O_8$

$B_0 - B_1$ distributions and their correlation and the metric used to compare simulations with the experiments.

2.1 Experimental Approach

An important aspect of this thesis work is the development of sequences in the laboratory and the acquisition of data. The work was carried out in the NMR laboratory in the Department of Physics and Astronomy (DIFA) of the University of Bologna.

The main laboratory devices used were: the magnet to produce the uniform magnetic field B_0 , a coil for the B_1 field that also acts as a receiver of the signal induced by the return to equilibrium of the magnetization and a compact modular console, which acts as an interface and connects a PC with the magnet and the coil.

2.1.1 NMR Apparatus

Electromagnet JEOL

The apparatus located in the NMR laboratory of the Physics and Astronomy Department of the University of Bologna, is an in-house relaxometer based on a C-60 HL electromagnet controlled by the portable console *KEA-II*. An image of the experimental setup is shown in Figure 2.1, where the electromagnet Jeol is the first device on the right. This electromagnet is made up of two solenoidal coils in which the current flows to generate the uniform B_0 . The B_0 field is perpendicular to the surface area of the coils. Measurements conducted in this work were performed at the frequency of 20.15 MHz for 1H nuclei corresponding to a $B_0 = 0.473 T$.



Figure 2.1: NMR laboratory of the Physics and Astronomy Department of the University of Bologna.

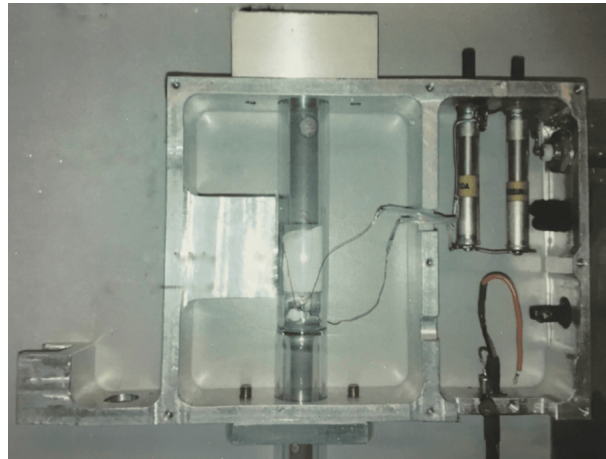


Figure 2.2: Section of the coil containing a cylindrical test tube with a rubber sample (in white in the center of the image).

The coil used to produce the radio frequency pulse and in which the signal is detected is a solenoidal coil and it is located between polar expansions of the magnet where the field has the maximum homogeneity. The coil containing the sample is shown in Figure 2.2.

Normally, the excitation field is in the order of mT , but in the KEA-II console (as for basically all NMR consoles) the actual value in mT can be tricky to detect since the pulse transmitted by the NMR console is applied with a lower value and it goes through power amplification by the electronic system.

The sensitive volume has a diameter $d = 8 \text{ mm}$ and a thickness $t = 5 \text{ mm}$, which corresponds to the dimension of the samples used placed in a cylindrical test tube.

Experimental Setup

The experimental part in the laboratory is characterized by a series of operations necessary for the correct carrying out of the acquisition. The laboratory is equipped with a cooling system connected to the electromagnet to prevent its overheating. Once the cooling system and the electromagnet are turned on, the pulse transmitter connected to the coil and the lock are turned on. This last device is a system to keep the magnetic field centered over time, with a maximum drift around 999.98 Hz . Locking is monitored by an oscilloscope, which is connected to the scanner (Figure 2.3).

The laboratory test tube containing the sample is inserted inside the coil (as shown in Figure 2.2), which is positioned between the two polar ends of the electromagnet. Moreover, the test tube is equipped with an o-ring, which serves to lock it in such a way that the sample is centered in the sensitive volume of the coil (Figure 2.4). A ruler is used to set the center of the sample between 7.2 cm and 7.4 cm , with the o-ring just above the 0 cm .

Once the sample has been inserted into the magnet, the acquisition phase is generally preceded by the hardware preparation phase. This phase is called *match and tuning* and

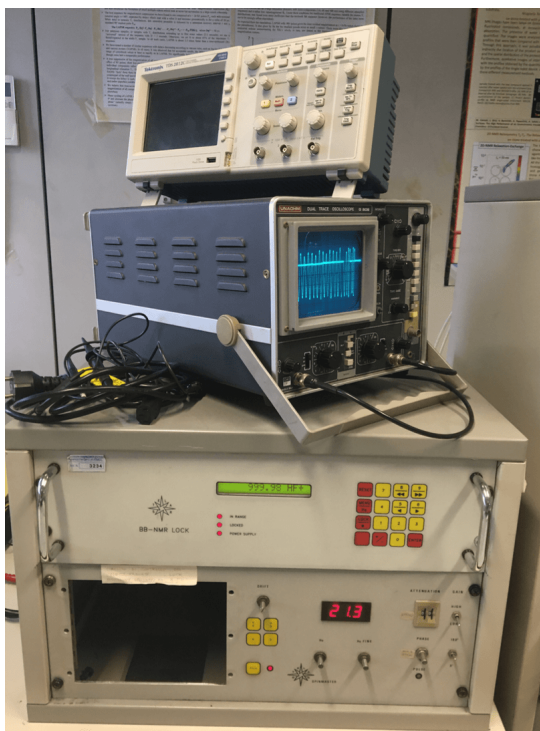


Figure 2.3: Lock device.



Figure 2.4: Rubber sample in a laboratory test tube sealing with a coating and equipped by an o-ring.

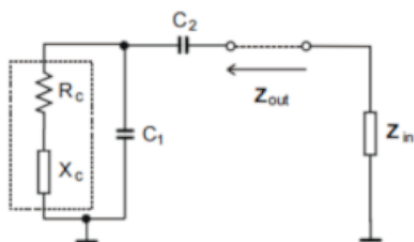


Figure 2.5: Match and tuning circuit. The capacitor in parallel modulates the tuning process, while the capacitor in series modulates the matching process.

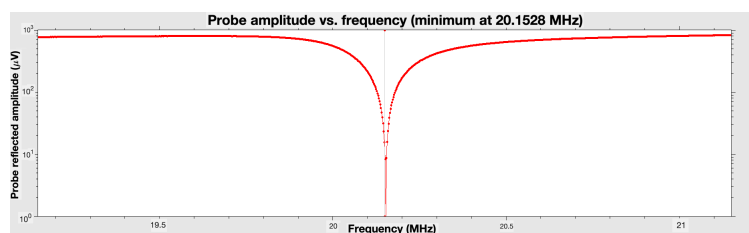


Figure 2.6: Maximum signal centered in the resonance frequency obtained with the match and tuning process.

it consists in manually adjusting the capacity of two capacitors inside a circuit (shown in Figure 2.5) in order to have the maximum acquired signal (matching).

Moreover, it is necessary to ensure that the band of excited frequencies is centered around the resonance frequency (tuning)². Subsequently, a further adjustment called *fine tuning* is generally performed using the software. This process allows to obtain an adjustment with sensitivity of the order of Hertz.

Adjustment via software is managed using the *Wobble* sequence. The optimal result that must be achieved is something similar to that shown in the Figure 2.6.

KEA - II Console

The KEA-II (Figure 2.7) is a complete NMR digital spectrometer suitable for performing a wide variety of NMR experiments. It consists of many modules all powered from a 24DC input. It is connected to the PC via USB interface and it is managed by the software. It has a very compact shape and is generally used as a console in combination with single-sided devices.

²The pulse has a limited duration in time, this means that it is not possible to excite a single frequency. The bandwidth is inversely proportional to the duration of the pulse as

$$\Delta\nu = \frac{1}{\tau} \quad (2.1)$$



Figure 2.7: KEA-II Console.

It is generally equipped with a duplexer system that consists in splitting the signals in transmission and reception on two different channels. In this way, the dead time³ is easier to manage.

The software that allows you to govern the console is called Prospa. The most interesting advantage of this console is the ability to design their own NMR sequences through the use of macros programmed with a procedural programming language based with some object oriented features.

Attenuation in voltage for pulse programming in KEA console

When a sequence is programmed, a series of suited pulses must be defined. The fundamental parameter which characterizes these pulses is the flip angle, which is equal to $B_1 \cdot t_p$, where t_p represents the pulse length of the pulse. Hence, it is possible to select a pulse length value, fixing B_1 value to define a pulse, or do the opposite.

The B_1 amplitude value in the KEA language is represented by the decreasing in power, dB (with the minus sign). This power is related to the voltage following the Ohm's law ($V = IR$, and $W = RI^2 = \frac{V^2}{R}$), and, considering the KEA electronics:

$$\left(\frac{W_{90}}{W_0}\right)_{dB} = 10 \cdot \log_{10}\left(\frac{V_{90}}{V_0}\right)^2 = 20 \cdot \log_{10}\left(\frac{V_{90}}{V_0}\right) \quad (2.2)$$

Where W corresponds to the power and V is the voltage (with the correspondent angle as subscript).

At this point, the attenuation W_x for an arbitrary angle x can be derived considering the trivial proportion $W_X : X = W_{90} : 90^\circ$:

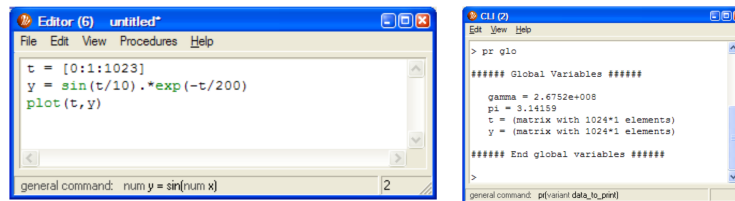
$$W_X = \left(\frac{X}{90}\right) \cdot W_{90} = 20 \cdot \log_{10}\left(\frac{X}{90}\right) + 20 \cdot \log_{10}\left(\frac{V_{90}}{V_0}\right) \quad (2.3)$$

Selecting amplitude for pulses, instead of pulse lengths, KEA console works better and programmed sequences are more robust. Because of this, the pulse series for the MRF-based sequence was designed taking into account the amplitude values to create a more robust and stable sequence. The application of these considerations is described in Section 3.3.5.

³The dead time represents the time you have to wait for the coil to discharge from the current used for the excitation in transmission, before it starts to detect the induced current in reception.

Prospa Macro Language

Prospa macro scripts are based around a number of commands, which are built in, added via the DLL (*dynamic linked library*) interface or file based commands. These macros come in two different forms: simple scripts and procedures. A script is a list of commands to be run when it is executed. The script is executed by selecting the "Run text" menu option from the editor file menu or by selecting the "Save and run text" menu option. If it has already been saved to a file, it is possible execute the script by typing the filename from the command line or main menu interface. It is not possible to pass information to and from this kind of script except via global variables.



(a) An example of a simple script executed using the run text menu option.

(b) Global variables.

Figure 2.8: First type of macro.

However all variables in this script are global and so are accessible from the command line interface. To view all visible globally defined variables, the command is `pr globals` or `pr glo` in the *CLI window*.

The second type of macro consists of procedures, i.e., lists of commands bounded by the `procedure()` and `endprocedure()` commands. To access the procedure, the name of the macro file and then the name of the relevant procedure must be typed. These two names are divided by a colon. If there is only one procedure in the file and its name matches the filename, then the filename alone is sufficient to identify the procedure. For example, in Figure 2.9, there is an edit window where there are the contents of the file "fid_sim.mac". It contains two procedures that return either a decaying cosine or sine function. To access the decaying cosine function, it can be typed:

$$(x,y) = \text{fid_sim}(1024,1,10,0.2)$$

since it is the first procedure in the file. Or, alternatively:

$$(x,y) = \text{fid_sim:cosine}(1024,1,10,0.2)$$

While the sine function is obtained with:

$$(x,y) = \text{fid_sim:sine}(1024,1,10,0.2)$$

```

Editor (5) fid_sim.mac
File Edit View Procedures Help
#####
# Generates a decaying cosine/sine function
#
# N ..... number of data point
# acqTime ... length of function in seconds
# freq ..... frequency of function in Hz
# T2 ..... 1/e point
#####
procedure (cosine,N,acqTime,freq,T2)
  x = [0:1:N-1]/N*acqTime
  pi = 3.14159
  y = cos(2*pi*freq*x) * exp(-x/T2)
endproc (x,y)
procedure (sine,N,acqTime,freq,T2)
  x = [0:1:N-1]/N*acqTime
  pi = 3.14159
  y = sin(2*pi*freq*x) * exp(-x/T2)
endproc (x,y)
general command: run y = sin(run x)

```

Figure 2.9: Edit window with the contents of the file "fid_sim.mac".

The two procedures both generate two vectors: x which contains 1024 numbers equally spaced between 0 and 1, and y , a decaying cosine or sine function with 1024 points, at 10 Hz and a T_2 of 0.2 s.

However, in practice, two type of file are necessary to implement a new sequence on KEA console. The first one is a .mac file, where the real sequence is designed. The relationships between the pulse sequence parameters and GUI parameters are defined in this script. Then, a list of commands define each pulse sequence steps, i.e., depending on the sequence, loop can be created (e.g. for the balanced sequences, where pulses with the same characteristics are repeated over time) or each pulse must be defined, as for the case of MRF sequence. In this list, pulses alternate with the acquisition windows and delays, which must also be defined in a specific way. At the end of the script the phase cycle is designed, considering the phase for pulses and also the phase of acquisition.

Once programming the .mac script, the .bak file must be designed. The easier procedure is to start from an existing one, copying and renaming it with the same name of the folder containing the .mac file of the programmed sequence. At this point, once compiled the sequence with Prospa program, the .bak file must be modified, according to the sequence of interest.

This file allows to design the GUI window. It is possible define and select what parameters can be entered in the window. In addition, it is possible to manage how and where store and save signal data. Finally, it is possible to design the plot window, selecting which data to plot. This file is the most challenging to program, because there are some specific rules to follow when different parts of the GUI window and of the experiment are defined and sometimes it can be tricky to recall some parameters or commands. Moreover, there are some parts that are always the same for different sequences, such as those that define the position inside the GUI window of the parameters to enter and the ranges of values to insert allowed.

In this thesis work 4 NMR sequences of interest were designed: an *ANGLE*, a *constant balanced steady state free precession*, an *alternate balanced steady state free precession* and an *IR-bSSFP*-based sequence for the Magnetic Resonance Fingerprinting experiment.

An example of some parts of the designed codes with their description for the MRF based sequence is reported in the appendix A while the theory of each sequence is described

in the next section.

2.1.2 NMR Sequences

This section describes all NMR sequences used in the laboratory (and then simulated with Matlab). Some of them were already designed and incorporated in the console, for others it has been necessary to program them.

When a sequence is selected, a window with 4 sections opens:

- *Pulse sequence.* In this first one it is possible to set the values related to the selected sequence. Obviously the parameters change respect to the sequence selected. For example, it is possible to select the resonance frequency (in MHz), the power of the pulse at 90° (in dB), the pulse length of the 90° pulse (in μs), the flip angle of the radio frequency pulse selected (in μs), the delay, the number of echoes, the echo shift, the number of dummy scans, and so on.
- *Acquisition.* In this second one it is possible to select the receiver phase (in degrees) and the gain (in dB), the number of points to be sampled and the dwell time (the interval between two sampled points), the number of scans (increasing the number of scans, the signal to noise ratio increases) and it is possible to choose whether or not to consider the phase cycle⁴.
- *Processing + display.* Here, in this third one, there are the two domains (time and frequency) and it is possible to correct the phase with some specific selections.
- *File settings.* Finally, in this last one section, there are all information related to the folder where files will be saved.

A screenshot example of this window is in Figure 2.10. The commands at the bottom allow to start the sequence ("Run") or open the script of the sequence to modify it, and so on.

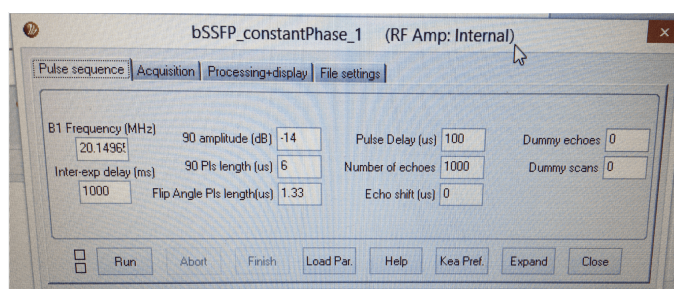


Figure 2.10: Example of the Prospra program GUI for the constant bSSFP sequence.

⁴This process involves repeating a pulse sequence with identical timings and pulse tip angles but with judicious changes to the phases of the radio frequency pulse(s) and to the routing of data to the computer memory blocks (often loosely referred to as the receiver-phase cycle). The aim in all this is for the desired signals to add coherently with time averaging whereas all other signals, whether from unwanted NMR transitions or from instrumental imperfections, cancel at the end of the cycle and do not appear in the resulting spectrum.

The first NMR sequence to be launched, once match and tuning with the *Wobble* sequence is over, is the *Pulse calibration*. In the pulse calibration sequence the sample is excited with radio frequency pulses and a FID is acquired for each pulse. The main goal of this sequence is to detect the pulse length of the pulse relative to an excitation with a flip angle of 90° . This will be useful because the subsequent sequences need this value in order to select and to control what kind of excitement is given. Hence, the sample is excited starting from a pulse length 0 (so it is acquired only noise), and with a suitable interval (generally set to $0.5 \mu s$) the pulse length is increased and each FID is acquired. The result plot shown is like the one in Figure 2.11, where it is possible to individuate where the maximum value is. In that case it corresponds to a pulse length of $6 \mu s$, i.e., a 90° pulse will correspond to a pulse length of $6 \mu s$. From this result, all values related to the other flip angles are derived, e.g., a 45° pulse will have a pulse length of $3 \mu s$ or a 30° pulse will have a pulse length of $2 \mu s$.

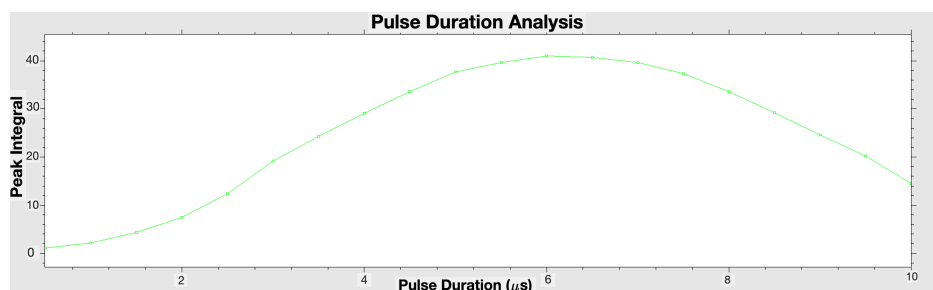


Figure 2.11: Pulse angle signal. The 90° pulse has a pulse length of $6 \mu s$. Signal obtained by a laboratory acquisition, using a rubber sample with a $T_1 = 51.7 ms$ and a $T_2 = 2.59 ms$.

Once this parameter is obtained, it is possible to start to acquire signals with more interesting sequences.

FID 1-Pulse

The FID 1-Pulse sequence is the easiest to implement, to acquire and to analyze. It consists of providing a single radio frequency pulse, generally at 90° , and acquiring the induced signal in the coil (Figure 2.12).

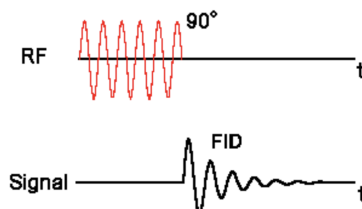


Figure 2.12: FID 90° -Pulse sequence.

As seen in the Section 1.1.3, after a radio frequency 90° pulse, the initial coherent transverse components of \mathbf{M} starts to dephase as a result of both magnetic field inhomogeneities and intrinsic T_2 mechanisms, incorporated in the concept of T_2^* -decay. The resulting signal is the FID, a damped sine wave of the following form

$$\sin(\omega_0 t) e^{-\frac{t}{T_2^*}} \quad (2.4)$$

Although it is convenient to think about an FID arising from the action of a 90° pulse, a FID will be created by a radio frequency pulse of any flip angle because some component of longitudinal magnetization is always tipped into the transverse plane (the only theoretical exception to this rule might be a 180° pulse, which in principle should only invert the longitudinal magnetization and not generate any transverse components. In practice, however, all 180° pulses are imperfect, and therefore always produce FID signals).

The acquisition of this type of signal is useful as it allows to obtain information about *off-resonance distribution*. This spectrum is obtained performing an inverse Fourier transform to the signal. A detailed description of this operation is in the section 3.1.1.

The signal obtained as a result is shown in Figure 2.13. The signal in the time domain is on the left, where the green part represents the real part, while the red one is the imaginary parts. Generally the phase is set in order to acquire the total signal on one single part, the real one, while the other is "set" to 0. On the right, the spectrum obtained by the inverse Fourier transform is shown.

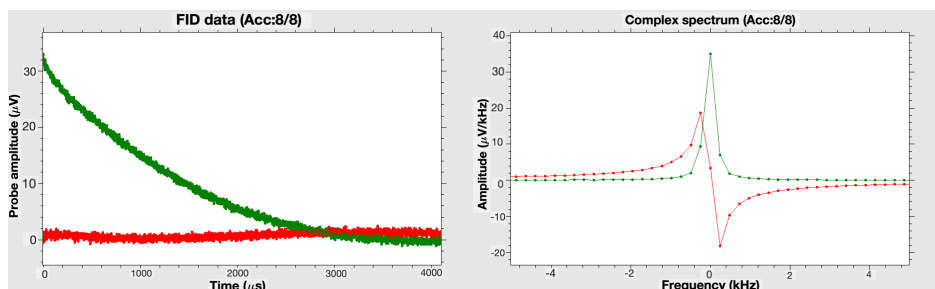


Figure 2.13: FID 1-Pulse signal on the left and its spectrum obtained performing the inverse Fourier transform on the right, from a laboratory acquisition using a rubber sample with $T_1 = 51.7 \text{ ms}$ and $T_2 = 2.59 \text{ ms}$.

ANGLE

An ANGLE experiment consists of a series of FID 1-pulse, where after each pulse a complete FID signal is acquired. The flip angle increases at each pulse, but in the practical case what changes is the pulse length, connected to the angle, following the relation 1.14, $\alpha = \gamma B_1 t_p = \omega_1 t_p$, where t_p is the pulse length and γ is the gyromagnetic ratio for the nuclei species under consideration. In our case we are interested in ^1H nuclei, so $\gamma = 267.5 \text{ MHz} \cdot \text{rad}/T$ (or $\frac{\gamma}{2\pi} = 42.58 \text{ MHz}/T$) and t_p varies starting from initial value and ending to a specific value (these values can be selected by the experimenter). At the end of ANGLE experiment two arrays are collected. In the first one the peak integral

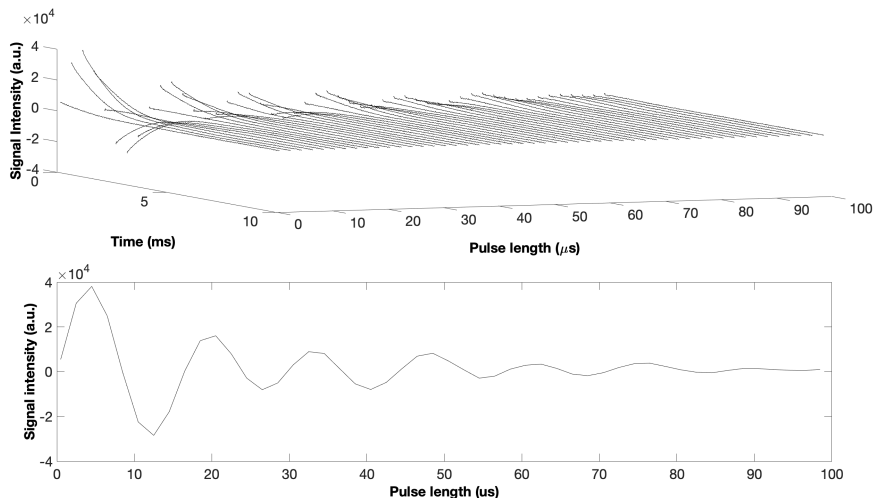


Figure 2.14: Data from a laboratory ANGLE acquisition, using a rubber sample with $T_1 = 51.7$ ms and $T_2 = 2.59$ ms, and processed with Matlab. On the top, all FIDs acquired in a 3D representation. On the bottom, the peak integral.

is shown (plotted in the down Figure 2.14), so in one column the pulse lengths for each applied radio frequency pulse are reported, while in the other column, in correspondence of each pulse length, there is the correspondent mean of the signal intensity in arbitrary units, which is calculated on the first acquired points. In the second array are collected all FIDs, so each row corresponds to one FID acquired (one for each different pulse length). It is important to notice that real and imaginary part alternate in columns. A 2D representation of data where all FIDs are plotted is in the up Figure 2.14.

This sequence is necessary to characterize the $B_0 - B_1$ correlation map, as said in section 1.2.4. These information then has been used in the simulation part to replicate the same experimental condition in order to obtain results to compare with the experimental ones. As for the single FID, applying a 2D inverse Fourier transform to the 2D data, information related to the distributions of the magnetic fields and its correlation can be extracted.

Inversion Recovery (IR)

In order to extract the value of the longitudinal time relaxation, T_1 , the required NMR sequence is the *Inversion Recovery*. Due to the perpendicular direction of B_1 respect to the direction of B_0 , it is not possible to directly acquire the signal from a return to equilibrium of the longitudinal component of the magnetization, thus each signal detected comes from the precession of the magnetization into the transverse plane.

This sequence consists of a first 180° pulse to flip the magnetization along the z -axis, giving to it a starting value of $-M_0$ (in the real case, due to the inhomogeneity of B_1 , the starting value is less, $-\eta M_0$). At this point the magnetization will start to return to

its equilibrium, passing through 0. Before it reaches the equilibrium, and after a suitable time (called *Inversion Time*, IT), a 90° pulse is applied to flip the magnetization into the transverse plane and thus measure an NMR signal. Into the xy -plane, the magnetization starts to precess and to dephase, generating a FID signal (which decays with a T_2^* decay constant).

The value to extract is the magnetization at the time $t = 0$, after the pulse applied after the inversion time (paying attention to wait a dead time needed for the coil to discharge itself from the current used to generate the radio frequency pulse, and thus, in order to start to detect the effective signal induced. Generally the dead time is around $20/25 \mu s$). A series of 64/128 FIDs are typically acquired, sequentially varying for each one the value of IT. For each of these FIDs, the value of the magnetization at the time $t = 0$ is extracted and it is reported as a function of IT. The longitudinal relaxation curve acquired is shown in Figure 2.15. First FIDs will be negative, since the magnetization moves from $-M_0$ to 0. Generally, the starting value for the inversion time is the shortest possible, and at each acquisition it increases with a fixed step (obviously all depends on the specific sample analyzed and its characteristics).

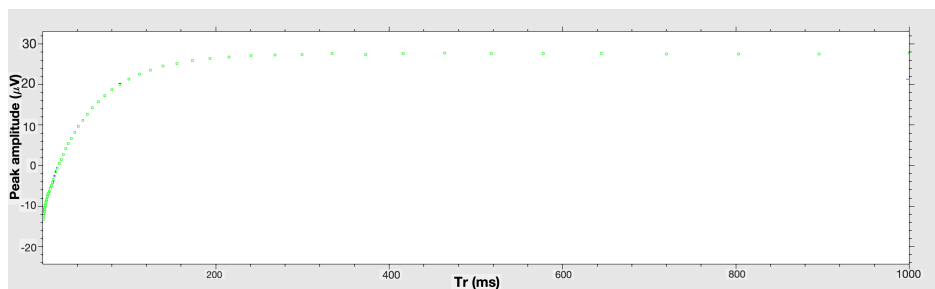


Figure 2.15: Inversion recovery signal acquired in laboratory from a rubber sample, with a $T_1 = 51.7 \text{ ms}$ and a $T_2 = 2.59 \text{ ms}$.

Obviously, after acquiring the FID, it is necessary to wait that the magnetization fully restores along the z -axis, before to re-apply the sequence, changing the inversion time. This waiting time is called *Repetition Time* (TR) and it is about $4/5$ times the value of T_1 . Thus, if the system to analyze is unknown, a longer value of TR is selected as a precautionary measure for first scans, and, once optimal values are found, you proceed with the real scans.

The evolution of the magnetization is described by the solution of the Bloch equation 1.17:

$$M_z(t) = M_z(0)e^{-\frac{t}{T_1}} + M_0(1 - e^{-\frac{t}{T_1}}) = M_0(1 - 2e^{-\frac{t}{T_1}}) \quad (2.5)$$

Considering the ideal case, where $M_z(0) = -M_0$. In the practical case, as said before, $M_z(0)$ is lower due to the B_1 inhomogeneities: $M_z(0) = -\eta M_0$. Thus

$$M_z(t) = M_0(1 - (1 + \eta)e^{-\frac{t}{T_1}}) \quad (2.6)$$

Carr-Purcell-Meiboom-Gill Sequence (CPMG)

The measurement of the relaxation time T_2 was performed with the *Carr-Purcell-Meiboom-Gill* sequence⁵ (from here on, *CPMG*).

When you study the transverse relaxation curve due to the magnetization transverse component dephasing in the xy -plane, different phenomena which contribute to phase coherence loss must be taken into account⁶. The real intrinsic T_2 , in which you typically are interested, is only related to the phase coherence loss due to *spin-spin interactions*. However, in the practical case it is not possible to obtain a perfect homogeneous \mathbf{B}_0 field, so each nucleus will experience a different local magnetic field obtained by the vector sum of the external \mathbf{B}_0 field and the local fields generated by the spin interactions. The phase coherence loss will be ruled by this inhomogeneity, which will lead to a decrease of the detected signal that will decay with a T_2^* time, instead of T_2 . Spin Echo sequence, seen in Section 1.1.3, decreases this contribution.

However, another important effect can not be neglected, especially with hydrogenate fluids: the diffusion. Any physical process that causes a molecule to move between different local environments during the course of an MR experiment can result in relaxation. The displacement might be an organized, *en masse* displacement of many molecules, as in blood or CSF flow. Or it might be an entirely random process due to microscopic diffusion, the thermally-induced displacements of molecules due to Brownian motion. If the external magnetic field through which a diffusing molecule is uniform, then the nucleus' resonance frequency will remain constant and no relaxation will occur. If the external field is not uniform, however, then the nucleus will resonate at different frequencies and develop a random phase shifts as it moves, resulting in loss of transverse coherence. Diffusion results primarily in T_2 relaxation proportional to the square of the gradient field and the length of time the spin moves within that gradient.

CPMG sequence was used because it decreases the such diffusion effects. This sequence takes the name from the initials of its designers (Carr, Purcell, Meiboom and Gill) and it consists in a first 90° pulse to move the magnetization into the xy -plane. Here, the magnetization will dephase due to the effects previous described. So, a 180° pulse on the xy -plane is applied to counteract the inhomogeneity effects after a time τ . This pulse is applied to reverse the phase angles and thus initiates rephasing. A spin echo will formed, with a peak after 2τ . Then, the signal will return to decrease. At this point, the CPMG sequence, includes other 180° pulses (pulse train), temporally divided by an echo time equal to 2τ (interval between the first 90° pulse and the first peak of the echo signal). Using a τ value as short as possible (compatible with instrumental limits), the diffusion effects decrease.

Thus, in CPMG method a series of 180° pulse are applied at intervals τ , 3τ , 5τ , 7τ , etc., following the 90° pulse. Echoes are then observed to form at times 2τ , 4τ , 6τ , 8τ , etc. because the dephasing resulting from molecular interactions the protons can no longer be completely refocused, and the CPMG spin echo train will decay. On multiple repetitions

⁵The sequence takes the name from its designers.

⁶As said before, in the first chapter, this relaxation is entropic-type.

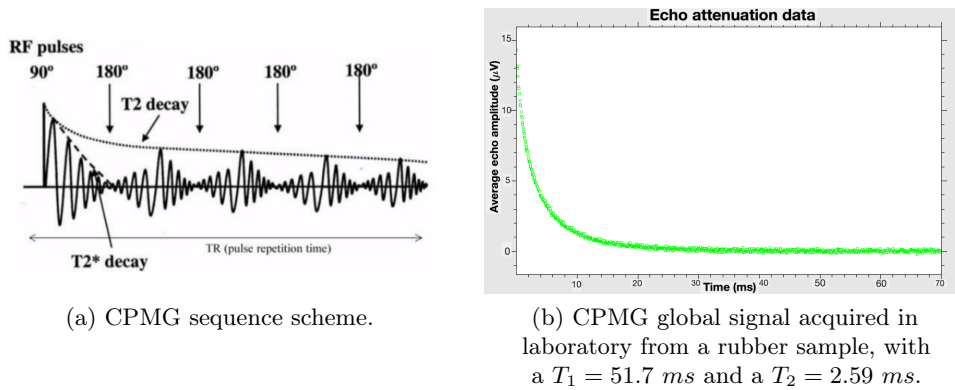


Figure 2.16: CPMG sequence.

of the 180° pulse, the height of the multiple echoes decreases successively as a consequence of T_2 dephasing. Therefore, the peak amplitude of an echo at a time t is given by:

$$A(t) = A(0) \exp\left(-\frac{t}{T_2} - \frac{1}{3}g^2\gamma^2 D\tau^2 t\right) \quad (2.7)$$

where γ is the gyromagnetic ratio of the nucleus species under exam, g is the constant gradient and D is the diffusion coefficient. The global trend of the signal is a decay following a time which can be considered the intrinsic T_2 (with a low contribute due to diffusion).

After $4/5$ times T_2 value, the signal decays to 0. The sequence, is typically acquired $4/8$ times to enhance the signal to noise ratio⁷.

Balanced Steady State Free Precession (bSSFP)

The scheme of a steady state free precession experiment is shown in Figure 2.17 and consists of a series of equally spaced (TR) phase coherent, and quasi-instantaneous radio frequency pulses with flip angle α . The magnetization is allowed to accumulate a constant phase advance (ϕ) within any TR, due to field inhomogeneities, local susceptibility gradients or chemical shift effects [53]. For reasons of simplicity, quasi-instantaneous radio frequency pulses are assumed (i.e., $T_{RF} \sim 0$). At time $t < 0$, the magnetization \mathbf{M} is presumed to be in thermal equilibrium (M_0). The magnetization is allowed to accumulate a constant precession angle (ϕ) during TR, i.e., due to static variations in the main magnetic field ($\phi \sim \gamma\Delta B_0 t$). In general, the duration (T_{RF}) of the excitation pulses is assumed to be short as compared to the overall relaxation processes (T_1, T_2) to separate the Bloch equations into repetitive basic units of radio frequency pulses and interpulse delays.

⁷Signals detected by the coil are very low, of the order of μV . The signal to noise ratio, SNR, increases following the square root of N , which is the number of repetitions

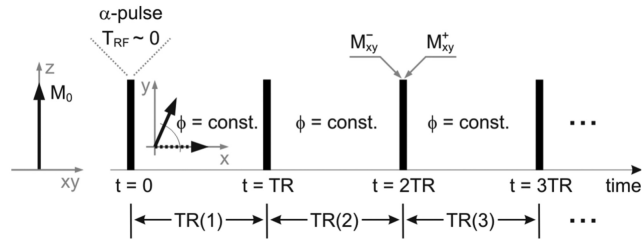


Figure 2.17: Scheme of a steady state free precession experiment. The magnetization immediately preceding (proceeding) the radio frequency pulse is labeled with a superscript "-" ("+"): M_{xy}^- (M_{xy}^+).

The succession of radio frequency pulses using the condition of $TR \ll T_2 \leq T_1$ does not allow magnetization to return to the thermal equilibrium state M_0 and each pulse acts on the remaining transversal and the remaining longitudinal magnetization. Magnetization in an experiment of this type is a mixture or superposition of different transversal and longitudinal states and results in complex patterns even after a few pulses (as shown in Figure 2.18), but after sufficient repetitions it reaches a steady state or *dynamic equilibrium* (meaning that the properties of the magnetization is unchanging with time).

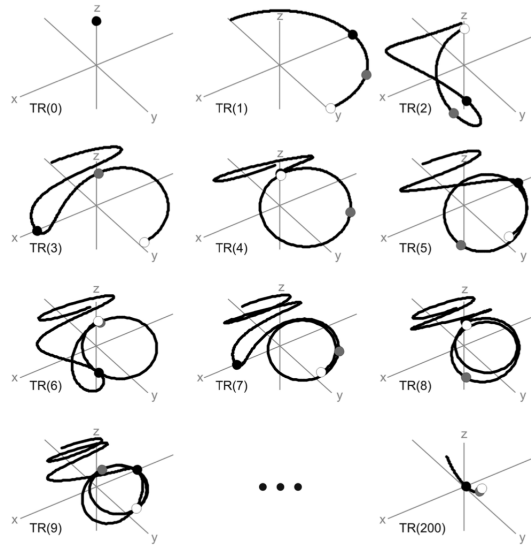


Figure 2.18: Time evolution of the magnetization in an experiment as shown in Figure 2.17 at $TE = TR/2$ for different TR periods as a function of the off-resonance related precession in the interval $[-180^\circ, +180^\circ]$. Black line = tip of magnetization vectors; black circle = $\phi = 0^\circ$; gray circle = $\phi = 90^\circ$; white circle = $\phi = 180^\circ$. Simulation parameters: $TR = 10ms$; $T_1 = 200ms$; $T_2 = 100ms$; $\alpha = 90^\circ$.

It can be observed that, independently from the off-resonance related precession angle, the magnetization reaches after some transient phase (after sufficient TR periods) a steady

state (i.e. a stationary value in the amplitude). The evolution is not the same and also the steady state is reached at different values.

The evolution of the magnetization in the transient phase and the analytical solutions to the transient response of SSFP, including off-resonance effects were derived by Ganter [54]. Using the eigenvector formalism it emerges that there are always one real and two complex conjugate eigenvectors that determine the transient response. In addition, using the perturbation theory, it emerges that the complex conjugate eigenvectors are perpendicular to the real one which is parallel to the steady state magnetization, M_{ss} . The real eigenvalue defines a relaxation rate parallel to M_{ss} [54] given by:

$$R_{\parallel} \approx \frac{1}{N^2} \cdot \left[\cos^2\left(\frac{\alpha}{2}\right) \cdot \sin^2\left(\frac{\phi}{2}\right) \cdot R_1 + \sin^2\left(\frac{\alpha}{2}\right) \cdot R_2 \right] \quad (2.8)$$

where $R_{1,2} := 1/T_{1,2}$ and

$$N := \sqrt{\cos^2\left(\frac{\alpha}{2}\right) \cdot \sin^2\left(\frac{\phi}{2}\right) + \sin^2\left(\frac{\alpha}{2}\right)} \quad (2.9)$$

In general, the results require $R_2 \cdot TR \ll 1$ [54]. The two complex conjugate eigenvalues yield an effective relaxation rate for the perpendicular components:

$$R_{\perp} \approx \frac{1}{2N^2} \cdot \left[\sin^2\left(\frac{\alpha}{2}\right) \cdot R_1 + \left(N^2 + \cos^2\left(\frac{\alpha}{2}\right) \cdot \sin^2\left(\frac{\phi}{2}\right) \right) \cdot R_2 \right] \quad (2.10)$$

The relaxation rates of both components depends not only on the flip angle, α , and on the relaxation rates $R_{1,2}$, but also on the off-resonance related precession angle, ϕ . The transient component in the magnetization parallel to the steady state magnetization shows a smooth decay, whereas the perpendicular components causes the oscillatory behavior in the transient phase. In general, the transition to steady-state from thermal equilibrium is completed after 5 times the T_1 value [53].

The steady-state instead, shows a strong dependence on the flip-angle (α) and on the relaxation time ratio (T_2/T_1). Off-resonances lead to a pronounced and periodic modulation in the steady state amplitude frequently referred to as the "frequency response" of balanced SSFP (as shown in simulations results in Figure 2.19).

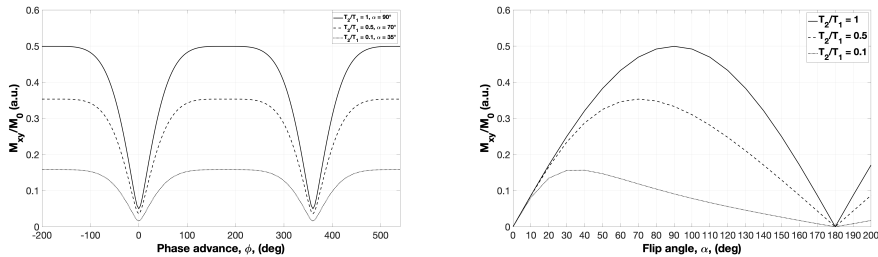


Figure 2.19: Steady state magnetization as a function of off-resonance and relaxation T_2/T_1 . Simulations parameters: $TR = 10ms$; $T_2/T_1 = 1 = 100ms/100ms$; $T_2/T_1 = 0.5 = 100ms/200ms$; $T_2/T_1 = 0.1 = 100ms/1s$.

In general, the amplitude decreases with decreasing T_2/T_1 and the optimum flip angle (yielding maximum steady state amplitude) decreases with decreasing T_2/T_1 . The steady state amplitude (i.e., the transverse magnetization component) immediately after the radio frequency pulse as a function of TR, TE, the flip angle α , relaxation times T_1, T_2 and off-resonances (ϕ) is given by:

$$M_{ss,xy}^+ = M_0 \frac{(1 - E_1)(1 - E_2 e^{-i\phi}) \sin \alpha}{C \cos \phi + D} \quad (2.11)$$

where

$$E_{1,2} := \exp(-T_{1,2}/TR) \quad (2.12)$$

and

$$\begin{aligned} C &:= E_2 (E_1 - 1) (1 + \cos \alpha) \\ D &:= (1 - E_1 \cos \alpha) - (E_1 - \cos \alpha) E_2^2 \end{aligned} \quad (2.13)$$

This type of sequence is called *Constant bSSFP* because all pulses are phase coherent (an experimental signal acquired performing this sequence is shown in Figure 2.20).

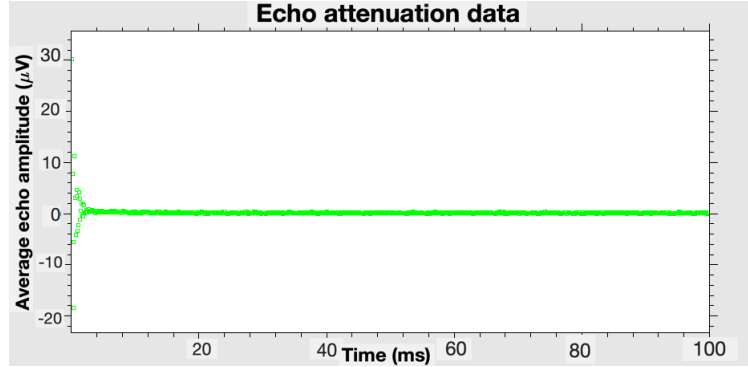


Figure 2.20: Signal acquired in laboratory using 90° pulse-constant-bSSFP sequence on a rubber sample with $T_1 = 51.7 \text{ ms}$ and $T_2 = 2.59 \text{ ms}$.

However, another more robust type of bSSFP sequence was used in this thesis work: the *Alternate bSSFP*. In this case the scheme of this sequence is equal to previous constant case, but what changes is the phase of pulses. This phase alternately is changed, so e.g., first pulse has 20° , second one has -20° , third one has 20° , fourth one has -20° , and so on. Also in this case it can be observed that, independently of the off-resonance related precession angle, the magnetization reaches after some transient phase (after sufficient TR periods) a steady state (i.e., a stationary value in the amplitude). An experimental signal acquired performing this alternate sequence is shown in Figure 2.21).

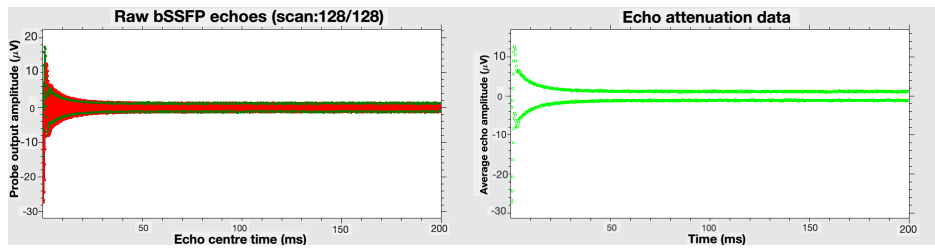


Figure 2.21: Signal acquired in laboratory using 90° pulse-alternate-bSSFP sequence on a rubber sample with $T_1 = 52.7$ ms and $T_2 = 2.59$ ms.

Magnetic Resonance Fingerprinting (MRF) - IR bSSFP

As seen in Section 1.3.1, instead of using a repeated, serial acquisition of data for the characterisation of individual parameters of interest, MRF uses a pseudo randomized acquisition that causes the signals from different materials to have a unique signal evolution or *fingerprint* that is simultaneously a function of the multiple material properties under investigation. Unique signal evolutions (or fingerprints) can be generated for different materials using an appropriate acquisition scheme. The idea is to continuously vary the acquisition parameters (such as the flip angle and phase of radio frequency pulses, the repetition time, echo time and sampling patterns) in a pseudo random manner, throughout the data collection.

The MRF-sequence implemented for this thesis work was based on an IR-bSSFP, because of its sensitivity to T_1 , T_2 and off-resonance frequency. It basically consists in a first 180° pulse to flip the magnetization along the z -axis and then it is applied a train of pulses (as the steady state sequence). The scheme of this sequence is reported in Figure 2.22.

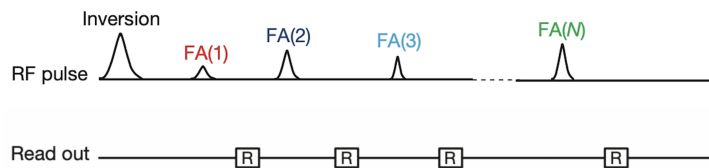


Figure 2.22: IR-bSSFP-based sequence scheme.

A typical flip angle pattern is shown in Figure 2.23 (a), while the expected signal obtained by a simulation is reported in Figure 2.23 (b). The signal seems to follow the flip angle pattern.

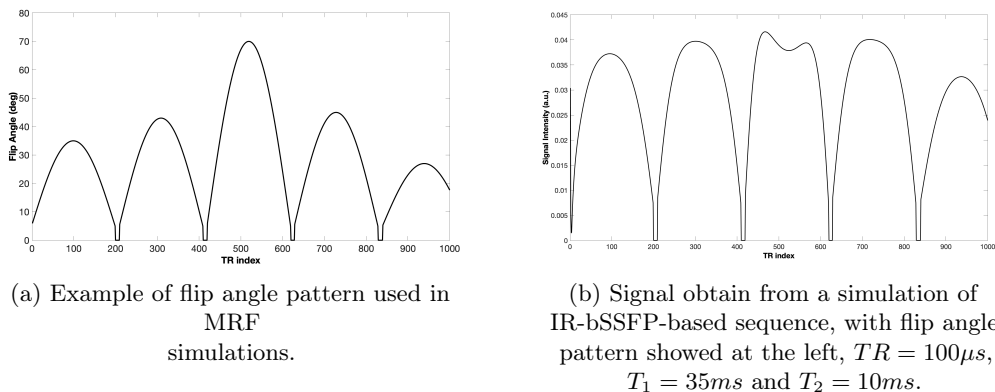


Figure 2.23: MRF-based sequence simulation.

2.1.3 Samples Analyzed

The samples used for this thesis work are two: EDTA and rubber. In particular, EDTA was used for the first investigative acquisitions, while the final comparisons were made using a rubber sample. The samples are placed inside a laboratory test tube which is sealed with a coating. An o-ring was placed around the test tube in order to lock it inside the magnet with the sample centered in the sensitive volume, where the height is 5 mm and the diameter is 8 mm.

Ethylenediaminetetraacetic acid (EDTA) is an aminopolycarboxylic acid with the formula $[CH_2N(CH_2CO_2H)_2]_2$. This white, water-soluble solid is used to bind to iron and calcium ions as a hexadentate chelating agent. The value of relaxation times, derived by inversion recovery and CPMG sequences, are $T_1 = 54 ms$ and $T_2 = 46 ms$.

While, the rubber sample used was a piece of a common rubber used as eraser, with the formula $-[CH_2C(CH_3)=CHCH_2]_n-$. The value of relaxation times are $T_1 = 51.7 ms$ and $T_2 = 2.59 ms$. The description of the software used to extract relaxation times for this sample is in Section 2.3.1, while the relaxation times distribution obtained are in the last chapter (Section 3.3).

An image of the rubber sample used in the test tube is in Figure 2.4.

2.2 Simulation Approach

The main goal of this thesis work is to implement a new MRF-sequence on the JEOL device, programming it on the KEA-II console. Although the signal evolution for this sequence is known in general, it is fundamental to validate the results obtained in laboratory with simulations. These simulations were conducted using *MARSS*, a program which allows to simulate all NMR sequences of interest. It was developed using Matlab by Dr. Stanislav Sykora and Dr. Marco Barbieri.

2.2.1 MARSS program

The block of MARSS program for an arbitrary sequence is shown in Figure 2.24.

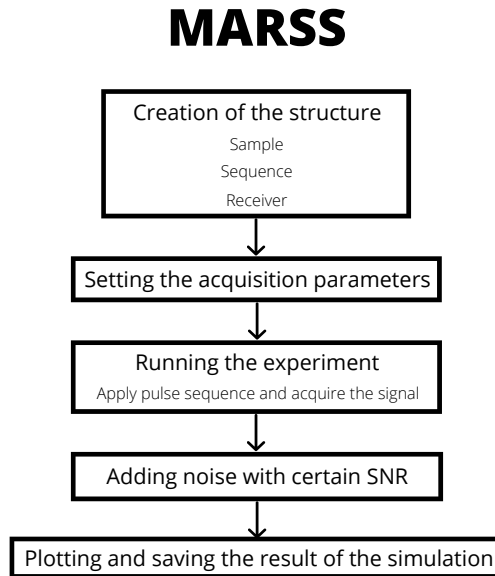


Figure 2.24: MARSS flux diagram.

Firstly, the structure is created (first box in the diagram in Figure 2.24). This consists in characterizing the sample, the sequence and the receiver.

The sample to be simulated and the magnetic fields influence on it are specified using a *LUT*. *LUT* stands for Look-Up Table and is a $N \times M$ table where all parameters of a sample and of the magnetic fields are set. In the real case, with low field NMR in laboratory, there is not a completely uniform magnetic field B_0 (i.e., not all spins are affected by the same field). To take into account that in simulation, in each row of the *LUT* there is an off-resonance component. Hence, each row corresponds to a different off-resonance component and in each columns its NMR parameters are specified (weight of this component, T_1 , T_2 , frequency, B_1 , D). An example of a part of a *LUT* is in Figure 2.25.

Component weight (a.u.)	T1 (s)	T2 (s)	Off-resonance frequency (Hz)	B1 (a.u.)	D (a.u.)
0.095607	0.0517	0.00259	-398.1	0.40036	0
0.095896	0.0517	0.00259	-398.1	0.40232	0
0.096173	0.0517	0.00259	-398.1	0.40427	0
0.096446	0.0517	0.00259	-398.1	0.40623	0
0.096716	0.0517	0.00259	-398.1	0.40819	0
0.096984	0.0517	0.00259	-398.1	0.41014	0
0.097249	0.0517	0.00259	-398.1	0.4121	0
0.097513	0.0517	0.00259	-398.1	0.41405	0
0.097776	0.0517	0.00259	-398.1	0.41601	0
0.098038	0.0517	0.00259	-398.1	0.41796	0
0.0983	0.0517	0.00259	-398.1	0.41992	0
0.098562	0.0517	0.00259	-398.1	0.42188	0
0.098826	0.0517	0.00259	-398.1	0.42383	0
0.099091	0.0517	0.00259	-398.1	0.42579	0
0.099359	0.0517	0.00259	-398.1	0.42774	0
0.099631	0.0517	0.00259	-398.1	0.4297	0
0.099906	0.0517	0.00259	-398.1	0.43165	0
0.10019	0.0517	0.00259	-398.1	0.43361	0
0.10047	0.0517	0.00259	-398.1	0.43557	0
0.10076	0.0517	0.00259	-398.1	0.43752	0
0.10106	0.0517	0.00259	-398.1	0.43948	0
0.10137	0.0517	0.00259	-398.1	0.44143	0
0.10169	0.0517	0.00259	-398.1	0.44339	0
0.10201	0.0517	0.00259	-398.1	0.44535	0
0.10235	0.0517	0.00259	-398.1	0.4473	0
0.1027	0.0517	0.00259	-398.1	0.44926	0
0.10306	0.0517	0.00259	-398.1	0.45121	0
0.10343	0.0517	0.00259	-398.1	0.45317	0

Figure 2.25: Example of Look-Up Table.

In the first column the weights of the component or the correlation between B_0 and B_1 distributions are entered. In the second and in the third columns there are the relaxation times (T_1 and T_2). In the fourth column the frequency is specified (for the B_0 component). In the fifth column there is the value of B_1 , expressed with respect to the expected B_1 value, e.g., 1 stands for the exactly chosen value of B_1 , i.e., the off-resonance component is affected by the exactly experimentally selected B_1 ; the value 0.9 indicates that the off-resonance component is affected by the 90% of chosen value of B_1 , and so on. Finally, the last column, indicates the diffusion values (D) in m^2/s . In all simulations the diffusion values were set to 0, supposing that there was not diffusion, based on time scales and analyzed materials. LUT values are extracted starting from experimental data. The specific methods are described in the next sections.

At the beginning of this first section of the script (where the structure is created), the LUT is loaded and it is given as input to the `MakeSample` function, with which the sample structure is created. This function uses a loop and other MARSS functions⁸ to create a structure data type "sample" containing the information about the different magnetization components present in the simulated sample.

In the second part of this section, the sequence acquisition parameters are set. Depending on the specific sequence, a number of parameters must be defined, as, for example, the relaxation delay (i.e., the repetition time between consecutive scans), the flip angle in radians of the excitation pulse, the phase cycle length, the phase vector of pulses (the following values can be selected: 0,1,2,3, indicating 0° , 90° , 180° , and -90° respectively). Selecting 0, the pulse will be applied along the $+x$ direction, selecting 1 the pulse will be applied along the $+y$ direction, and so on), and the number of echoes acquired. Other

⁸As, e.g., `NormalizeSample` function, which is used to normalize values of the LUT.

parameter must be specified for other specific sequences, as the ANGLE sequence. A more detailed description (with an example) is given in Appendix B. Obviously, all parameters must be selected to be the same of the correspondent selected ones in the laboratory experiments. Once the parameters are set, the sequence is created, using the correspondent function. For example, `Make_S1P` function is used for the FID 1-Pulse experiment, or `Make_SSFP` is used for the bSSFP sequences. These functions basically create an instance of the correspondence sequence. Hence, all parameters previously defined (i.e., the flip angle, the phase cycle length, and so on) are recalled and defined in the sequence structure.

The last part of this first section is for the receiver. It is possible to select the type (i.e., standard with 2 channels phd, or single-channel phd, or power phd, or modulus phd), and it is possible to specify the receiver's phase cycling. In fact the number of phase cycles indicates if the receiver has to follow the phase cycling (e.g., the value 1 suppresses the phase cycling), while the receiver phase cycling vector parameter follows the identical notation used for the applied pulses, i.e., 0 indicates that the receiver acquires along the $+x$ direction, 1 indicates that the receiver acquires along the $+y$ direction, and so on.

The next section in a sequence script (second box in the diagram in Figure 2.24) is where the signal acquisition parameters are set, as the FID duration (i.e., the total duration of the FID)⁹, the dwell time (i.e., the time delay between two adjacent sampled points), the number of total signal points, the vector times at which the signal is sampled, the real and imaginary parts of the signal and the FID, which is a matrix containing the signal (both real and imaginary part). This is the case of the FID-1 Pulse experiment. Obviously, there are other parameters for bSSFP experiments, as the number of sampled points for each echo in addition to the center point of the echo, the length in seconds of the acquisition window centered at the echo time, and so on. In this section it is also possible to select the number of dummies scans (during which the signal is not acquired), the signal to noise ratio in case you want add noise to the final signal, and finally the number of sampled scans.

The next section (third box in the diagram in Figure 2.24) is the one where the pulse sequence is applied to the sample. Here the experiment is simulated. Depending on the experiment, a series of functions are called, but, generally the first function is always the `RelaxSample` function. This function takes the sample (a structure data type previously created) as input and it creates an equilibrium longitudinal magnetization, updating the structure data type. Then, typically, the magnetization vector is preallocated with a for cycle. At this point, the experiment is performed using for cycles. A series of functions are called in this structure. For example, considering a bSSFP simulation, there is the `SSFP_2train2Sample` function. This function takes as inputs all parameters previously defined, as the sample structure, the sequence structure, the number of scans, the number of sampled points in each acquisition window, the length of the acquisition window centered at the echo time, the delta t of free evolution between adjacent sampled points, the FID matrix, the dummies scans, and the type of receiver. The output of this function is represented by `sampleout`, which is the result of the structure sample

⁹Time intervals are typically in seconds.

after the sequence, and by the FID, which represents the updated FID containing the sampled signal. Specifically, this function uses other MARSS functions, as the `createFreeEvolutionMatrix` function, which creates the free evolution matrix to apply to the magnetization, or the `createPulseMatrix` function, which is used to create the pulse matrix to apply to the magnetization. Moreover, the signal is acquired in this function calling the `SampleAccSignal` function, which simulates the acquisition of the signal from the sample with a specific receiver type.

The next section of a sequence script is not necessary and it was never used during the simulations of this thesis work (fourth box in the diagram in Figure 2.24). In this part it is possible to add noise with a certain signal noise to ratio, using a specific MARSS function called `add_wgn`, which takes the final FID acquired and the SNR as inputs and gives the signal with noise as output.

The signal as a function of time is typically plotted at the end of the sequence script (last box in diagram in Figure 2.24) and it is possible to save signal data to elaborate apart.

A commented example of some sequence codes used is reported in the Appendix B.

2.3 Data Analysis

Data acquired in the laboratory and results obtained by the simulations must be processed using specific software and methods. All methods used in this thesis work are reported in this section, starting from the laboratory data and the extraction of relaxation times to characterize the analyzed sample, and finishing with the metric used to compare experimental results with the simulated one.

2.3.1 UpenWin software

The relaxation times T_1 and T_2 were extracted using the UpenWin software. This software was developed for inversion of multi-exponential decay data for Windows system by V. Bortolotti, R.J.S. Brown and P P. Fantazzini at the University of Bologna [55] [56].

The data files acquired are in `.sdf` format. Loading the file in UpenWin, the data are bypassed by a filter, that compresses the data.

In the practice, the acquired relaxation curves are usually multi-exponential because not all spins are affected by the same local field (only in simple liquid samples such as water you can have mono-exponential relaxation). Thus, it is useful to assume that there are a discrete number (M) of components and the data are fitted using a function represented by the sum of a discrete number of exponential, each characterized by its own time constant, T_k and amplitude, a_k . The signal measured at each time t_i will be:

$$S(t_i) = \sum_{k=1}^M a_k e^{-\frac{t_i}{T_{(1,2)k}}} \quad (2.14)$$

where, starting from the n experimental $S(t_i)$, the $2M$ T_k and a_k parameters can be extracted, minimizing the residual sum of squares. Increasing the number of parameters,

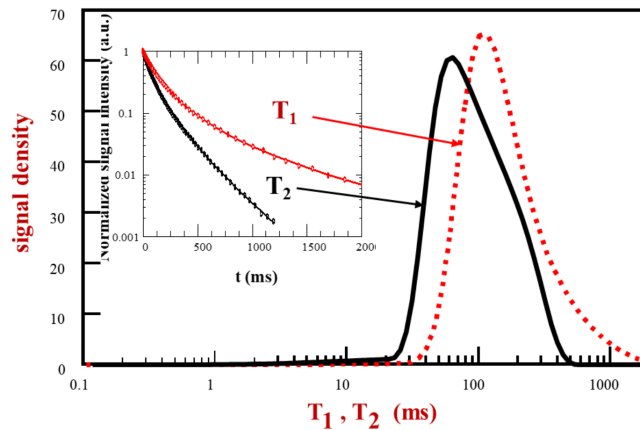


Figure 2.26: Inverse Laplace transform on relaxation curves.

you will obtain mathematically correct solutions, but this does not mean that these solutions will correctly represent the real physical system. Thus, a relaxation time continuous distribution is defined, characterized by a signal density function, $f(T_{1,2})$:

$$S(t) = \int_0^{\infty} f(T_{1,2}) e^{-\frac{t}{T_{1,2}}} dT_{1,2} \quad (2.15)$$

The passage from a measured time domain (t) to relaxation times domain to extract the function $f(T_{1,2})$ is done applying the inverse Laplace transform (Figure 2.26). Obviously, the $S(t)$ is acquired in the experiment, so it will be affected by a noise. The equation 2.15 becomes:

$$S(t) = \int_0^{\infty} f(T_{1,2}) e^{-\frac{t}{T_{1,2}}} dT_{1,2} + \epsilon \quad (2.16)$$

The consequence of adding the noise is that infinite distributions $f(T_{1,2})$ satisfy the equation 2.16.

In practice, you assume that the signal is due to a high number of exponential components (of the order of hundreds) and you search the so-called quasi-continuous solution of relaxation times (minimizing the residual sum of squares between experimental data and fit). To avoid excessive variations, a smoothing term is introduced. For many software this term is fixed, and this causes problems in signal interpretation (e.g., for a distribution with a narrow peak plus a low intensity tail, as it is often the case for liquid-saturated porous media, a fixed smoothing coefficient could widen the peak and split the tail in multiple peaks).

OpenWin software instead, searches the solution by introducing a term "penalty", that is weighted on the inverse of the curvature of the data. In particular, it has a variable smoothing coefficient along the distribution that allows the same "penalty" to be applied along the entire distribution curve. This is done by using an iterative negative feedback algorithm that at each iteration varies the values of the smoothing coefficient associated

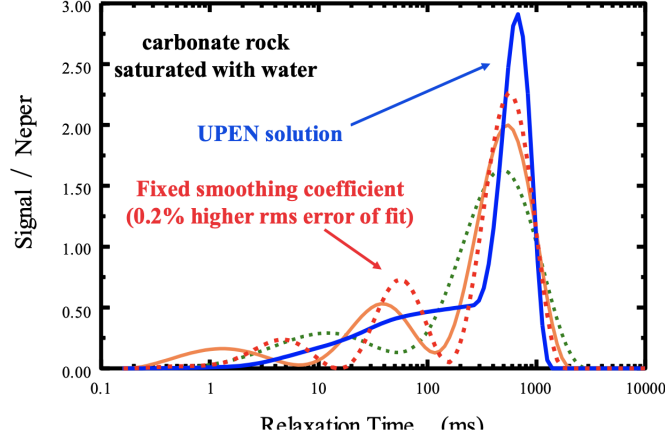


Figure 2.27: Comparison between solution obtained by UpenWin software and a solution obtained by another software that uses a fixed smoothing coefficient on carbonate rock saturated with water. Figure taken from the article [55].

with each point until each is inversely proportional to the square of the curvature at that point, so as to make the term "penalty" constant throughout the distribution. In this way the creation of unjustified peaks that lead to an erroneous interpretation of the acquired signal is minimized. In Figure 2.27 is shown a comparison between a curve obtained by the use of UpenWin software and a curve obtained by a software with a fixed smoothing coefficient (note the different peaks in the different distribution).

Moreover, the error minimizing equation of UpenWin is:

$$\sum_{j=1}^N B_j \left(g_0 + \sum_{k=1}^M g_k e^{-\frac{t_j}{T_k}} - s_j \right)^2 + \sum_{k=1}^M A_k g_k^2 + \sum_{k=2}^{M-1} C_k (g_{k-1} - 2g_k + g_{k+1}) \quad (2.17)$$

where C_k is the smoothing term, which is variable along the distribution g_k and $C_k(g_{k-1} - 2g_k + g_{k+1})$ is the "penalty" term, approximately constant.

2.3.2 Double-Angle Method

In the first simulations, to prove that it was important to correctly find how B_1 value varies and to test if the coil, in the laboratory part, was exciting the sample with the expected value of B_1 , the *Double-Angle Method* was used [57]. This analysis was important because the effective influence of B_1 distribution affects the sample after the pulses. Hence, for example, for the FID 1-Pulse sequence, the selection of 1 single value for the B_1 in the simulation (individuated by the double-angle method) provides a good agreement between the simulated signal and the acquired one. In this case, the B_1 distribution only affects the evolution period of the signal, immediately after the pulse. While, considering an experiment where a pulse train is applied for example, disagreements are immediately evident, and it is necessary to study the correlation map between the magnetic fields.

The double-angle method consists of performing two FID 1-Pulse experiment, where the value of the flip angle of the second acquisition is the double of the value of the flip

angle of the first acquisition. Then, considering the magnitude of the signals acquired, you expect that the value obtained in the case of the double value of the flip angle is the double of the value in the other case [58]. The goal is to estimate the effective flip angle given by the radio frequency pulse (and then compare it with the theoretical set value to find the proportion for the B_1 value):

$$\alpha = \arccos \left(\left| \frac{S_2(t)}{2S_1(t)} \right| \right) \quad (2.18)$$

Where α is the flip angle estimated, $S_2(t)$ and $S_1(t)$ represent the signal acquired in the case of the double value of flip angle and in the case of the selected value of flip angle respectively. The value of the signal considered was extracted from the first points acquired of the magnitude, performing a mean.

2.3.3 Fourier Transform

To extract the spectrum of off-resonance frequencies, i.e., the off-resonance frequency distribution, it is necessary to pass from the time domain to the frequency domain starting from experimental signals. This can be done using the *Fourier transform* (FT). The FT of a time dependent function is a complex-valued function of frequency, whose magnitude (i.e., the absolute value) represents the amount of that frequency present in the original function, and whose argument is the phase offset of the basic sinusoid in that frequency. The inverse of the FT mathematically synthesizes the original function from its frequency domain representation.

The Fourier transform of a function $f(x)$ is denoted $F(u)$ and it is defined as:

$$F(u) = \int_{-\infty}^{+\infty} f(x)e^{-2\pi jxu} dx \quad (2.19)$$

The function $f(x)$ will be obtained applying the inverse Fourier transform as follows:

$$f(x) = \int_{-\infty}^{+\infty} F(u)e^{2\pi jxu} du \quad (2.20)$$

This last result is known as the *Fourier inversion theorem*. In this notation u are the frequencies and x are the times.

For 2D signals, the transforms are defined as

$$F(u, v) = F[f(x, y)] = \int_{-\infty}^{+\infty} \int_{-\infty}^{+\infty} f(x, y)e^{-j2\pi(ux+vy)} dx dy \quad (2.21)$$

for the Fourier transform and

$$f(x, y) = F^{-1}[F(u, v)] = \int_{-\infty}^{+\infty} \int_{-\infty}^{+\infty} F(u, v)e^{j2\pi(ux+vy)} dudv \quad (2.22)$$

for its inverse.

In this thesis work case, the inverse *discrete Fourier transform* was used, which is the inverse of the discrete Fourier transform. This last one converts a finite sequence of equally-spaced samples of a function into a same-length sequence of equally spaced samples of the discrete-time Fourier transform, which is a complex-valued function of frequency. The interval at which the discrete-time Fourier transform is sampled is the reciprocal of the duration of the input sequence.

Thus, the discrete 1D Fourier transform of a function $f(x)$ is defined as

$$F(u) = \frac{1}{M} \sum_{x=0}^{M-1} f(x) e^{-j2\pi x/M} \quad (2.23)$$

for $u = 0, 1, 2, \dots, M$. The inverse discrete transform is defined as

$$f(x) = \frac{1}{M} \sum_{u=0}^{M-1} F(u) e^{j2\pi x/M} \quad (2.24)$$

for $x = 0, 1, 2, \dots, M$. Using the Euler formula the complex exponential functions can be replaced by trigonometric functions:

$$F(u) = \frac{1}{M} \sum_{x=0}^{M-1} f(x) \left[\frac{\cos(2\pi ux) - j \sin(2\pi ux)}{M} \right] \quad (2.25)$$

In this way, it is made explicit the dependency of the Fourier transform from the various frequencies composing the signal. Thus, the domain of $F(u)$ is properly called frequency domain and u represents the frequency of the various sinusoidal components.

In two dimension, the discrete Fourier transform is defined as

$$F(u, v) = \frac{1}{MN} \sum_{x=0}^{M-1} \sum_{y=0}^{N-1} f(x, y) e^{-j2\pi \left(\frac{ux}{M} + \frac{vy}{N} \right)} \quad (2.26)$$

and the inverse transform is

$$f(x, y) = \frac{1}{MN} \sum_{u=0}^{M-1} \sum_{v=0}^{N-1} F(u, v) e^{j2\pi \left(\frac{ux}{M} + \frac{vy}{N} \right)} \quad (2.27)$$

This last inverse 2D equation was used to extract the $B_0 - B_1$ correlation map.

2.3.4 $B_0 - B_1$ Correlation Map - 2D FFT

Simulations need LUTs to characterize the analyzed sample and to correctly represent the environment. In fact, in Section 2.2.1, it is shown the LUT parameters required. The method to separately extract the off-resonance distribution is shown in Section 3.1.1, while T_1 and T_2 values can be extracted using UpenWin software. For the B_1 values instead, the derivation is more challenging. Considering the low field NMR, in Section 1.2.4 it

is shown that the magnetic fields distributions are correlated and must be extracted together. If the condition 1.52 is satisfied ($\Delta\omega_0 \ll \omega_1$), the information related to this correlation is derived by the application of the 2D inverse discrete Fourier transform to a specific signal acquired using the ANGLE sequence. Here it is reported the method to extract this information from the ANGLE signal. This will be used to build the LUT to use for the simulations of all sequences.

The experimental data acquired from an ANGLE sequence are in `.csv` format and they are typically divided in two files:

- `data.csv` in which are collected peak integrals and pulse lengths. The ANGLE experiment is a sequence of FID 1-Pulse where the pulse length of each radio frequency is increased with a certain step. So this time interval is collected in this first file, flanked by the value of the magnitude of each correspondent signal. This value is averaged on first points for each signal. Plotting the peak integral as a function of pulse lengths you obtain a Figure as the bottom part of Figure 2.14.
- `data2.csv` in which are collected all the FIDs acquired. This is a matrix where in each row there are the single FID corresponding to the different pulse length and in columns there are real and imaginary parts which alternate, i.e., in the first row you have the complete acquired signal corresponding to the first pulse length and in the odd columns (1,3, and so on) you will found the real part of the signal, while in the even columns you will found the imaginary part of the signal.

Once loaded the files, an operation on the file containing FIDs is performed, to separate real and imaginary parts. In addition, the phase of the signal is set to $\pi/2$, in order to have that all information is only on one part. The Matlab code for this part is trivial, so it is not reported. When you are sure that all the signal is on one part, you can plot the two files, obtaining the Figure 2.14 (peak integrals can be also calculated from the FIDs matrix, averaging first points of the signal and plotting it as a function of pulse lengths).

At this point, the 2D inverse transform is performed. The first thing to do is to set the required parameters and compute the axis. The dwells for the single FIDs and for the pulse length is obtained from the `acqu.par` file, which contains all information about the experiment performed. Thus, the experimenter selects opportune values for these parameters¹⁰. The bandwidths are the reciprocal values of dwells. Moreover, in this type of experiment, the B_1 intensity is fixed¹¹. The estimation of the intensity is done recalling the relationship between the flip angle and the pulse intensity

$$\alpha = \gamma B_1 t_p = \omega_1 t_p \quad (2.28)$$

where t_p is the pulse duration, γ is the gyromagnetic ratio for the nuclei species under consideration. Considering the 1H , the gyromagnetic ratio is $\gamma = 267.5 \text{ MHz} \cdot \text{rad}/T$ or $\frac{\gamma}{2\pi} = 42.58 \text{ MHz}/T$. In the experiment, the value of pulse length to give a 90° pulse

¹⁰Typically, for the dwell of the FID, you select $0.5 \mu s$. For the step of increasing for the pulse lengths it is selected or the same value or $2 \mu s$. Values are always in the order of few μs .

¹¹Normally, as said before, the excitation field is in the order of mT .

founded is around $6 \mu s$. Inverting the equation 2.28, you obtain $B_1 \approx 1 mT$. This is the value used for simulations and data processing.

As said before, the inversion and all these considerations can be done only if the 1.52 condition is satisfied. Taking into account values derived, the ω_1 value is $\gamma \cdot B_1 = 267.5 MHz \cdot rad/T \cdot 1 mT = 0.2675 MHz \cdot rad$, while the experimental $\Delta\omega_0$ value is around $500 Hz$, thus the $\Delta\omega_0 \ll \omega_1$ condition is satisfied.

At this point, the processing is done followed the code below.

```

1 % 2D FFT
2 % Set required parameters
3 gamma = 42.58*10^6;
4 dwell = dwell_fid; % dwell fid
5 dwell_pls = 2e-6; % dwell pulse length
6 bw_off = 1/dwell;
7 bw_pls = 1/dwell_pls;
8 % 90, pulse length = 6\mus
9 alpha = pi/2;
10 gamma_rad = 267.5e6;
11 tp = 6e-6;
12 B1 = alpha/(gamma_rad*tp);

```

The axis are computed by steps, dividing the bandwidth by the length of the signal and creating vectors as shown in the code below.

```

1 % Compute the axis
2 f_b0_step = bw_off/length(signal(:,1));
3 f_pls_step = bw_pls/length(signal(1,:));
4 off_axis = linspace(-bw_off/2,bw_off/2,length(signal(:,1)));
5 pls_axis = linspace(-bw_pls/2,bw_pls/2,length(signal(1,:)));
6 b1_axis = (pls_axis./gamma)./B1;
7 Y = fftshift(fft2(signal));

```

At the end, the 2D inverse discrete Fourier transform (equation 2.27) is performed using the `fft2` build-in function. The `fftshift` command flips the lower frequencies in the center.

Plotting the `abs(Y)` as a function of the off resonance axis and B_1 axis, the shape of the correlation between the two magnetic fields is obtained. An example performed on simulated ANGLE data is shown in Figure 2.28.

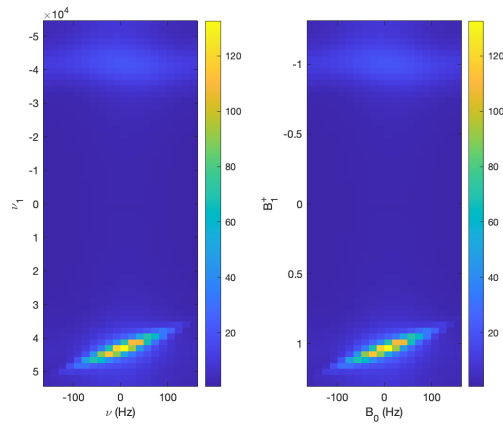


Figure 2.28: Example of reconstruction of the $B_0 - B_1$ correlation map obtained from simulated ANGLE data (supposing that the input data for the simulated ANGLE experiment presents a 45° Gaussian shaped correlation map of distributions). On the left the inverted signal is plotted as a function of the off-resonance axis and pulse axis (ν_1), while on the right the inverted signal is plotted as a function of the off-resonance axis and the B_1 axis. This last image typically is the one in which you are interested.

Zooming on the area of interest, it is clear that the map is very poorly resolved. To fix this, a 0-filling operation is performed on the signal in both dimensions, obtaining a better resolved 2D FFT (Figure 2.29).

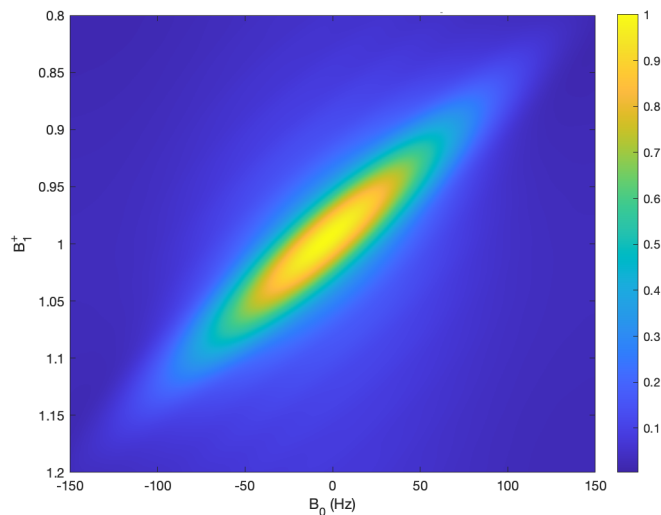


Figure 2.29: Estimated $B_0 - B_1$ correlation map of the case in Figure 2.28, after a 0-filling operation.

2.3.5 Creating a LUT for the simulations

Once extracted the correlation map performing the 2D FFT, and the relaxation times using the OpenWin software, it is possible to construct the LUTs for the simulations.

Comparing the simulated results and experimental ones it emerged that a better agreement is obtained considering a large correlation map, with dimension in the order of 512×1536 , where the first dimension indicates the number of B_1 components and the second one indicates the number of B_0 components.

Thus, after the map is calculated, it is necessary to resample and to resize the map, in order to have the required dimension. Obviously, the correct off-resonance and B_1 interval for the axis is selected, zooming and focusing on the area where there is the distribution.

At this point, the code used to create a LUT is similar to the one shown below.

```

1 T1 = 54e-3; %[s]
2 T2 = 46e-3; %[s]
3 D = 0;
4
5 LUT_img = zeros(512,1536,6);
6
7 for i = 1:512
8     for j = 1:1536
9         LUT_img(i,j,:) = [b0b1_outmap_resized(i,j),T1,T2,
10             off_axis_resized(j),b1_axis_resized(i),D];
11     end
12 end
13 LUT_r = reshape(LUT_img,512*1536,6);
14
15 LUT_r(LUT_r(:,1)<0)=0;
16 a = LUT_r(:,1);
17 indx_nnz = find(a>0);
18
19 LUT = LUT_r(indx_nnz,:);
20 save(strcat(save_fldr,'LUT'),'LUT');
```

where first the constant T_1 , T_2 and D values are set¹². Then a 3D matrix is created, containing the value of correlation map as weight for all components (2D map. In the code is expressed as `b0b1_outmap_resized`), and for each component, a value of T_1 , T_2 , B_0 (in the code is expressed as `off_axis_resized`), B_1 (in the code is expressed as `b1_axis_resized`) and D is assigned. The input for MARSS sequences must be a 2D matrix, so a reshaping is performed, considering all values. If you want exclude the component with lower frequencies it is sufficient to change the 0 in the inequality in the row 15 (e.g., setting 0.1 means that each component with a correlation value, i.e., a weight, less than 0.1 are omitted). This is done to create smaller LUT and, thus, to speed up simulations.

¹²In all simulation the diffusion values were set to 0, supposing that there was not diffusion, based on time scales and analyzed materials.

Finally, the LUT is saved and can be used to perform all simulated sequences.

2.3.6 Signal comparison with RMSE

The metric selected to compare results between experiments and simulations was the *Root Mean Squared Error* (RMSE), which represents the square root of the second sample moment of the differences between predicted values and observed values or the quadratic mean of these differences. Moreover, the RMSE is a measure of accuracy, to compare forecasting errors of different models for a particular dataset and not between datasets, as it is scale-dependent [59].

RMSE is always non-negative, and a value of 0 indicates a perfect fit to the data. This result is almost never achieved in practice. In general, a lower RMSE is better than an higher one, but comparisons across different types of data would be invalid because the measure is scale-dependent of the number used.

RMSE is defined as the square root of the average of squared errors. Thus, its units are the same of the analyzed values, and the effect of each error on RMSE is proportional to the size of the squared error. This means that larger errors have a disproportionately large effect on RMSE and, consequently, RMSE is sensitive to outliers [60].

The RMSE of N predicted values \hat{y}_t with respect to N variables observed y_t is defined as

$$RMSE = \sqrt{\frac{\sum_{t=1}^N (\hat{y}_t - y_t)^2}{N}} \quad (2.29)$$

In Matlab, after performing a normalization of the signals (by taking the magnitude vector and dividing it by the norm of the vector itself), the experimental and simulated results are compared using a code line as

```
1 RMSE = sqrt(mean((y-yhat).^2));
```

where `y` and `yhat` are the normalized experimental and simulated signals.

Chapter 3

Results and Discussion

The goal of this thesis work was to implement an MRF-based sequence on a customized NMR relaxometry apparatus (JEOL C60 + KEA-II) at the Physics and Astronomy department of University of Bologna. To achieve this objective many simulated and laboratory experiments have been performed to characterize the magnetic fields correlation map, and then to validate all results via simulations.

The influence of B_1 occurs when a pulse is applied. For example, in a FID 1-Pulse experiment, where only one radio frequency pulse is applied at the beginning of the sequence, the B_1 influence is shown immediately after the pulse application, in correspondence of the evolution period of the signal. While, considering experiments where a pulse train is applied to the sample, the B_1 influence is more visible in all the signal. For this reason, the first acquisitions in laboratory confirmed the necessity to determine the distributions of the magnetic fields and their correlation. All experimental results were validated by means of simulations through the MARSS toolbox (Section 2.2). In the first section of this chapter these first results are shown.

In the second section, the investigation to find the best parameters for simulations is described. These tests were simulated in Matlab to investigate the suited initial conditions of the LUT in greater detail. In particular, different distributions were investigated for the $B_0 - B_1$ correlation map. Once defined the initial conditions for the LUT, which we assumed as the *ground truth data*, the sequences of interest were simulated. Then correlation maps were extracted from the simulated ANGLE results (using method described in Section 2.3.4) and LUTs were reconstructed. Finally, sequences of interest were performed using *post-ANGLE* LUTs and results were compared with the correspondent ground truth results, finding the best parameters which minimized the RMSE.

Finally, when the parameters to describe the $B_0 - B_1$ correlation within the sensitive volume were found, many sequences were performed in laboratory by using a sample made of rubber. In the final section of this chapter, these last results are reported.

3.1 First tests and sequences validation

The first laboratory acquisitions were: FID 1-Pulse and balanced steady state sequences (after performing *Wobble* and *Pulse calibration* sequences to correctly set the sample and experimental setup, described in Sections 2.1.1 and 2.1.2). The first sequence was already incorporated in the KEA console, thus, only steady state sequences were programmed ex novo. IR and CPMG sequences were also performed to determine the intrinsic relaxation times values of the sample.

The purpose was to check the accuracy of the newly programmed sequences (bSSFP) with the final goal of realizing and implementing a MRF-based sequence. Moreover, this first investigation had the goal to confirm that was not sufficient extracting information about the B_0 distribution, with the off-resonance frequencies.

For this investigation step, a sample of doped water (H₂O + CuEDTA) was used, with relaxation times $T_1 = 54 \text{ ms}$ and $T_2 = 46 \text{ ms}$. T_1 was calculated from a best fit of the longitudinal relaxation curve using the *Curve Fitting Tool* Matlab toolbox (Figure 3.1). While, the T_2 value was determined by a mono-exponential fit performed by Prospa software, after a CPMG acquisition (Figure 3.2).

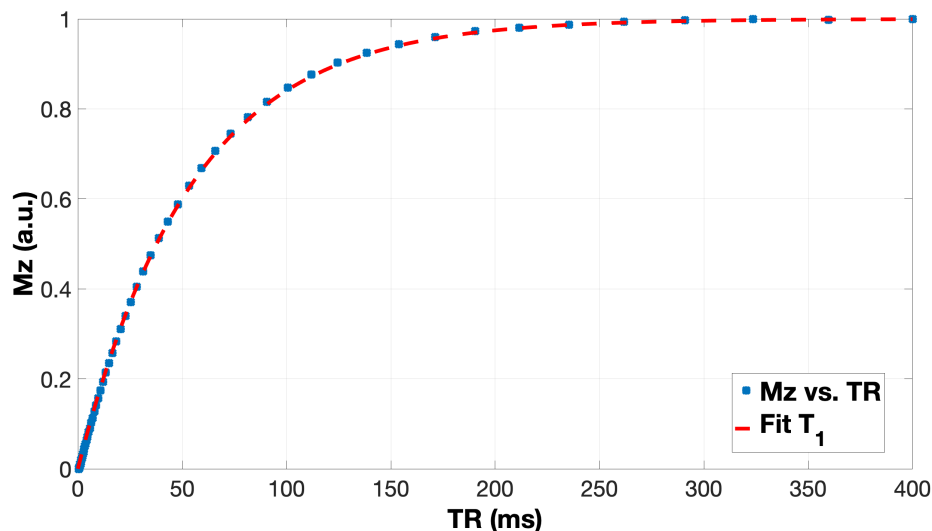


Figure 3.1: T_1 curve fit using the *Curve Fitting Tool* Matlab toolbox. The value obtained was $T_1 = 54 \text{ ms}$.

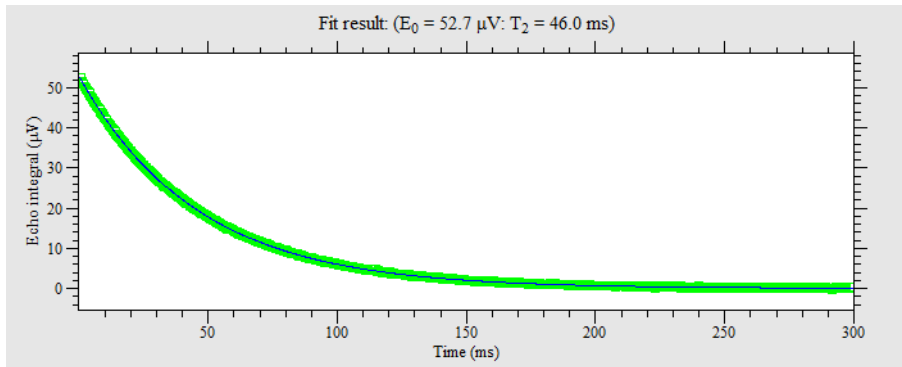


Figure 3.2: T_2 curve fit performed by Prospa software. The value of the relaxation time was $T_2 = 46 \text{ ms}$.

These are the relaxation times values used to characterize the sample in the LUT.

3.1.1 B_0 off-resonance distribution

At this point, once acquiring all data from the experiments of interest, the first data analysis consisted in studying the B_0 distribution. The information about B_0 distribution has been used to create the LUT, as described in Section 2.3.5.

Specifically, the data from the FID 1-Pulse experiment are used to create the off-resonance distribution. The idea is to extract the spectrum on the right in Figure 2.13. This is done creating a complex vector using the real and the imaginary part of the acquired signal, then an inverse Fourier transform is performed, in order to move in the frequency domain (starting from the time domain). The bandwidth is calculated knowing the sampling rate (also called *dwell* time of the experiment), i.e., the time interval between two sampled points of the FID signal. The frequency interval is calculated, with a step in Hz , dividing the bandwidth by the length of the spectrum signal (inverted signal).

Plotting the real part of the spectrum versus the frequency interval gives the off-resonance distribution. A limited plausible interval is selected (e.g., $\sim 500/600Hz$), omitting near-zero values for the off-resonance values.

Simulations showed that the number of off-resonance components directly extracted (typically, on the order of 10) was not sufficient to create a LUT which correctly reproduces the magnetic field conditions, so it was increased on the order of 400/500 component to simulate results with a better agreement with experimental ones. To achieve this purpose the 0-filling method was applied.

A representation of an off-resonance distribution is shown in Figure 3.3, where 500 component of off-resonance were selected.

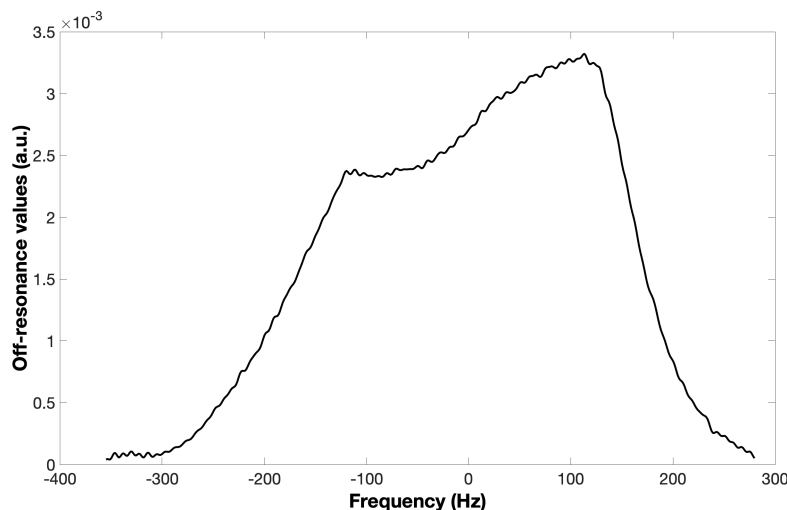


Figure 3.3: Example of an off-resonance distribution with 500 components extracted from FID 1-Pulse data. Experiment acquired using an EDTA sample with $T_1 = 54 \text{ ms}$ and $T_2 = 46 \text{ ms}$.

While, an example of the code used for this procedure is shown below.

```

1 re_fid = fid_data(:,2); % Real part of the signal acquired
2 img_fid = fid_data(:,3); % Imaginary part of the signal acquire
3 complex_signal = complex(re_fid, img_fid);
4 % 0-filling
5 n = length(complex_signal);
6 scl = 5;
7 vector_0 = zeros(scl*n,1);
8 fid = cat(1, complex_signal, vector_0);
9 % Inverse Fourier transform
10 spectr_sign = fftshift(iff(fid));
11 % Bandwidth
12 bw = 1/(2*10^-6);
13 % Step in Hertz
14 step_f = bw/length(spectr_sign);
15 % Frequencies axis
16 f = [-bw/2:step_f:bw/2]; khertz_freq = f./1000;
17 % Finding and selecting the interval of interest
18 indexes = find(khertz_freq > -0.356 & khertz_freq < 0.281016);
19 spect_zoom = real(spectr_sign(indexes));
20 f_zoom = f(indexes);
21 % Off-resonance distribution
22 off_dist = cat(2, f_zoom', spect_zoom);

```

The inverse discrete Fourier transform (equation 2.24) of the signal is performed using the `fft` build-in function (row 10). The `fftshift` command flips the lower frequencies in the center.

3.1.2 B_1 estimation using Double-Angle Method

After evaluating the B_0 distribution, the investigation has moved to the B_1 characterization. The value of the effective B_1 applied was extracted using the *Double-Angle method* described in Section 2.3.2. Thus, after acquiring two different FID signals, with the FID 1-Pulse sequence, selecting 60° and 120° as values for the flip angles, the data analysis was conducted. The sample used in laboratory for acquisitions was the EDTA sample.

This method is based on the comparison of the signal intensities, hence, the magnitudes were calculated and then a mean was performed, only considering the first 50 points. The value of the effective flip angle was obtained calculating the arc cosine of the ratio between magnitudes. The script is shown below.

```

1 % Real and imaginary signal a = 60
2 real_60 = fid_60(:,2); img_60 = fid_60(:,3);
3 % Magnitude and mean on first 50 points
4 mod_60 = abs(complex(real_60, img_60)); s_60 = mean(mod_60(1:50));
5 % Real and imaginary signal a = 120
6 real_120 = fid_120(:,2); img_120 = fid_120(:,3);
7 % Magnitude and mean on first 50 points
8 mod_120 = abs(complex(real_120, img_120)); s_120 = mean(mod_120(1:50))
9 ;
10 % Estimated alpha in radians
11 dam_alpha_rad = acos(s_120/(2*s_60));
12 true_alpha_deg = (dam_alpha_rad*180)/pi;
13 B_1_value = true_alpha_deg/60;

```

Using this method, the B_1 found value was approximately 1, specifically 1.12. This is a dimensionless number, indicating the ratio between the effective value of excitation and the selected nominal one. It means that the coil provides a radio frequency pulse with an efficiency of 112% in mean in the laboratory experiments. This was subsequently confirmed in the rubber study case.

3.1.3 B_1 distribution and its correlation with B_0

At this point, LUTs can be created following the procedure in Section 2.3.5, and the correspondent laboratory sequences can be simulated using MARSS¹. Several simulations and tests were performed changing some parameters of interest, e.g., the flip angle value, but here are reported the most significant. All sequences parameters are specified in the next subsections, where results are shown and discussed.

Three principal LUTs were created changing the B_1 value: the first one had a constant B_1 value set to the nominal value², 1, according to double-angle method result; the B_1 value selected for each off-resonance component in the second LUT followed a linear equally-spaced interval starting from 0.6 and ending to 1.4 (i.e., you assume that the first component is affected by the 60% of the effective B_1 value selected in laboratory, the

¹Obviously, the simulation parameters must be set as equal as the experimental correspondent ones.

²Remember that B_1 value is entered in LUTs as a coefficient with respect to the nominal value.

second one is affected by a slightly higher value, and so on, until the last component, which is affected by the 140% of the effective B_1 value); the last LUT was similar to the second one, except for the B_1 interval. In this case it started from 0.8 and it ended to 1.2.

Once obtained simulated signals, the comparison with the experimental ones was conducted, using the RMSE as metric. This comparison has not always been done using all signal points, because, e.g., for the bSSFP signals, the steady state values were close to zero value, thus a lower impact on RMSE was expected. Hence, the transient phase was more interesting to investigate. Moreover, these operations were performed using normalized signals, in order to be sure to conduct a consistent comparison. The normalization consisted in taking the magnitude vector (obtained by the `complex` Matlab build-in function with the real and imaginary part of the signal as input) and dividing it by the norm of the vector itself. The normalized real and imaginary parts then were extracted by using the `real` and `imag` Matlab build-in functions on the normalized complex vector.

A disagreement between simulated and acquired signals had been expected, because the B_1 was roughly set. The aim was to demonstrate that a simple linear B_1 variation does not approximate properly the real case, and a specific correlation function between B_0 and B_1 must be investigated.

However, in the FID 1-Pulse case, the simulation showed a good agreement with the acquisition, as shown below. This is due to the fact that FID 1-Pulse sequence only uses one radio frequency pulse and this causes that the effective influence of B_1 distribution only affects the evolution period of the signal, immediately after the pulse.

Hence, more representative results are shown below, considering the agreement case (FID results) and the expected disagreement case (bSSFP results).

FID case

Results presented in this subsection were obtained performing the FID 1-Pulse sequence. The main acquisition parameters were the flip angle value, set to 90° , the dwell time (i.e., time interval between two sampled points), set to $2 \mu s$, the number of points acquired, set to 65536, the number of scans (to increase the SNR), set to 32, the pulse length of the 90° pulse set to $6 \mu s$ (estimated with an initial pulse calibration sequence), and the repetition time, set to $0.5 s$.

The simulation parameters were set to be the same as the acquisition ones, in order to perform the comparison.

Figure 3.4 shows the comparison using the signal simulated with the second LUT (B_1 interval $[0.8 - 1.2]$). Results obtained from the other LUT are very similar, so they are not reported. The RMSE value in this case was $RMSE = 4.00 \cdot 10^{-4} a.u.$, which corresponds to a good agreement, that is also qualitatively visible directly from the figure. RMSE was calculated comparing normalized magnitudes of the two signals. The other RMSE values obtained using other LUTs was on the same order (10^{-4}). Moreover, a focus of signals on first 800 points ($t = [0 - 1.6] ms$) is reported in the figure on the right in 3.4 to show the B_1 influence which affects the first points of the signal. The signal in the simulation was obtained setting to 0 the noise, because it is not important to consider this aspect for this comparison.

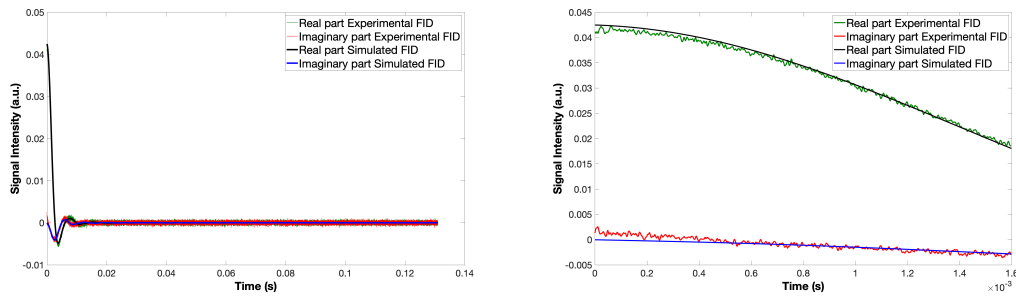


Figure 3.4: On the left, the comparison between simulated FID signal obtained with a LUT created using the off-resonance distribution shown in Figure 3.3, B_1 values in the interval $[0.8 - 1.2]$ and relaxation times $T_1 = 54 \text{ ms}$, $T_2 = 46 \text{ ms}$, and experimental FID signal acquired on an EDTA sample with the same relaxation time values. $\text{RMSE} = 4.00 \cdot 10^{-4} \text{ a.u.}$. On the right, a focus on first 800 points ($t = [0 - 1.6] \text{ ms}$) of the signals.

bSSFP case

Results presented in this subsection were obtained performing the bSSFP sequences. The acquisition parameters are the same for both sequences (constant and alternate). What changed was the phase of the pulses in the alternate sequence, to follow the correspondent scheme described in Section 2.1.2. The sequence parameters were the flip angle value, set to 90° , the dwell time (i.e., time interval between two sampled points), set to $1 \mu\text{s}$, the number of echoes acquired, set to 400, the number of scans (to increase the SNR), set to 32, the pulse length of the 90° pulse set to $6 \mu\text{s}$ (estimated with an initial pulse calibration sequence), and the repetition time, set to 0.5 s .

The simulation parameters were set to be the same as the acquisition ones, in order to obtain a similar signal to compare later with the correspondent experimental one.

Results in the balance steady state cases are definitely different from the FID case. The necessity to better characterize the B_1 influence on the sample, finding its distribution and its correlation with the off-resonance distribution is evident. The disagreement between simulations and experiments confirms this hypothesis.

This can also be derived from another important aspect that emerged, i.e., the fact that using a simple B_1 distribution in the LUT led to not satisfactory results. It is immediately evident from the Figures 3.5, 3.6 that a constant B_1 value, fixed to the nominal value, gives a not realistic result.

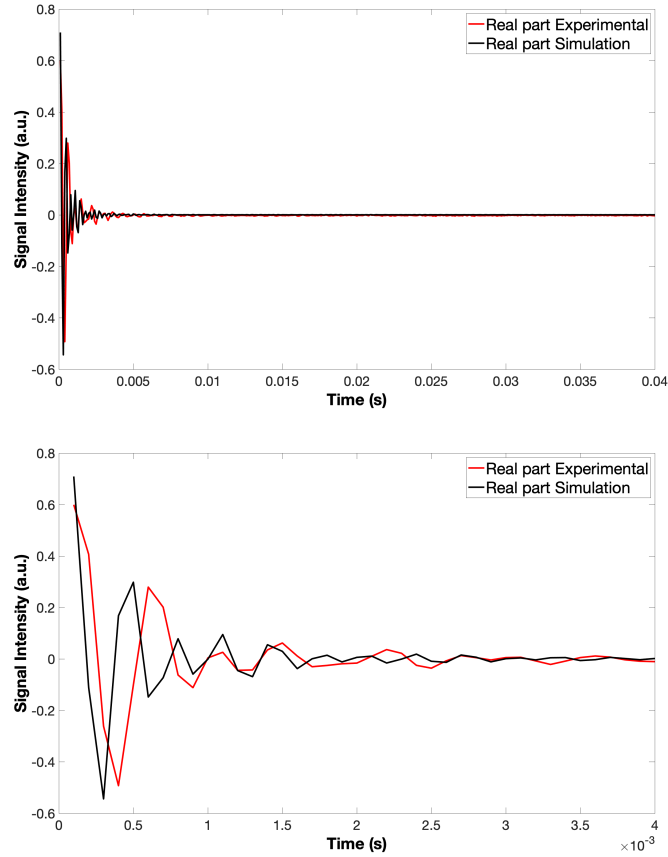


Figure 3.5: On the top, experimental versus simulated normalized real part of the signals for the constant bSSFP case. LUT with B_1 values in the interval $[0.6 - 1.4]$. RMSE = 0.1585 a.u. . On the bottom, a focus on first 40 echoes ($t = [0 - 4] \text{ ms}$) of the signals.

However, although the case with B_1 varying in the interval $[0.6 - 1.4]$ showed the best result, this was not sufficient. The RMSE for this case was 0.1585 a.u. . Moreover, from the zoomed plot, where only the first 40 echoes ($t = [0 - 4] \text{ ms}$) of the signals are showed (down figure in 3.5), it is clear the presence of a sort of shift between signals, due to the approximated B_1 which affected the magnetization evolution in the simulation.

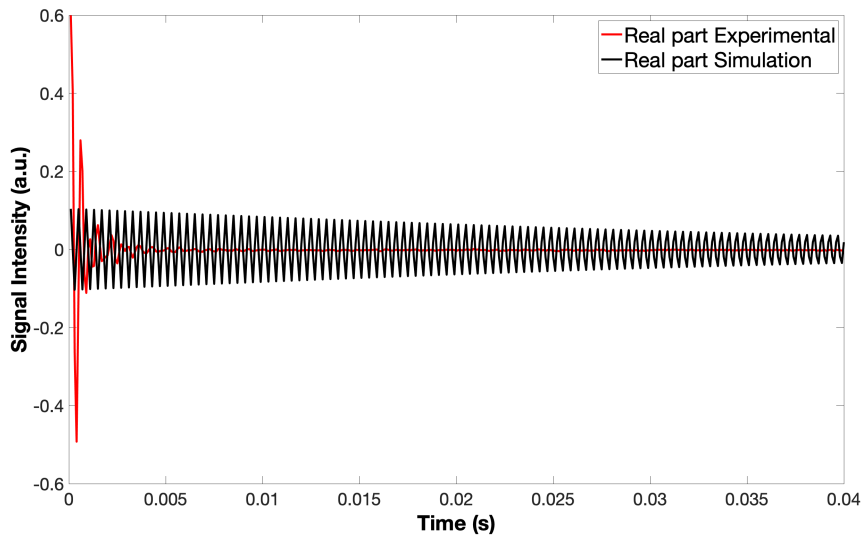


Figure 3.6: Experimental versus simulated normalized real part of the signals for the constant bSSFP case. LUT used had constant $B_1 = 1$. RMSE = 0.1796 *a.u.*.

These first results refer to the constant balance steady state sequence, described at the beginning of Section 2.1.2. It is not necessary to report all comparisons obtained varying roughly the B_1 , because they confirm the previous assumptions. The signals are plotted only considering normalized real parts, where all information was stored. Thus, the RMSEs were derived using the normalized real part of signals. Notice that, not all points of the signals were used to calculate the RMSE, because, as we expected, the steady state values were close to zero value and a lower impact on RMSE was expected. Hence, only first 40 echoes ($t = [0 - 4] \text{ ms}$) were considered to calculate RMSEs, on a total of 400 sampled echoes.

Simulations on alternate balance steady state sequence were performed too, and also in this case a disagreement was obtained. For the sake of completeness a comparison between experimental and simulated signals, with a focus on first 40 echoes ($t = [0 - 4] \text{ ms}$), is reported in Figure 3.7. Here normalized magnitudes were plotted and used to derive the RMSE value. In this case, the RMSE was 0.0171 *a.u.*. This sequence is more robust than the correspondent one with the constant phase, although from the figures the disagreement is still evident in this case. In fact, the steady state has been reached before by the experimental signal, which showed in addition a less oscillating transient phase. In constant B_1 case, the RMSE value was worst, but its value was on the same order of the shown case. This was an additional confirmation of the initial considerations on magnetic fields.

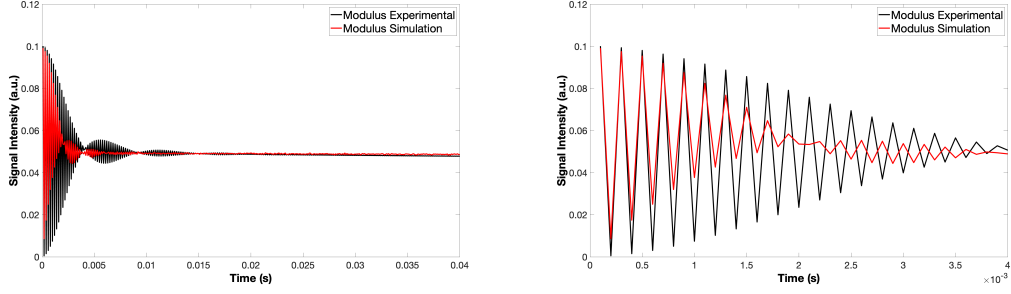


Figure 3.7: On the left, experimental versus simulated normalized magnitude of the signals for the alternate bSSFP case. LUT with B_1 values in the interval $[0.8 - 1.2]$. RMSE = 0.0171 *a.u.*. On the right, a focus on first 40 echoes ($t = [0 - 4]$ ms) of the signals.

3.2 Investigating the best parameters for simulations

The data analysis performed to properly characterize the $B_0 - B_1$ correlation is shown in this section. The correlation can be represented as a 2D map where one dimension corresponds to the off-resonance components, while the other dimension corresponds to the B_1 components.

Information about the correlation between the two distributions can be obtained performing the ANGLE experiment (Section 1.2.4). The idea was to simulate the ANGLE sequence with MARSS in order to find the best parameters to use later for optimizing the laboratory acquisition. The ANGLE experiment is described in Section 2.1.2.

Initially, some Gaussian distributions were selected for correlation maps. These were assumed as ground truth data (from here on, *ground truth data*). Using these maps, LUTs were created, and the ANGLE experiment was simulated for each LUT. Then, the simulated signals were processed using the 2D FFT method and the extracted maps (from here on, *post-ANGLE data*) were compared to the correspondent ground truth ones. The aim was to achieve a good matching between the maps, so that we could use this method to extract the maps from the experimental signals of ANGLE sequence.

The second part of the investigation regarded sequence simulations using LUTs created with the ground truth maps, and using LUTs created with the correspondent post-ANGLE maps. Analyzed sequences were the balance steady state with both constant and alternate phases, and the MRF-based sequence (IR-bSSFP-based sequence). After performing all sequences, ground truth results were compared with the correspondent post-ANGLE results in order to evaluate the reasonable minimum resolution for building the correlation map. If a good matching would be obtained these results would led to individuate some level of confidence with which correlation maps can be reconstructed, without losing information. Moreover, this last investigation individuated some suited parameters used later as guide in last laboratory acquisitions.

3.2.1 ANGLE Approach

Many ANGLE simulations were performed, varying a lot of parameters, both in the LUT itself and in the sequence. Here the most important results are shown.

One first investigation regarded the total duration of the sequence.

Two principal Gaussian distributions were selected for the correlation maps. First one was a 64×64 2D Gaussian distribution, with the same standard deviation along the two principal directions. The other one was a 64×64 45° -shaped 2D Gaussian, with the axis along the 45° direction longer with respect to the axis on the perpendicular direction. Regarding the range of the off-resonance components, an interval of 300 Hz was selected, starting from -150 Hz , and ending to $+150 \text{ Hz}$, for both Gaussian distributions. For the B_0 , the Gaussian distributions were centered at $B_0 = 0 \text{ Hz}$. The minimum resolution was obtained dividing the bandwidth by the length of the correspondent dimension of correlation map. While, an interval starting from 0.8, i.e., the 80% of the B_1 nominal value, and ending to 1.2, i.e., the 120% of the B_1 nominal value was selected for the B_1 components. For the B_1 , the Gaussian distributions were centered at the nominal value of $B_1 = 1$. In this case, the minimum range was obtained dividing the length of B_1 interval (i.e., 0.4) by the length of the correspondent dimension of correlation map. For the sake of completeness, other distributions were analyzed, e.g., Gaussian distributions like the first one described, but shifted of 100 Hz for the B_0 , or centered at $B_1 = 0.8$. These investigations were conducted to see if the extracted post-ANGLE maps correctly represented the shifting. These results are not reported, because conclusions are the same of the reported ones.

The other parameters were chosen to simulate the relaxation characteristics of the real sample, with $T_1 = 0.46 \text{ s}$, $T_2 = 0.37 \text{ s}$, and $D = 0 \text{ m}^2/\text{s}$ (in all simulations the diffusion values were set to 0, supposing that there was not diffusion, based on time scales and analyzed materials).

ANGLE parameters and Nyquist–Shannon sampling theorem

The characterization of $B_0 - B_1$ map is based on the considerations on the simulation parameters described in this section. These were necessary to speed up simulations and to be sure to acquire consistent results, considering that ANGLE simulation required a large amount of computational time (on the order of 3/4 days).

An ANGLE experiment consists of a series of FID 1-pulse, where after each pulse a complete FID signal is acquired. The flip angle increases at each pulse with a fixed step. The description of these sequence is in Section 2.1.2.

First of all, ANGLE simulation requires to select the value of B_1 , which remained fixed for the simulation. The value was $B_1 \sim 1 \text{ mT}$, and it was obtained inverting the Equation 1.14, considering that the pulse length to give a 90° pulse was around $6 \mu\text{s}$.

The reconstruction of maps is based on the 2D inverse FFT, thus data must be acquired and converted considering in a proper way the minimum resolution and intervals in order to avoid aliasing and information loss. These considerations were based on the *Nyquist - Shannon sampling theorem*. Considering this, it was possible to extract

minimum values for, e.g., dwell times, which then were set in the ANGLE sequence to conduct investigations avoiding both information loss, and aliasing problem.

The *Nyquist - Shannon Theorem* (from here on, N-S theorem) establishes a sufficient condition for the sampling rate to guarantee not to lose information from a continuous-time signal of finite bandwidth, without aliasing issues. In particular, the theorem states that, given a function whose Fourier transform is zero outside a certain frequency range (i.e., a limited-band signal), in its analog-digital conversion the minimum sampling frequency necessary to avoid aliasing and loss of information in the reconstruction of the original signal must be greater than double its maximum frequency. Hence, it was necessary to specify the minimum resolution and intervals both for B_0 , and for B_1 .

Considering the B_0 field, the maximum frequency in both cases reported, was +150 Hz, hence, according with the N-S theorem, this value was multiplied by 2.1 (because the frequency must be greater than 2 times the maximum frequency) and the result was inverted, to obtain dwell value for FID sampling (i.e., step between two sampled points) on which depends the off-resonance distribution. This value is indicated as dt in the simulation script (see row 3 of the example code related to the section of acquisition parameters in Appendix B). Moreover, another important parameter to select was the total acquisition time for the FID signal, in order to be sure to acquire complete relaxations. This value is specified in the simulation by the selection of the number of the sampled FID points, which it is multiplied by the dwell time (see row 4 of the same example code cited right up above). The selected number of sampled FID points was 10, in order to speed up simulations.

According to previous considerations, the Nyquist frequencies was $2.1 \times 150 \text{ Hz} = 315 \text{ Hz}$, and the dwell to be set in the script was $\frac{1}{315 \text{ Hz}} = 3.2 \text{ ms}^3$.

Same considerations were done to find the B_1 minimum resolution, i.e., the minimum increasing step for the pulse length to obtain the minimum resolution after the inversion, following the N-S theorem. In other words, the step for varying the pulse length represents the time interval between two consecutive pulse lengths in an ANGLE experiment.

Thus, knowing that frequency is given by $\nu_1 = \gamma B_1$, where γ and B_1 were fixed (respectively $42.58 \frac{\text{MHz}}{\text{T}}$ and 1 mT), according to N-S theorem, the maximum frequency was $\gamma \times 1.2 \times B_1$ (1.2 indicated the maximum value of B_1 applied with respect to the nominal value). Hence, the pulse step was given by

$$\text{pulse step} = \frac{1}{2.1 \cdot \gamma \cdot 1.2 \cdot B_1} = 9.32 \cdot 10^{-6} \text{ s} \quad (3.1)$$

where the maximum frequency was multiplied by 2.1 according the N-S theorem⁴. Thus, the value obtained was $9.32 \mu\text{s}$. The code in which this parameter is set it is shown in Appendix B, in the section of sequence parameters (row 12), where there also are set the starting pulse length (row 11), and the total length of sequence (row 13). This last parameter was varied during first investigations.

³For tests with the distribution centered at 100 Hz , the maximum frequency considered was 250 Hz , and correct value of dwell was computed following the same procedure.

⁴Same considerations were done for the distribution shifted along B_1 axis, where the maximum frequency only corresponded to the product of γ and the magnetic field

In the case of ANGLE simulation, the signal relaxation during the application of the pulse must be taken into account. Hence, a modified version of the main code, in which pulses are considered as soft-pulses, i.e., as the sum of multiple short pulses, is used. After each of this short pulses there is a relaxation.

In the Matlab code, *the main pulse is not simulated as a single rotational matrix, but it is subdivided in many little rotational matrixes separated by delays where relaxation occurs*. This delay is specified in the code using the `dwell_pulse` parameter (which is in the commented line 8 of the example of a part of the ANGLE sequence code in the setting sequence parameters section in Appendix B). This feature allows to incorporate frequency sensitivity in simulations. Indeed, when using a rectangular pulses (that is the case for the experiment with the KEA-II console), the frequency bandwidth is $\Delta\nu = \frac{1}{t_p}$ (where t_p is the pulse duration). This is an important value to know since it gives a sense of what interval of frequencies (centered around the transmitting frequency ν) you are able to efficiently transfer energy to. Hence, `dwell_pulse` indicates time between these small pulses, where relaxation happens.

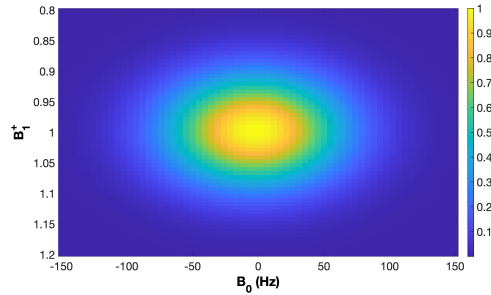
Moreover, in the Matlab code, it is possible to fix the number of short pulses in which the principle pulse is decomposed, instead to fix the value of dwell pulse. This is useful to speed up the simulation. In fact, if the dwell pulse is fixed and the selected maximum pulse length is very long, e.g., $600 \mu s$, the last pulse will have a pulse length of $600 \mu s$, and it will be decomposed in a large number of short pulses. This slows down the simulation. Hence, in the simulation, a fixed value of the number of short pulses which composed the principal pulse was selected (`n_sp = 100`).

Best parameters for ANGLE experiments

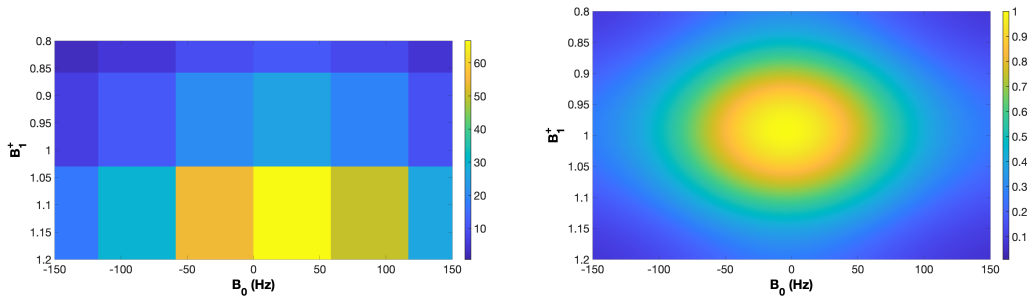
Once correctly set previous described parameters, ANGLE sequences were performed to investigate the best parameters for this experiment.

First tests were performed to investigate if the total duration of the ANGLE sequence affects results. Several tests were conducted, changing the value of the longest pulse length. Here, two representative cases are reported: the first one with the longest pulse length of $140 \mu s$ and the second one, with the longest pulse length of $560 \mu s$. This last case gave the best result.

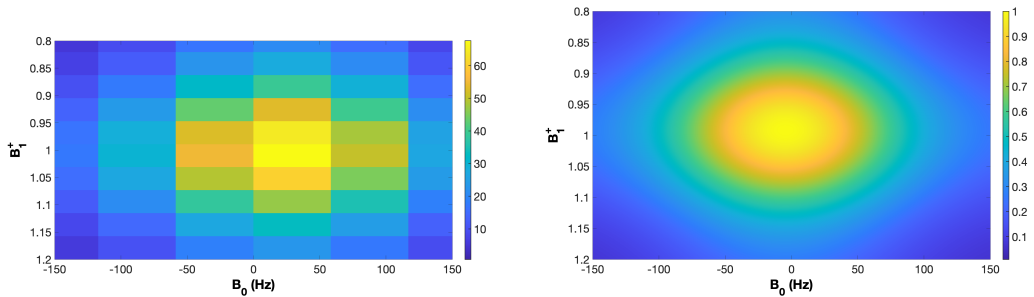
The value of the longest pulse length of the sequence affects results, as it is clear from Figures 3.8 and 3.9. In fact, according to the inverse proportionality between time and frequency, selecting a longer value for the last pulse length leads to acquire more information about the B_1 frequency component. Selecting $140 \mu s$ as the longest pulse length of the sequence, the extracted correlation maps are much larger than the ones in the case of $560 \mu s$. In addition, considering the second case (45° -shaped distribution), the reconstructed map presented a slope which seems to be different to 45° for the case of the longest pulse length of $140 \mu s$. For this reason, the value of $560 \mu s$ was fixed for the longest pulse length in the following ANGLE simulations. In the experimental case, this means that ANGLE sequence must be performed acquiring the maximum pulse length possible, according to device limitations.



(a) Correlation map in input.

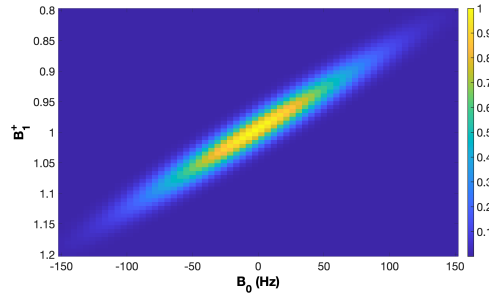
(b) Extracted map from ANGLE results.
Value of the longest pulse length = $140 \mu s$.

(c) Map (b) obtained after a 0-filling operation.

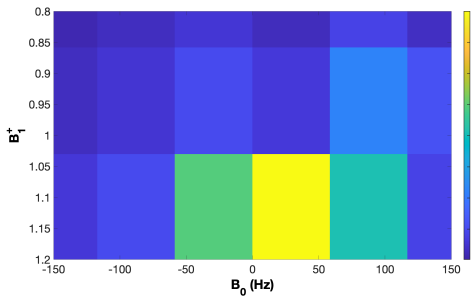
(d) Extracted map from ANGLE results.
Value of the longest pulse length = $560 \mu s$.

(e) Map (d) obtained after a 0-filling operation.

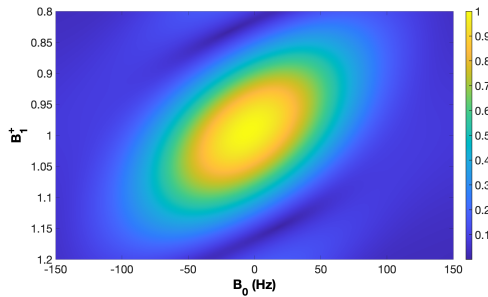
Figure 3.8: ANGLE simulations with parameters described in Section 3.2.1. Case of "classic" Gaussian distribution.



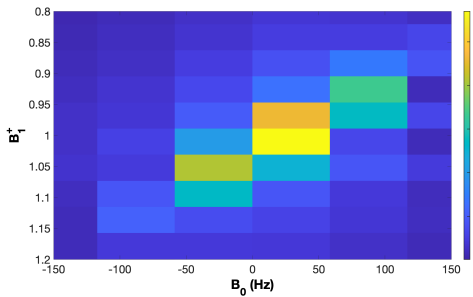
(a) Correlation map in input.



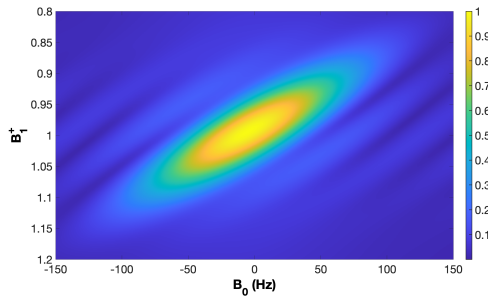
(b) Extracted map from ANGLE results.
Value of the longest pulse length = $140 \mu s$.



(c) Map (b) obtained after a 0-filling operation.



(d) Extracted map from ANGLE results.
Value of the longest pulse length = $560 \mu s$.



(e) Map (d) obtained after a 0-filling operation.

Figure 3.9: ANGLE simulations with parameters described in Section 3.2.1. Case of 45° -shaped Gaussian distribution.

Once finding the suited value for the longest pulse length of the sequence, the other parameters described in the previous section were alternatively varied, keeping fixed all the other parameters. Also in this case, several tests were performed. Here, most representative results are shown.

The first changed parameter was the total duration of the FIDs, selecting first a total duration of 64 *ms*, and then a total duration of 160 *ms*. This value is varying in the code by selecting the number of sampled FIDs points, because the sampling rate is fixed (3.2 *ms*, calculated in the previous section). In particular, for the first case 20 sampled points were acquired, and for the second case 50 sampled points were acquired.

Then, the sampling rate (dwell time)⁵ and the increasing step for the pulse length⁶ were changed, always according to the N-S theorem. Greater values for the Nyquist frequencies were selected, multiplying maximum frequencies by 3.5, instead of 2:

$$\begin{aligned} dt &= \frac{1}{3.5 \cdot 150 \text{Hz}} = 1.9 \text{ms} \\ \text{pl_step} &= \frac{1}{3.5 \cdot \gamma \cdot 1.2 \cdot B_1} = \frac{1}{3.5 \cdot 42.58 \frac{\text{MHz}}{T} \cdot 1.2 \cdot 1 \text{mT}} = 5.59 \mu\text{s} \end{aligned} \tag{3.2}$$

Finally, size of the map was changed in output. A resizing was performed after the reconstruction, extending the dimension to 128×128 .

It is important to repeat that in each test, only the described parameter was changed, keeping fixed all the other ones.

All results are shown in Figures 3.10 and 3.11.

From these results, the best parameters to extract the correlation map, making a tradeoff between final resolution and computational time needed by simulations, were:

- Longest pulse length for the ANGLE sequence = 560 μs ;
- Sampling rate (or dwell) for the FID = 3.2 *ms*.
- Increasing step for the pulse length = 9.32 μs ;
- Map dimension after the ANGLE simulation = 64×64 ;
- Total duration of the FID = 64 *ms* (the difference between this case and the case with the total duration of 160 *ms* led to equal results, so, to speed up simulations smallest value was selected).

At this point, the $B_0 - B_1$ correlation maps, obtained by exploiting the optimized parameters, were tested. However, the small dimensions of the map led to not satisfactory results. A map of dimension 512×1536 (where 512 corresponded to the B_1 component dimension, while 1536 corresponded to the B_0 component dimension) was finally selected after other tests, because these represented the correct minimum dimensions which allow to reach satisfactory results.

⁵*dt* in the Matlab script.

⁶*pl_step* in the Matlab script.

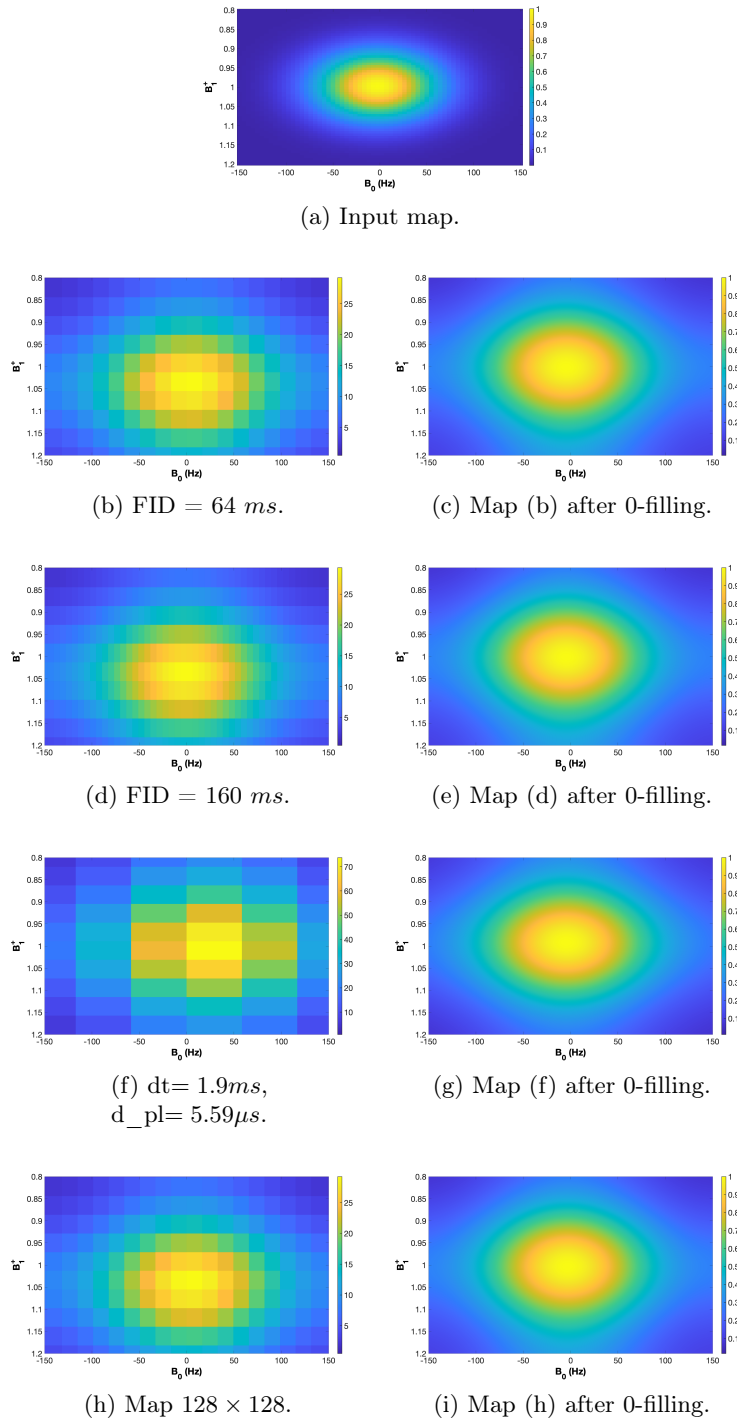


Figure 3.10: ANGLE simulations. Total duration $560 \mu s$. Case of "classic" Gaussian distribution.

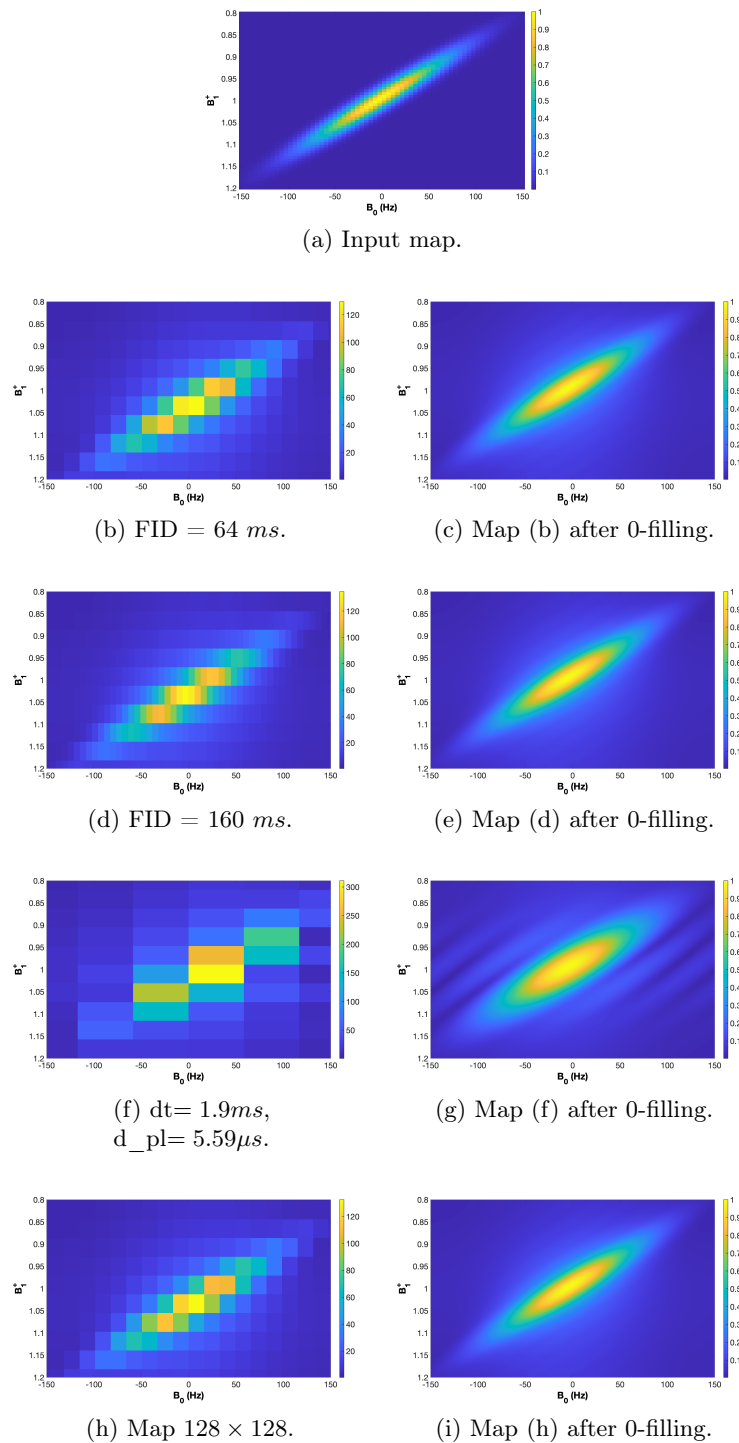


Figure 3.11: ANGLE simulations. Total duration 560 μ s. Case of 45°-shaped Gaussian distribution.

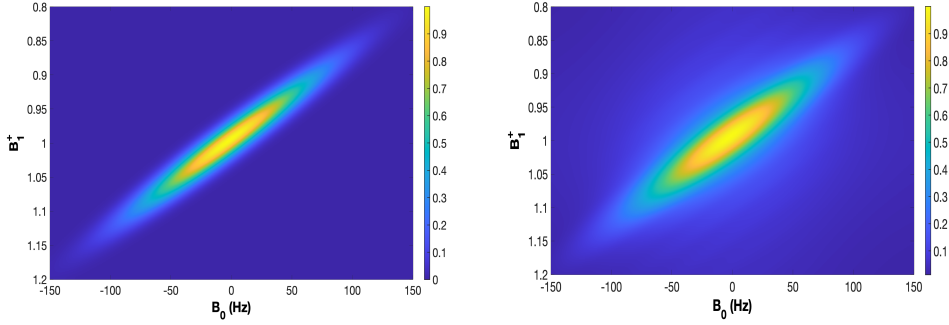


Figure 3.12: Comparison between maps before (on the left) and after ANGLE (on the right). Case of 45°-shaped Gaussian.

The Ground truth map and the reconstructed map post-ANGLE used to simulate all following tests are shown in Figure 3.12. Only the 45°-shaped Gaussian distribution for the correlation map was used. The post-ANGLE map was obtained by performing the ANGLE simulation using the final parameters defined above, except for the dimension of the map, which was resized to 512×1536 .

To quantitatively evaluate the performance of this approach (reconstruction of the correlation map), the full width at half maximum (FWHM) of the distributions were calculated to estimate the standard deviations of Gaussian distributions. This was performed considering the number of the pixels from the center, where the maximum value (1) of the distribution was expected, to the half of the maximum intensity, that in the color scale of the map corresponds to the green color pixels.

For the Gaussian distribution the standard deviation can be approximated as $\sim FWHM/2.35$. The ratio between the two correspondent sigmas (along each principal axis, i.e., 45° and 135°) was used to estimate the widening after the reconstruction. In this case, the sigma unit is the pixel.

Found values was the following ones:

- Ground Truth map
 - σ minor axis (135°) = 17.02 pixels;
 - σ maximum axis (45°) = 33.19 pixels.
- Post-ANGLE map
 - σ minor axis (135°) = 31.49 pixels;
 - σ maximum axis (45°) = 57.02 pixels.
- Minor axes ratio $\frac{\sigma_{pA}}{\sigma_{gt}} = 1.85$;
- Maximum axes ratio $\frac{\sigma_{pA}}{\sigma_{gt}} = 1.72$;

Hence, after the reconstruction, the correlation map resulted widens by a factor of $\sim 1.7/1.8$ along the two principal directions.

3.2.2 Constant bSSFP

Constant bSSFP sequences were simulated using first the LUT with the ground truth correlation map, and then using the LUT with the post-ANGLE correlation map. Signals were compared to individuate the best parameters to use then in the experimental sequence. The matching between ground truth signal and post-ANGLE one would have confirmed the efficacy of the $B_0 - B_1$ map reconstruction method.

Constant bSSFP investigations were conducted changing pulses flip angle, in order to check the influence of this parameter on the expected signal. In particular, flip angle was varied between 20° and 90° , with a 10° step. For each flip angle, the simulated signal were compared using the RMSE metric. RMSE was calculated on a limited number of points, considering all the transient phase and few points of steady state (first 50 echoes, $t=[0 - 5] \text{ ms}$). This was done because steady state values were close to zero value, thus a lower impact on RMSE was expected. Hence, the transient phase was more interesting to investigate. A good matching between first oscillations was requested.

The ground truth steady states and the post-ANGLE ones were compared, in order to see if there were evident differences. The last point of the analyzed signal was considered as the steady state value.

All the signal information was on the real part, hence all the analysis was performed using the normalized real part of the signals.

RMSEs and steady states as a function of flip angle are reported in Figure 3.13.

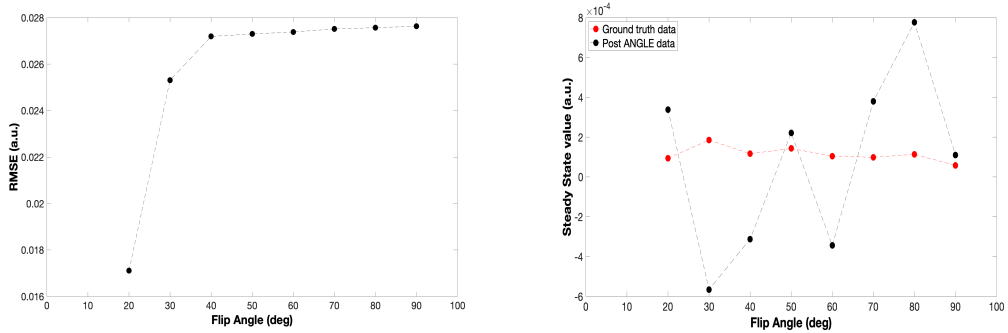
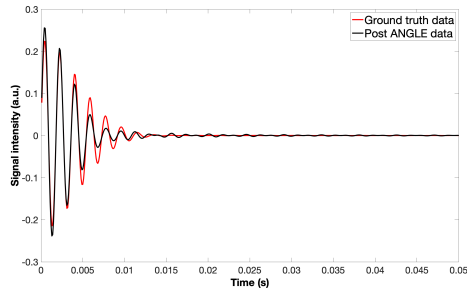


Figure 3.13: Comparisons between normalized ground truth real part of the signal and correspondent post-ANGLE one for the constant bSSFP sequence. On the left, RMSE value as a function of flip angle. On the right, steady state value as a function of flip angle.

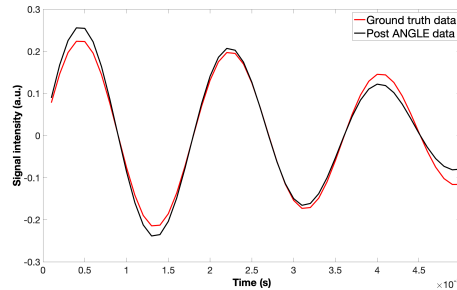
What emerged from these simulations was that using a lower flip angle, a best matching was reached. In particular, RMSE values were on the order of 10^{-2} and the lowest value corresponded to 20° flip angle ($\text{RMSE} = 0.0171 \text{ a.u.}$). The RMSE asymptotically tent to a value of 0.028 a.u. . Considering the steady state values, the post-ANGLE results qualitatively seemed to be more casual (see Figure 3.13 (b)), but observing the order of values it is clear that it should not impact the experiment, being on the order of the experimental noise.

In Figure 3.14 the comparison between bSSFP signals is shown for the 20° -pulse

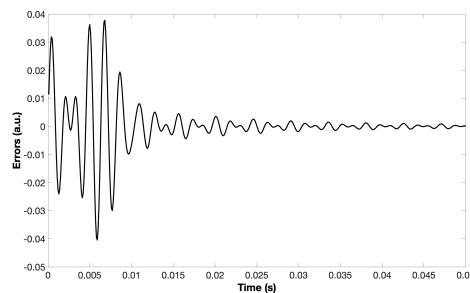
sequence case, which corresponded to the best result considering RMSE values. Moreover, a focus on first 50 echoes ($t=[0-5] \text{ ms}$) of the signal is reported in Figure 3.14 (b). Finally, the residuals, which were obtained from the difference between post-ANGLE signal and the correspondent ground truth one, are plotted in Figure 3.14 (c).



(a) Normalized ground truth real part of the signal compared to the post-ANGLE one.



(b) Focus of the signals on the first 50 echoes.



(c) Residuals.

Figure 3.14: 20° -pulse constant bSSFP simulations.

Results confirmed that a good matching was reached, although the transient phase showed more mismatched points respect to the steady state phase.

3.2.3 Alternate bSSFP

Simulations of the alternate bSSFP were then performed, conducting the same analysis of the previous case.

However, in this case, the normalized magnitude of the signals was used to perform the comparison, and the number of the first echoes on which the RMSE value was calculated was 120 ($t=[0-12] \text{ ms}$). RMSEs and steady states as a function of flip angles are reported in Figures 3.15.

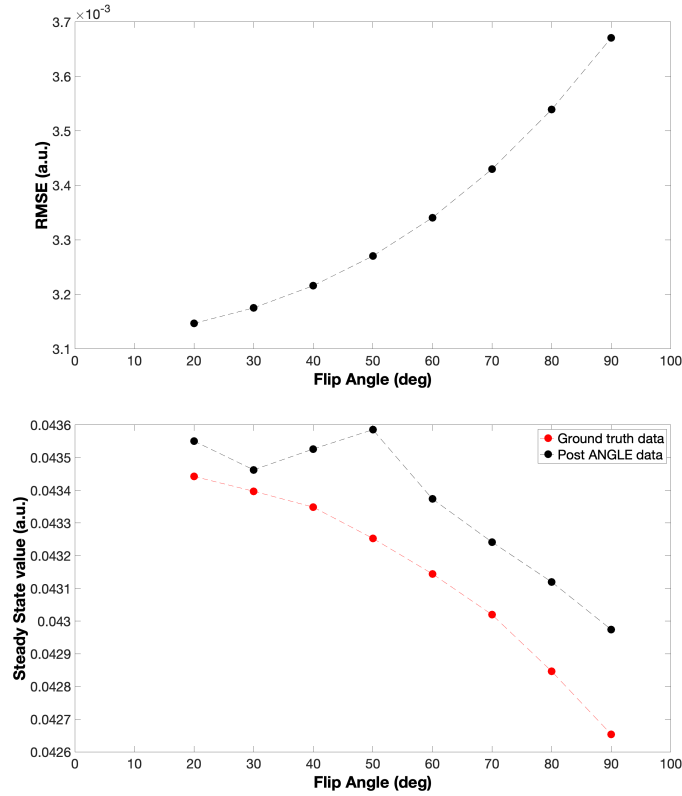


Figure 3.15: Comparisons between normalized ground truth magnitude of the signal and correspondent post-ANGLE one for the alternate bSSFP sequence. On the top, RMSE value as a function of pulses flip angle. On the bottom, steady state value as a function of pulses flip angle.

Using a lower flip angle, a best matching was reached also in the case of the alternate bSSFP. RMSE values were on the order of 10^{-3} and the lowest value corresponded to 20° flip angle (RMSE = 0.0031 a.u.), while the highest one, for 90° -pulse sequence corresponded to a value of 0.0037 a.u. . A better agreement is evident with respect to the constant bSSFP case. Steady states too seemed to behave in a better way, with post-ANGLE signal points which followed the same trend of correspondent ground truth ones (Figure 3.15 on the bottom). Considering the order of them, these fluctuations could be probably lower than the noise level in the experimental case.

Here, in Figure 3.16 best result is reported, considering (a) the signals, (b) a focus on first 120 oscillations ($t=[0 - 12] \text{ ms}$), and (c) the residuals.

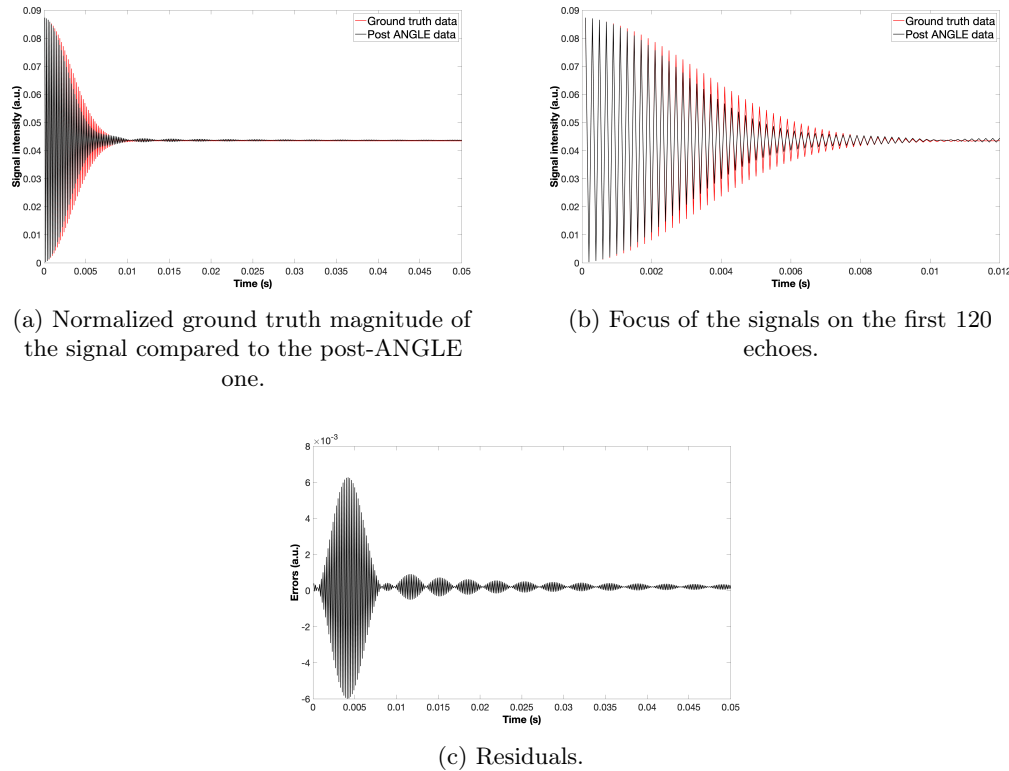


Figure 3.16: 20°-pulse alternate bSSFP simulations.

From the order of residuals it is clear that this sequence is more robust than the correspondent one with the constant phase. The only evident disagreement was manifested by the fact that in ground truth signal the oscillations have a greater amplitude with respect to ones of the post-ANGLE signal. This is due to the approximation with which the correlation map after the ANGLE simulation was reconstructed.

3.2.4 MRF

Finally, an investigation about MRF sequence was performed to individuate the best parameters to use then in the laboratory acquisition. In order to simulate the relaxation characteristics of the real sample, relaxation times were changed. Once decided that the case of study in laboratory would have been a rubber sample, an estimate of relaxation times was found in literature, with $T_1 \approx 35 \text{ ms}$ and T_2 on the order of 10 ms [61]. Correlation maps remained the same for the ground truth LUT and the post-ANGLE one. Simulations were conducted using these LUTs, and correspondent signals were compared to find the best parameters for this sequence to use later in the laboratory acquisition.

The MRF sequence was based on an IR-bSSFP sequence, where only a flip angle pattern was applied. The value of the repetition time, TR, for all pulses was fixed during

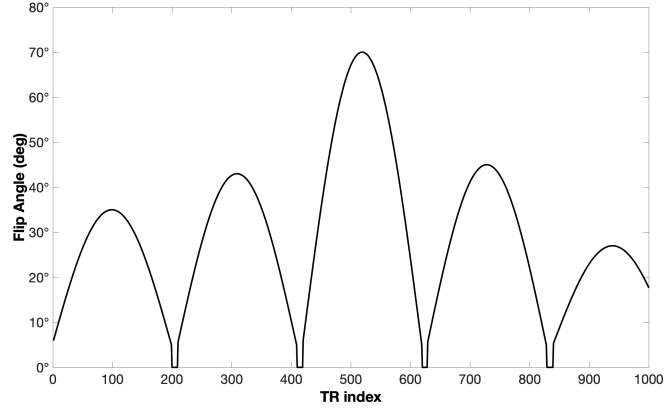


Figure 3.17: Flip angle pattern used for simulations.

the simulation. More complicated sequence can be implemented, using variable TRs, but it is not the case of this thesis work.

To investigate the relationship between the timing parameter TR of the sequence and the relaxation time T_2 of the sample, several tests were performed varying both TR and T_2 .

The flip angle pattern used for all simulations is shown in Figure 3.17. This is one of the standard flip angle pattern used in MRF-based implementations for MRI [2].

Selected TR values for simulations were: TR = 100 μ s, TR = 1 ms, TR = 10 ms and TR = 100 ms. For each TR value, simulations varying T_2 were performed, with values: $T_2 = 1$ ms, $T_2 = 5$ ms, $T_2 = 10$ ms, $T_2 = 15$ ms, $T_2 = 20$ ms, $T_2 = 25$ ms, $T_2 = 30$ ms and $T_2 = 35$ ms. RMSE values as a function of T_2 and as a function of TR is reported in Figures 3.18. RMSE values were calculated on normalized magnitude of the signals.

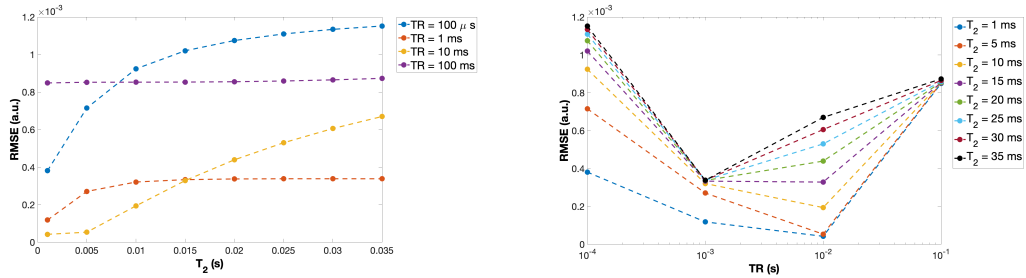


Figure 3.18: RMSE values for the MRF-based sequence simulations. On the left, RMSE values as a function of T_2 values for each TR values. On the right, RMSE as a function of TR values for each T_2 values.

In the case of RMSE values as a function of T_2 (Figure 3.18 on the left), once fixed TR value for simulations, a constant trend was found. In fact, considering TR = 100 μ s, and TR = 1 ms, RMSEs asymptotically tent to $1.2 \cdot 10^{-3}$ a.u., and $0.3 \cdot 10^{-3}$ a.u.

respectively. While, for $TR = 100\text{ ms}$, the RMSE value was about $0.8 \cdot 10^{-3}\text{ a.u.}$ for all T_2 values. Only for $TR = 10\text{ ms}$, increasing the T_2 the RMSE increased too.

Considering the case of RMSE values as a function of TR, fixing the T_2 values, the lower RMSEs were reached in correspondence of $TR = 1/10\text{ ms}$ as it is shown in Figure 3.18 on the right. RMSE values in both graphs are very low, on the order of 10^{-3} , so a good matching between signals would be expected.

Here, two comparisons are presented, one corresponding to the lowest RMSE value measured, obtained for $TR = 10\text{ ms}$ and $T_2 = 1\text{ ms}$: $RMSE = 4.2 \cdot 10^{-5}\text{ a.u.}$; the other one was selected taking the case with the lowest RMSE value for T_2 value fixed to 25 ms , because this value is the expected one for rubber sample: $RMSE = 3.38 \cdot 10^{-4}\text{ a.u.}$. The correspondent value of the TR was 1 ms . Results are shown in Figures 3.19 and 3.20.

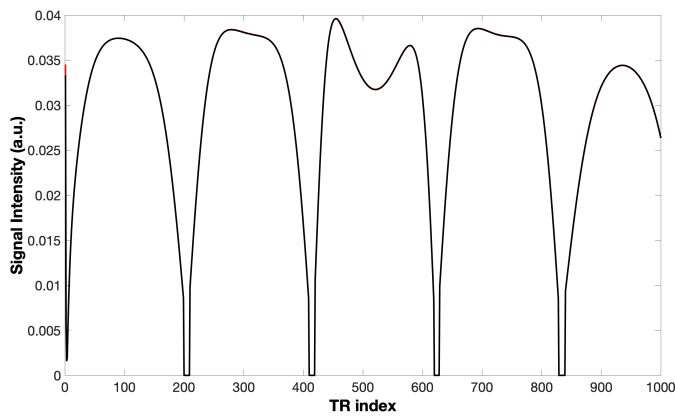


Figure 3.19: Normalized ground truth magnitude (in red) compared with the post-ANGLE one (in black) for a MRF-based sequence, with $TR = 10\text{ ms}$ and $T_2 = 1\text{ ms}$.

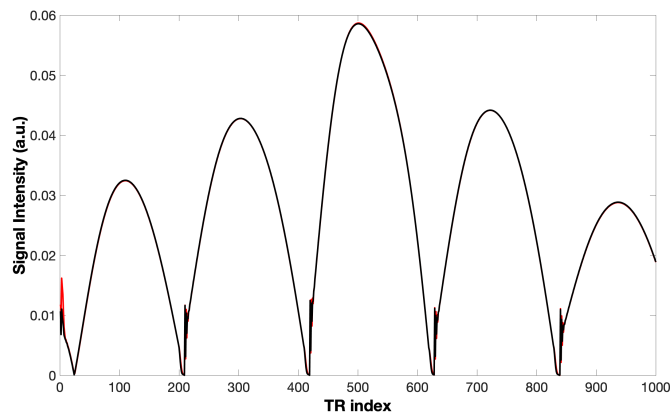


Figure 3.20: Normalized ground truth magnitude (in red) compared with the post-ANGLE one (in black) for a MRF-based sequence, with $TR = 1\text{ ms}$ and $T_2 = 25\text{ ms}$.

It is evident from Figures 3.19 and 3.20 that a perfect match was obtained. The red part, correspondent to the ground truth data is not visible, except for the very first points, where the sequence has just applied the 180° -pulse of IR sequence to the sample. Finally, it is important to point out that in the first plot (Figure 3.19), where $T_2 < TR$, the T_2 relaxation effects are visible on the modulation of the acquired signal, while in the second plot (Figure 3.20), where $TR \ll T_2$, the T_2 modulation is lost, and the signal follows the flip angle pattern.

3.3 Case of study: Rubber

Once validated the sequences and parameters, experimental acquisitions were performed and compared to the simulated results for all sequences described in this thesis work. The final goal of this thesis work was to validate the MRF-based sequence, which was programmed on the KEA console ex novo. The sequences used for this rubber sample were: ANGLE, FID 1-Pulse, Inversion Recovery, CPMG, Constant and Alternate bSSFP (with several flip angles), and finally the MRF sequence, based on the IR-bSSFP.

The rubber used as a sample was a piece of common eraser rubber. The values of relaxation times were computed using UpenWin software described in Section 2.3.1. The time distributions obtained are reported in Figure 3.21. The values were calculated as the geometric mean of the peak values, obtaining $T_1 = 51.7 \text{ ms}$ and $T_2 = 2.59 \text{ ms}$. These values were entered in the LUT used to perform all simulations.

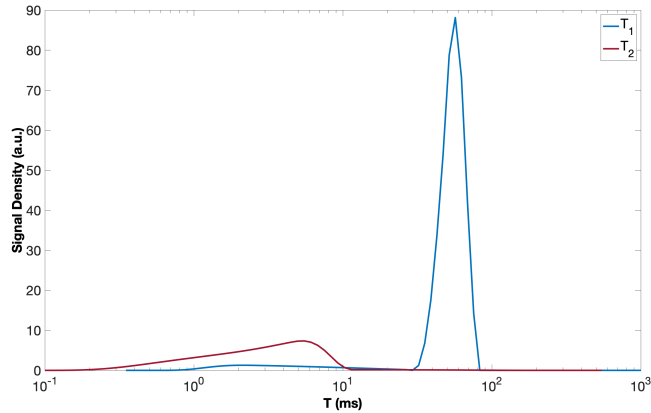


Figure 3.21: Relaxation times distributions of the rubber sample obtained by UpenWin Software. The values were calculated as the geometric mean of the peak values, obtaining $T_1 = 51.7 \text{ ms}$ and $T_2 = 2.59 \text{ ms}$.

3.3.1 $B_0 - B_1$ distribution

At this point, The ANGLE experiment was performed, using the optimized previously investigated parameters to reconstruct the $B_0 - B_1$ correlation map for the rubber sample. After acquiring the ANGLE signal, data were analyzed with methods described

in Section 2.3.4. Acquired signal is reported in Figure 3.22, where on the top figure all FIDs are plotted in a 3D plot, and on the bottom figure the peak integral is shown. The ANGLE sequence was acquired starting with a pulse length of $0.5 \mu s$ and ending with a pulse length of $100 \mu s$, with an increasing step for the pulse length of $2 \mu s$. While, the selected sampling rate for the FID was $12.5 \mu s$. Repetition time selected was $1 s$.

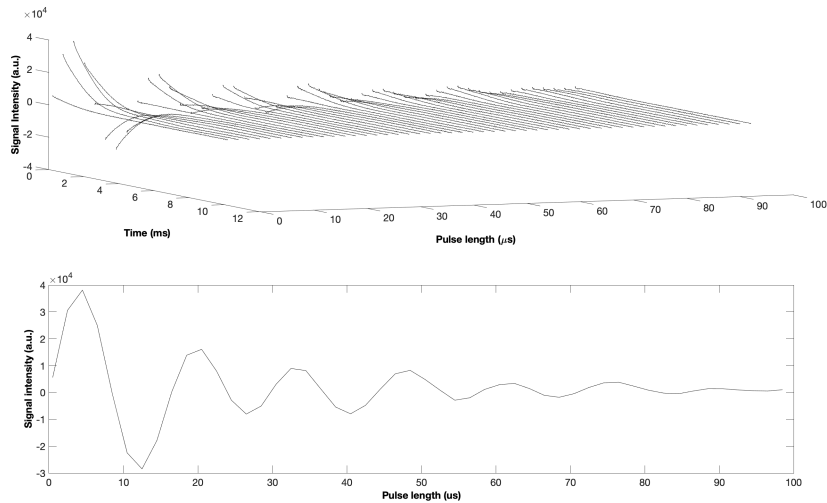


Figure 3.22: Acquired ANGLE signal. On the top, all FIDs are reported. On the bottom, the peak integral is reported.

To describe the results of the $B_0 - B_1$ correlation map, the projections on the B_0 and B_1 axes were computed and reported in Figure 3.23 (B_1 distribution on the left, and B_0 distribution on the bottom). The range of the off-resonance frequencies was about $800 Hz$, while the range of the B_1 values was about 1.00 , which means that B_1 did not uniformly affected the sample, but the spins were flipped by a rotation with efficiency which followed the distribution showed in figure. These results were credible. The complete final map inverted and resized (512×1536^7) is shown in Figure 3.23. This map was used to create the LUT, which was used to perform all simulations.

⁷Where 512 corresponded to the B_1 component dimension, while 1536 corresponded to the B_0 component dimension.

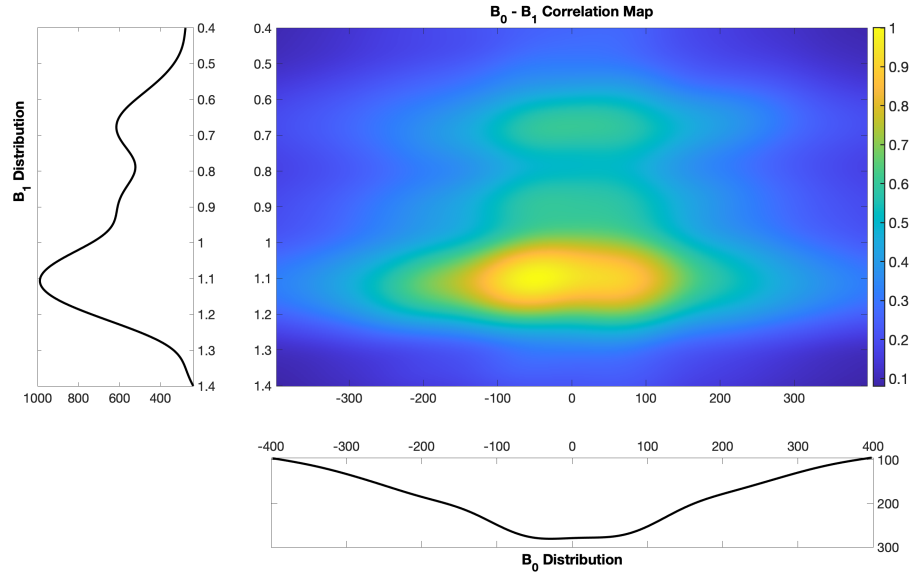


Figure 3.23: $B_0 - B_1$ correlation map of the rubber sample. The final dimension after a resizing is 512×1536 (512 for B_1 components, and 1536 for B_0 ones). On the left there is the B_1 distribution, while on the bottom there is the off-resonance distribution.

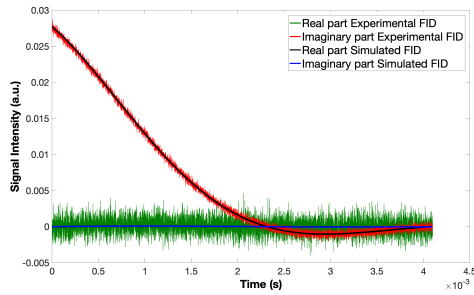
The obtained map consisted of a main component (with B_0 value in the interval $[-100Hz, +100Hz]$, and B_1 value in the interval $[1 - 1.2]$), and two lower intensity features in the same range of B_0 but at different B_1 (B_1 value in the intervals $[0.6 - 0.7]$, and $[0.85 - 0.95]$).

Finally, the LUT was created using all extracted parameters and the simulations of all the sequences of interest were performed to compare the obtained results with the correspondent experimental ones. These comparisons are shown in the next subsections.

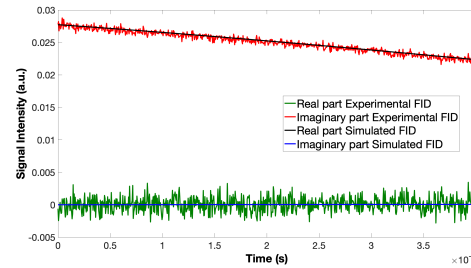
3.3.2 FID 1-Pulse

The experimental FID signal was acquired selecting the following main parameters: repetition time = 2.5 s; sampling rate = 0.5 μs ; number of acquired points = 8192; number of scans = 8; and pulse length for the 90° pulse = 6 μs . The simulation was performed using the same values for the correspondent parameters.

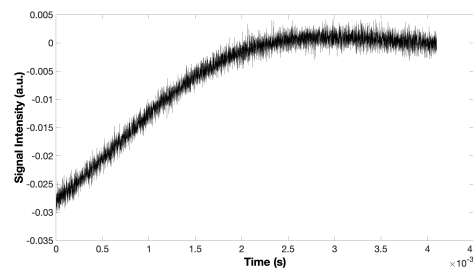
Here, in Figure 3.24, the comparison between normalized real and imaginary part of the signals is reported.



(a) Normalized experimental real and imaginary part of the signal compared to the simulated ones.



(b) Focus on the first 800 points of the signals.



(c) Residuals between real part of the signals.

Figure 3.24: Experimental and simulated results for the rubber sample in the case of FID 1-Pulse.

In Figure 3.24 (b) a focus on the first 800 points ($t = [0 - 0.4] \text{ ms}$) is shown, while in Figure 3.24 (c) the residuals (which were calculated subtracting the simulated signal values from the experimental correspondent ones) are reported. Only residuals between real part of the signals were plotted, because all information was stored on this part, while imaginary parts were averaged on 0.

A great agreement was reached, as it is visible from the order of residuals, even for the first points, where for the EDTA sample there had been a mismatching (see Figure 3.4) due to a non correct $B_0 - B_1$ correlation map reconstruction. The RMSE values was obtained comparing normalized signals. The value obtained was 0.0110 a.u. , thus on the order of 10^{-2} . Hence, this quantitatively confirms that the agreement reached was very good.

3.3.3 Constant bSSFP

Many constant bSSFP experiments were performed in laboratory, changing the pulse flip angle value. The values used were 20° , 30° , 50° , 80° , and 90° . Moreover, the following main parameters were selected for the experimental acquisitions: repetition time = 2.5 s ; sampling rate = $0.5 \mu\text{s}$; number of echoes acquired = 1000; pulse length for the 90° pulse = $6 \mu\text{s}$; and number of scans = 128.

The script of this sequence on the KEA console is based on the pulse length, which means that it is necessary to change the pulse length value to select a different pulse flip angle value. From a trivial proportion, the correspondent selected pulse length values were: $1.33 \mu s$, $2 \mu s$, $3.33 \mu s$, $5.33 \mu s$ and $6 \mu s$ for the 20° pulse, the 30° pulse, the 50° pulse, the 80° pulse, and the 90° pulse respectively.

The simulations were performed selecting the same experimental values for the correspondent parameters.

At this point, for each flip angle, RMSE value was calculated using the normalized real part of the signals (because all signal information was stored on that part), only considering the first 40 echoes ($t = [0 - 4] ms$). The comparison was performed only considering the transient phase and few points of steady state, because a focusing on the first oscillations was more significant. All RMSE values were plotted as a function of pulse flip angle values (Figure 3.25).

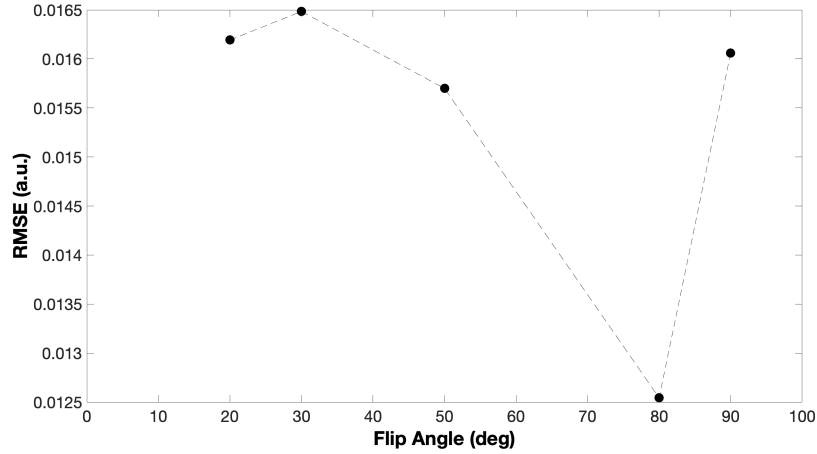


Figure 3.25: RMSE values as a function of pulse flip angles for the constant bSSFP sequence.

The order of these values is very low, i.e., 10^{-2} . This quantitatively confirmed that a very good agreement was reached.

In addition, this agreement between experimental and simulated results is qualitatively shown in Figure 3.26, where the case for the lowest RMSE value is reported. This corresponds to the case with the flip angle of 80° , where the RMSE was $0.0125 a.u.$. It is evident that a very good matching was obtained, except for few oscillations, but this can be explained by the random fluctuations due to the noise in the experimental case. Moreover, a good matching was obtained in all cases considered. A focus on the first 40 echoes ($t = [0 - 4] ms$) of normalized real part of the signals is shown in Figure 3.26 (b). Finally, the residuals between normalized real part of the signals are shown in Figure 3.26 (c). The order of residuals represents another indicator that shows that a very good agreement was reached.

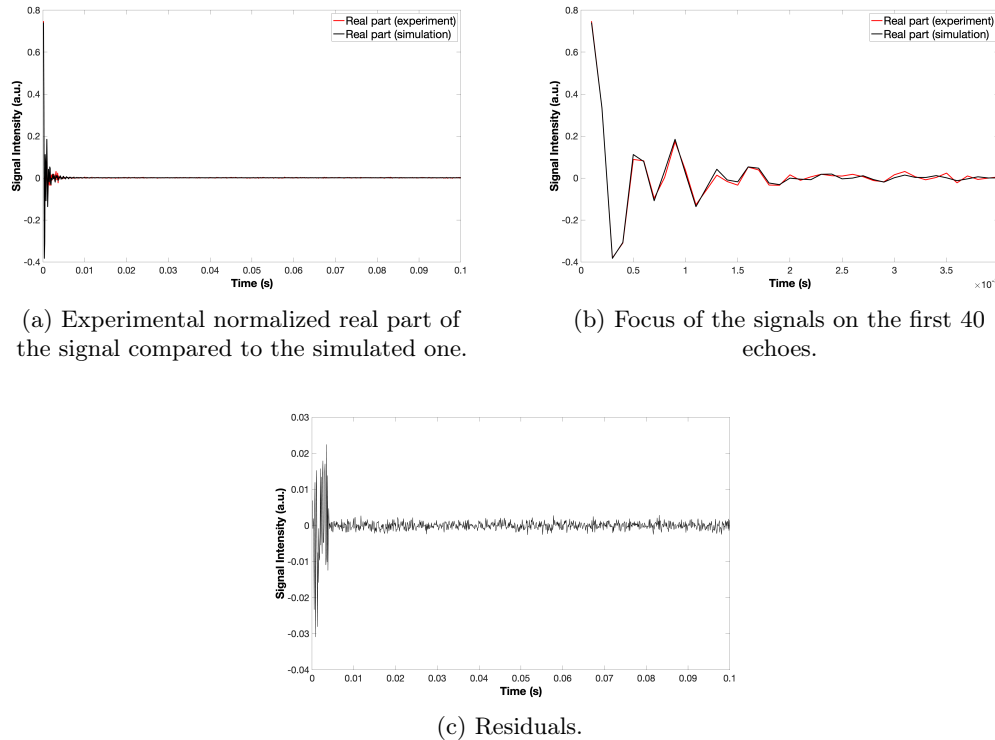


Figure 3.26: 80°-pulse constant bSSFP.

It is important to recall the best result for the EDTA case in order to compare it with the obtained result in this different case. In the EDTA case, the $B_0 - B_1$ correlation map was not extracted. Only the off-resonance distribution was reconstructed, while the B_1 distribution was approximated with a linear distribution. The best RMSE value in the EDTA case (0.1585 *a.u.*) was one order greater than the RMSE value in the rubber case. Moreover, in the EDTA case, the transient oscillations showed a sort of dephasing. While, in the rubber case, a very good matching was obtained. These results confirm the necessity to extract the $B_0 - B_1$ correlation map, and they represent a validation for the programmed sequence on the KEA console.

3.3.4 Alternate bSSFP

Many alternate bSSFP experiments were performed in laboratory, changing the pulse flip angle value also in this case. The selected values for the main parameters of the sequence were the same of the constant bSSFP case.

The simulations were performed selecting the same experimental values for the correspondent parameters.

The RMSE values were calculated using the normalized magnitudes, considering that the real part of the signals gave the same results (because all signal information was

stored on that part). Only echoes in the time interval $t = [0 - 4] \text{ ms}$ (first 40 echoes) were considered to obtain RMSE values, focusing on transient phase oscillations and few points of steady state. These values as a function of pulse flip angle are shown in Figure 3.27.

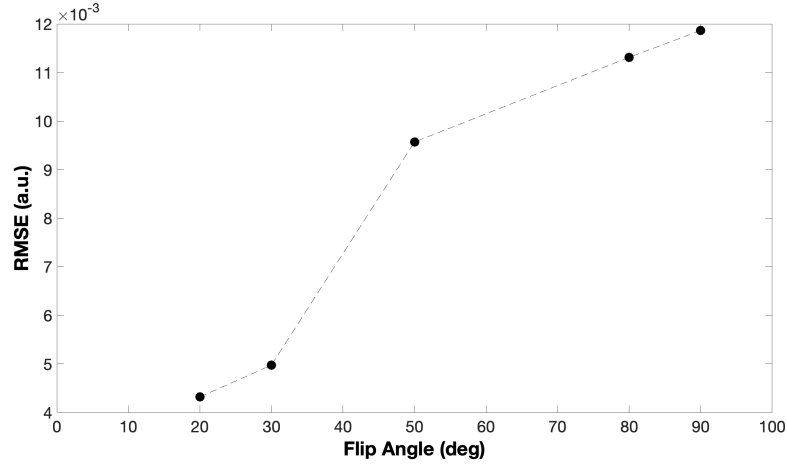


Figure 3.27: RMSE values as a function of pulse flip angles for the alternate bSSFP sequence.

In this case, values were on the order of 10^{-3} , one order less than the correspondent case with the constant phase. Hence, this result quantitatively confirmed a very good agreement between experimental and simulated signals. A good matching between signals was obtained in all cases. Moreover, the lowest RMSE value was 0.0043 a.u. , and it was obtained with a flip angle of 20° . For this case, the comparison between normalized real part of the experimental signal and the simulated one is shown in Figure 3.28 on the left, while the comparison between normalized magnitudes is shown in Figure 3.28 on the right. It is also qualitatively evident from these plots that a very good matching between experimental and simulated results was obtained.

A focus on the first 40 echoes ($t = [0 - 4] \text{ ms}$) of the signals, and the residuals (obtained subtracting the simulated values from the experimental ones) are shown in Figure 3.29, and Figure 3.30 respectively.

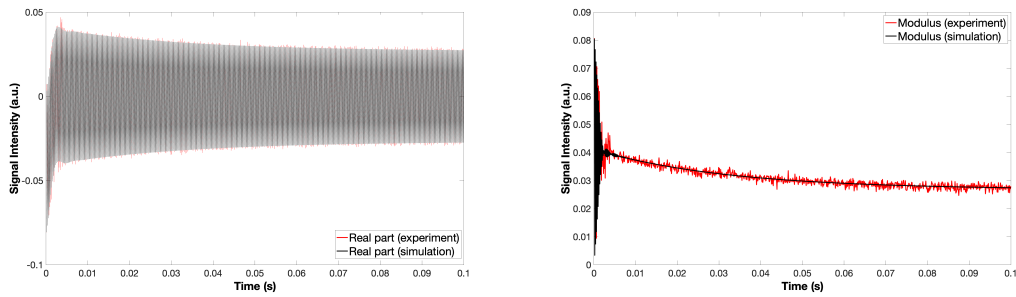


Figure 3.28: Experimental and simulated results for the rubber sample in the case of 20° -pulse alternate bSSFP. On the left, the comparison between normalized real part of the signal. On the right, the comparison between normalized magnitudes.

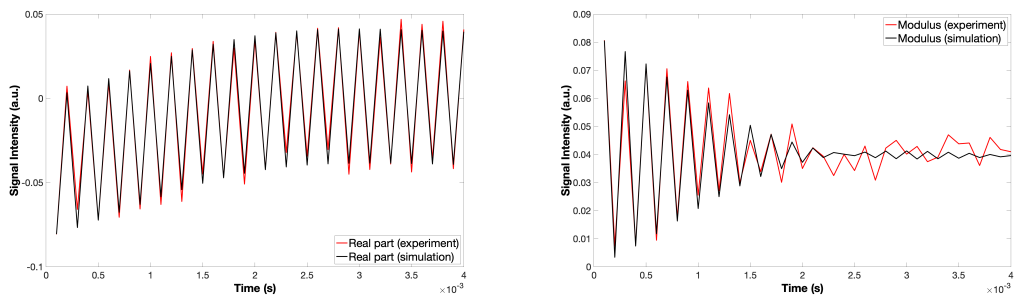


Figure 3.29: Focus of the signals in Figure 3.28 on the time interval $t = [0 - 4] \text{ ms}$.

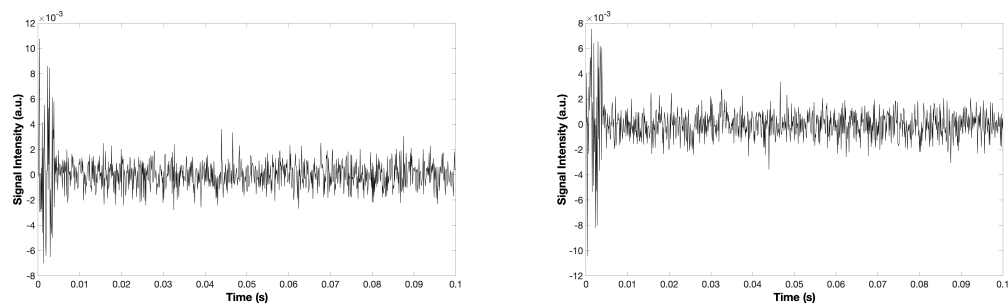


Figure 3.30: Residuals between signals in Figure 3.28.

Considering the residuals order and the order of RMSE values, it can be concluded that the alternate bSSFP showed a better agreement between experimental and simulated signals with respect to the constant bSSFP. Finally, these results represent a validation for the programmed sequence on the KEA console.

3.3.5 MRF

All previous sequences were preparatory to implement an MRF-based sequence on KEA console. The first challenge was to program it using Prospa language. The sequence considered was based on an IR-bSSFP, thus the first pulse is a 180° pulse, which flip the magnitude on the z -axis, and then a train of pulses following a specific flip angle pattern is applied. All pulses had to be specified in the main script of the sequence (`pp.mac` file).

Firstly, the maximum number of parameter that can be written in the memory of the console was found in order to avoid errors. After several tests, in the MRF sequence 96 radio frequency pulses were programmed. The best way to produce the RF pulses with the KEA console, is to vary the amplitude of the pulse fixing the pulse length. The amplitude is specified by the decreasing in power, dB (with the minus sign), as said in Section 2.1.1.

The flip angle pattern selected for the sequence was based on the one found in literature, which is largely used in MRI [2]. However, the pattern was scaled for our purpose, considering only angles greater than 5° and selecting a limited interval. Flip angle pattern used is showed in Figure 3.31.

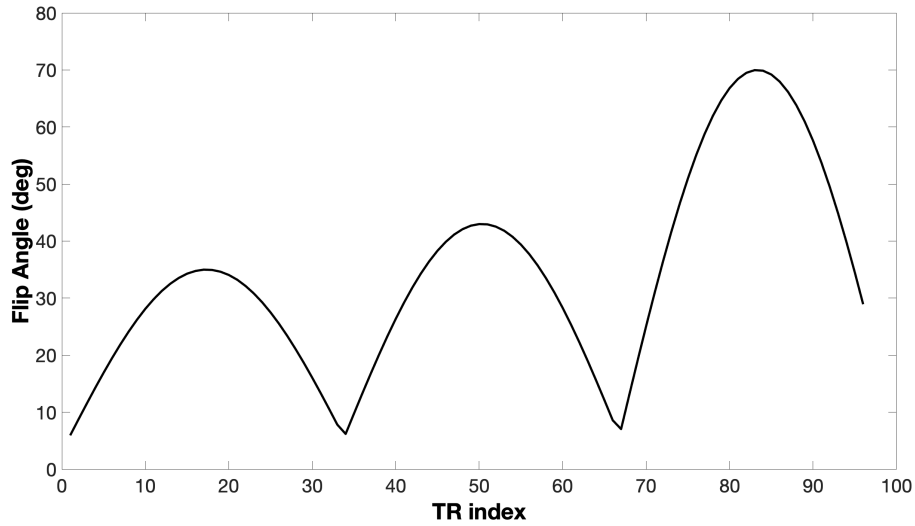


Figure 3.31: Flip angle pattern used to program MRF-based sequence.

Once selected the flip angle pattern, the decreasing in power was found for each angle starting from the Equation 2.2, where the experimental result corresponded to $-13.8 dB$, which means that a value of $-13.8 dB$ for the amplitude is necessary to select a 90° pulse in the KEA console. At this point, replacing that result in the Equation 2.3:

$$W_X = \left(\frac{X}{90}\right) \cdot W_{90} = 20 \cdot \log_{10}\left(\frac{X}{90}\right) + 20 \cdot \log_{10}\left(\frac{V_{90}}{V_0}\right) = 20 \cdot \log_{10}\left(\frac{X}{90}\right) - 13.8 \text{ dB} \quad (3.3)$$

the power attenuation values for each flip angle were computed.

The sequence was designed defining each pulse in terms of power attenuation, and fixing the pulse length (for the 90° pulse, the value was $6 \mu s$). A commented example of this designed sequence is shown in Appendix A.

At this point, the GUI was created in order to select desired values for the parameters to perform the sequence.

After verifying that the sequence would work and it would have been possible to acquire consistent data, the following main parameters were selected to perform the experiment:

- -7.8 dB for the 180° pulse amplitude from Equation 3.3;
- $5 \mu s$ for the sampling rate;
- 96 echoes (one for each flip angle);
- 128 scans to increase the signal to noise ratio;
- 1.2 s for the repetition time.

The same values were used for the simulations.

Once acquired the experimental signal, the idea was to compare it with different simulated signals, which were obtained varying relaxation times in the LUT in order to validate the sensitivity of the sequence in distinguishing different T_1 and T_2 , i.e., different materials. T_1 and T_2 values for the rubber sample obtained from inversion recovery and CPMG sequences were 51.7 ms and 2.59 ms respectively. Thus, keeping fix the relaxation times ratio ($51.7/2.59 = 19.96$), four different LUTs were created, where only relaxation times were changed: the first one with measured values, the second one with $T_1 = 100 \text{ ms}$ and $T_2 = 5.01 \text{ ms}$, the third one with $T_1 = 10 \text{ ms}$ and $T_2 = 0.501 \text{ ms}$, and the last one with $T_1 = 1 \text{ ms}$ and $T_2 = 0.0501 \text{ ms}$. Correlation map values were all the same for different LUTs and they corresponded to the map extracted from ANGLE sequence (Figure 3.23).

The RMSE value was calculated to individuate the LUT which better fits experimental data. Obtaining the best agreement in correspondence of the LUT which used measured values for relaxation times, meant that MRF sequence was correctly programmed and this approach was providing consistent results.

Moreover, a simulation was performed using a LUT containing only one component, in order to compare the result with the best one obtained from the previous comparisons. The aim of this last comparison is to point out the importance of studying the $B_0 - B_1$ correlation map. Hence, the LUT had dimension 1×6 , where the "weight of the component" was set to 1, the off-resonance frequency was set to 0 Hz , the B_1 value was set to 1, the relaxation times were set to measured values, and D was set to $0 \text{ m}^2/\text{s}$.

The comparison between experimental and simulated signals to validate the sequence for assigning the correct relaxation properties of the sample is shown in Figure 3.32. A very good agreement was obtained, as it is evident from the plot. In addition, the RMSE value was $6.6 \cdot 10^{-3} \text{ a.u.}$, confirming the agreement from a quantitative point of view.

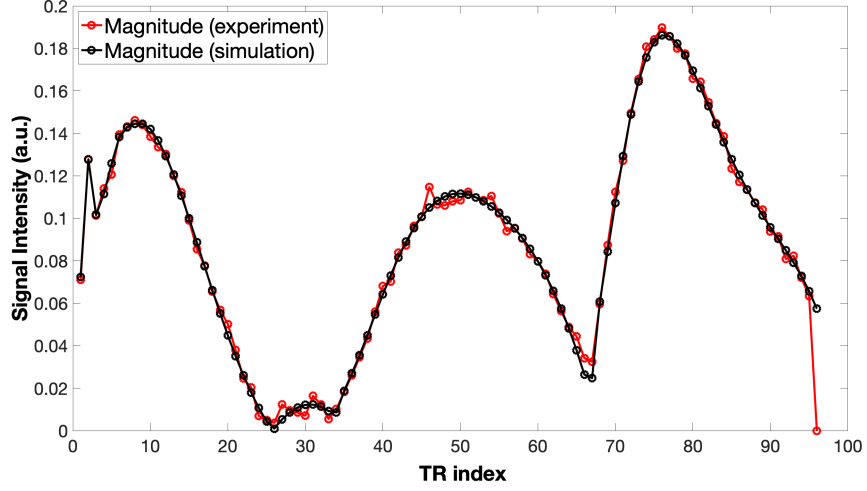


Figure 3.32: Comparison between experimental and simulated signals obtained for MRF sequence using flip angle pattern showed in Figure 3.31 and LUT for simulation with the measured relaxation time values.

The other comparisons between experimental and simulated signals obtained using LUTs with different values of relaxation times are shown in Figure 3.33. The agreement was not good for these cases, as it is visible from the plots. Moreover, RMSE values were greater than the value obtained for the case with the LUT using measured values of relaxation times. These values were on the order of 10^{-2} , and in particular RMSEs were:

- $6.25 \cdot 10^{-2}$ *a.u.* in the case of LUT with $T_1 = 100$ *ms* and $T_2 = 5.01$ *ms*;
- $5.36 \cdot 10^{-2}$ *a.u.* in the case of LUT with $T_1 = 10$ *ms* and $T_2 = 0.501$ *ms*;
- $4.08 \cdot 10^{-2}$ *a.u.* in the case of LUT with $T_1 = 1$ *ms* and $T_2 = 0.0501$ *ms*.

The obtained RMSE values are plotted in Figure 3.35, also considering the comparison between the experimental signal and the simulated one obtained using the LUT with one component.

The comparison between experimental signal and the simulated one obtained using the LUT with one component is shown in Figure 3.34. The agreement was not good also in this case, as we expected, confirming the necessity to extract the $B_0 - B_1$ correlation map to correctly conduct the simulations. The RMSE value obtained in this case was 0.0181 *a.u.*.

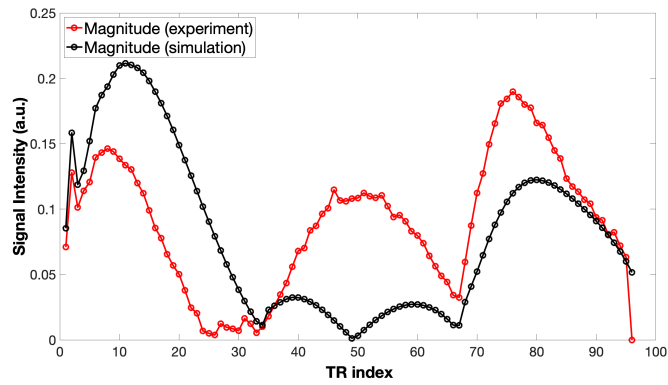
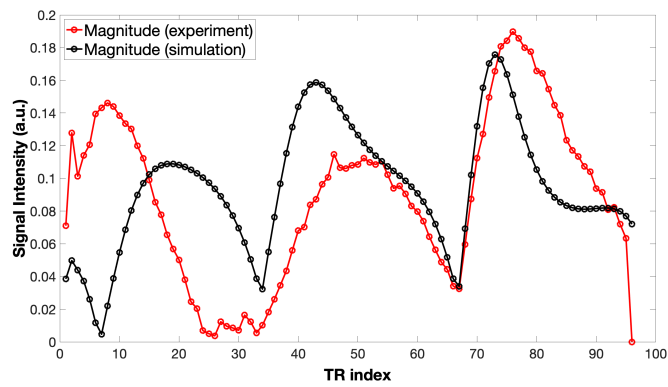
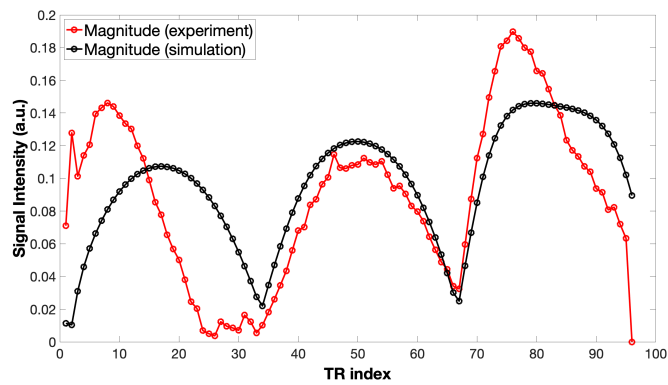
(a) LUT with $T_1 = 100 \text{ ms}$ and $T_2 = 5.01 \text{ ms}$.(b) LUT with $T_1 = 10 \text{ ms}$ and $T_2 = 0.501 \text{ ms}$.(c) LUT with $T_1 = 1 \text{ ms}$ and $T_2 = 0.0501 \text{ ms}$.

Figure 3.33: Comparison between experimental and simulated signals obtained for MRF sequence using flip angle pattern showed in Figure 3.31 and LUT with different relaxation time values.

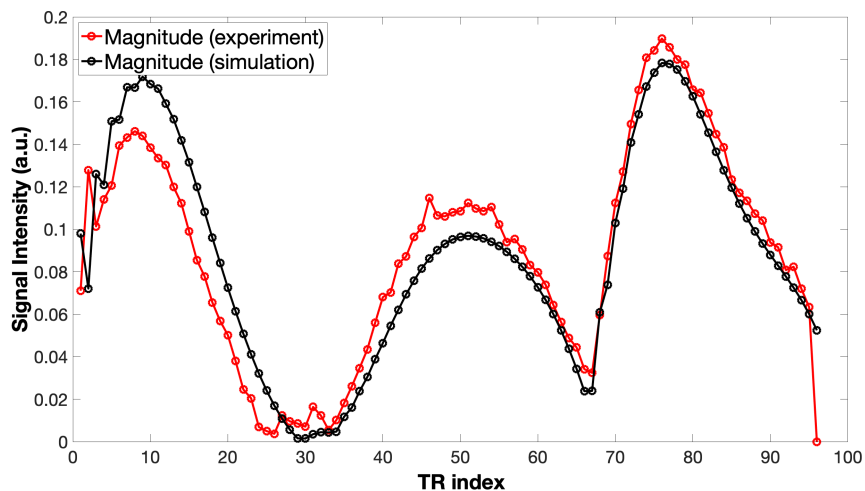


Figure 3.34: Comparison between experimental and simulated signals obtained for MRF sequence using flip angle pattern showed in Figure 3.31 and LUT with only 1 component.

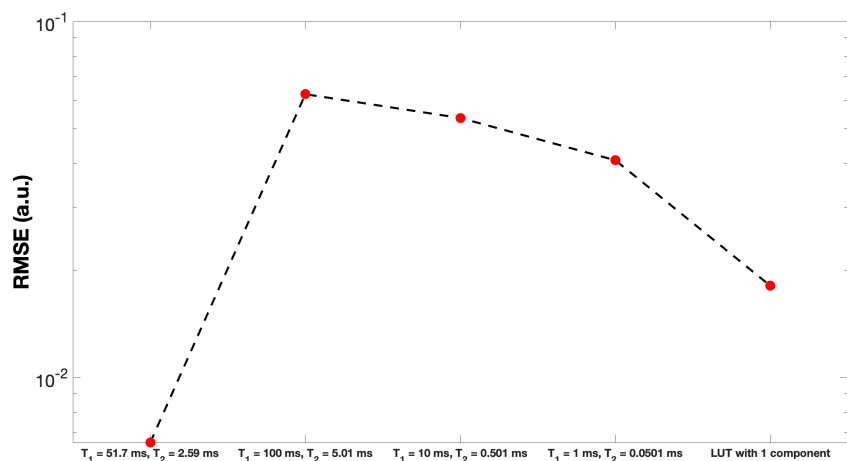


Figure 3.35: RMSE values obtained comparing experimental signal with different MRF simulated cases.

All performed tests validate the designed MRF sequence on KEA console. This sequence was programmed on this console *ex novo* and it was implemented for the low field NMR. Considering RMSE values and the plots, it can be concluded that the MRF sequence was correctly designed and programmed. Moreover, the approach of comparing the experimental signal with different simulated signals confirms the capacity of this specific sequence to individuate and to provide a correct estimation of relaxation times of the material under investigation. In fact, as described in Section 1.3, after acquiring

the signal with an MRF-based sequence, this is processed using a pattern recognition approach, which uses a dictionary to provide a correct quantitative measurement of some specific parameters of interest. In this thesis work, this phase was conducted in a direct way, analyzing the RMSE for each case and finally comparing them. A correct approach includes the creation of a suited pattern recognition algorithm, and the creation of a suited signal dictionary.

Finally, the comparison between experimental signal and the simulated one obtained with LUT consisting in one single spin confirmed the necessity to correctly determine the correlation of the $B_0 - B_1$ inhomogeneities of the instrument.

Conclusion

In this thesis work a MRF-based sequence was developed ex novo on low-field NMR.

The NMR theory with a focus on the influences of the inhomogeneity of the magnetic fields on the sample is presented on the first part of this work. At the end of this theoretical introduction, the magnetic resonance fingerprinting development up to the state of the art of it is summarized.

In the second part, the methods and the materials used for this work are presented. Firstly, the experimental setup is described, including the low field magnet, the coil, and especially the KEA console, which allows to program pulses sequences. Moreover, an overview on programming language of the console is reported. At this point, all sequences used and developed are described, focusing on the balanced steady state free precession sequence, which represents the base to develop an MRF-based sequence. A brief description of samples analyzed is also reported. All experimental results must be validated, thus simulations using a specific software were performed to obtain results to compare to experimental ones. The most important characteristics of this software were commented in this part. Some examples instead were reported in the Appendix. At the end of this part the data analysis methods were reported, including methods developed to extract information about $B_0 - B_1$ correlation maps, the metric used to compare simulations and experiments, and the UpenWin software, used to extract relaxation times of samples.

The last part of this work presents all the experimental and simulation steps followed to implement an MRF-based sequence for low-field NMR.

First acquisitions in laboratory were conducted to confirm the necessity to extract a complete information about the magnetic fields correlation map. In fact, the influence of the B_1 is directly correlated with the B_0 distribution and cannot be understood and extracted separately with respect to the off-resonance information. Then the simulation investigation is reported. This was conducted in Matlab and it was useful to better understand how to study the correlation map using ANGLE experiment and on what range of parameters basing all subsequent experimental acquisitions. At the end all acquisitions conducted with the rubber sample are reported. All results were correctly validated by MARSS simulations, confirming the success of them: an MRF-based sequence was correctly implemented on low-field NMR devices.

The use of sequences such as MRF-based, with a multiparametric analysis allows to understand and to simultaneously quantify several material properties in reasonable

scan time (the intrinsic relaxation times in the case of this thesis work). Moreover this approach provides a more robust answer in the presence of noise or other acquisitions errors, thanks to the post processing with pattern recognition algorithms.

So far, MRF has been only applied on high-field NMR for clinical purpose. This is due to the increasing interest in multiparametric quantitative imaging. For example, it could represent a useful support to diagnosis, which is traditionally conducted by a qualitative assessment. In fact, to correctly characterize a pathology is often necessary to apply multiparametric protocols [28], and the MRF approach provides these measurements. This technique could also be used for tissue characterization, follow-up, and therapeutic assessment [2].

This thesis presents the first MRF application in NMR laboratory. Obviously all this work must be considered taking into account the experimental limitations, linked for example to KEA console and to the impossibility to program sequences with a long series of pulses. While the clinical scanners and coils don't have these limitations, and they allow to design MRF sequences based on a long series of pulses and with a very long acquisition time.

Moreover, the difficulties to manage inhomogeneous fields in small volumes, and the necessity to individuate a method to extract the influences of these magnetic fields on samples and their correlation may represent the most difficult and stimulant challenge of this work. In the presence of inhomogeneous magnetic fields, relaxation times and diffusion coefficients are the key NMR parameters to assess sample composition and dynamics. This developed technique allows to simultaneously extract these parameters at NMR low field. The MRF sequence can be applied in diverse fields such as the non-destructive testing of rubber and polymer products and food analysis, as well as the state assessment of objects of cultural heritage [62].

Finally, another interesting challenge was to correctly design the desired sequences on the KEA console, both MRF-based sequence, and preparatory ones.

There are several continuations of this work. For example, a first way consists in continuing MRF acquisitions, maybe using other samples, developing a robust signal dictionary for each sample, and programming an efficient pattern recognition algorithm that will find and match in the dictionary the fingerprint evolution signal, individuating all parameters of interest.

In addition, the KEA console has a limitation on the number of parameters that can be written into memory to program a sequence. In fact, in the MRF sequence implemented in this work, the number of designed pulses was 96. Another possible development is represented by the identification of a strategy for designing an MRF sequence based on a larger number of pulses.

Another interesting development can be represented by finding an alternative method to extract information on $B_0 - B_1$ correlation maps. Maybe directly using bSSFP sequences, avoiding the necessity to firstly acquire an ANGLE signal.

Eventually, once validated these type of results, that can be always developed using a constant magnetic field device, the natural continuation of this work is represented to the capacity to translate all these results on more complex sensors, such as single-sided ones,

e.g., the MOUSE, to conduct investigation in the area of biological tissue or material science and quality control [62].

Appendix A

KEA-II NMR designed sequences

Here, as an example, the most important KEA sequence designed and programmed is reported and commented: the MRF based sequence. The other KEA sequences programmed (ANGLE, constant and alternate bSSFP) were implemented starting from some similar sequences already existing, modifying them in order to acquire the signal from the experiment of interest. Only limited parts of codes are reported because scripts can be very long and it is interesting to point out only some specific line which are characteristic for the sequence you are programming.

As said in Section 3.3.5, the MRF sequence was amplitude based and not pulse length based. This means that for each pulse is defined the attenuation in amplitude, fixing other parameters, such as the pulse length ($6 \mu s$ in this case). This sequence was designed considering a flip angle pattern, showed in Figure 3.31, and for each flip angle the attenuation was derived using the Equation 3.3. These amplitude values with delays and other parameters must be all defined in the .mac file in the relationship part, as following:

```
1 # Relationships between pulse-sequence and GUI parameters
2   relationships = ["a1 = 180Amplitude",
3                   "d1 = pulseLength",
4                   "a2 = -37.4093",
5                   "a3 = -34.0348",
6
7                   "...",
8                   "...",
9                   "...",
10
11                  "d97 = 1000/2 - acqTime*500 - d1/2 + rxLat + echoShift",
12                  "d98 = 1000 - d1 - pgo - d97",
13                  "w1 = 1",
14                  "d99 = 300000",
15                  "n1 = nrEchoes",
16                  "n2 = nrPnts",
17                  "echoTime = 100",
18                  "nb_totPnts = nrPnts*nrEchoes",
```

```

19         "totTime = nrEchoes*echoTime "]
20
21 # These parameters will be changed between experiments
22     variables = [" "]

```

where, in this case, 96 attenuation in amplitude are defined, with correspondent delays and acquisition time windows. Then, the other interesting part of the .mac file is where the list of pulses is defined and it follows a structure like the one below:

```

1 # Pulse sequence
2   initpp(dir) # Reset internal parameter list
3   cleardata(64000)
4   pulse(mode,a1,p1,d1)
5
6   wait(w1)
7
8   pulse(mode,a2,p2,d1)
9   delay(d97)
10  acquire("append",n2,d98)
11
12  ...
13  ...
14  ...
15
16  lst = endpp() # Return parameter list

```

where, for example, the first pulse represent the 180° pulse, and then, after a delay, a pulse train is applied, where pulses alternate with delays and acquisition windows.

The .mac script is finished with the phase cycle and the `endproc` command.

Initial parts of the .bak file are used to define e.g., what parameters enter in the GUI windows, where enter them and the range of allowed values. Then, some specific build-in functions of Prospa are used to run the pulse program, collect data, accumulate, plot and save data.

Code lines are generally interspersed with some checking command, used to avoid to run a sequence that can damage experimental devices.

Here some lines of a .bak file are reported as example. What is important is the structure of this part of the code. Then, according to the sequence, specific lines are designed.

```

1   # Set phases for this scan
2   (ppList,pAcq) = keaRun:setPPPphase(ppList,scan,pcList,pcIndex)
3
4
5   # Run the pulse program and collect the data
6   (status,data) = keaRun:getData(nb_totPnts,guipar)
7
8   if(status != "ok")
9       return(0)
10  endif

```

```

11
12 # Accumulate the data
13   sumData = keaRun:accumulate(accumulate,pAcq,sumData,data)
14
15   ...
16   ...
17   ...
18
19 # Integrate each echo
20   for(ec = 0 to (nrEchoes)-1)
21     MagData[ec] = sum(mag(echoData2D[~,ec])/nrPnts)
22   next(ec)
23
24   ...
25   ...
26   ...
27
28 # Save the data
29   keaFiles:save1DData(guipar,TRindex,MagData/scan)
30
31   ...
32   ...

```

Hence, for example, here `MagData` represent magnitude data of MRF acquired signal. All data can also be plotted with a specific build-in function.

At the end of the script there is the command `endproc("execpp")` which finishes all procedures.

Appendix B

MARSS sequences

Here are reported examples of the MARSS codes for some sequence analyzed. Also in this case, it is not interesting reporting all codes, because for example, the first section where the sample is loaded and created is always the same. Also the section related to the receiver is always the same, where the standard 2 channel phd is typically selected.

The parts related to the sequence parameters setting have the same parameters for FID 1-Pulse and bSSFP except for the function selected to make the sequence and the parameter `nb_echoes` present in the steady state sequences, which indicates the number of echoes acquired from the CPMG sequence. An example of code for this section, considering the constant bSSFP sequence is shown below.

```
1 %% — — — — Setting Sequence parameters — — — — %%
2 rd = 2.5;
3 p1 = pi/9;
4 TR = 100*10^-6; % Relaxation delay [s]
5 tau = TR; % Echo-time [s]
6 nphsc = 1;
7 phase1 = 0;
8 cphs = 2;
9 nb_echoes = 40000; % Number of echoes acquired from the CPMG sequence
   = number of 180 pulses.
10 % Creating CPMG sequence using MakeSequence Function
11 sequence = Make_SSFP(nb_echoes , p1 , nphsc , cphs , phase1 , TR);
```

For the alternate bSSFP, the phase cycle changes, considering the alternation of each pulse (i.e., the first one is for example 90° , the second one is -90° , the third one is again 90° , and so on).

Considering the ANGLE case it is necessary to specify the value of B_1 , which is fixed for this experiment and some other parameter, like the total duration of the sequence.

```
1 %% — — — — Setting Sequence Parameters — — — — %%
2 rd = 10;
3 % Set pulse length for the 90 PULSE and compute B1 intensity which
   will be fixed for the experiment
4 gamma = 42.58*10^6; % Gyromagnetic ratio
```

```

5 pw = pi/2; % 90 pulse
6 pl_90 = 6*10^-6; % Pulse length of 90 pulse [s]
7 B1 = (pw/(2*pi))/(gamma*pl_90); % Fixed
8 %dwell_pulse = (1*10^-6)/100; %[s]
9
10 % Define parameter for the 2D experiment
11 pl_start = 0.5*10^-6; %[s]
12 pl_step = 9.32e-6; %[s]
13 pl_nb_steps = round((96*pl_90)/pl_step); % Total duration
14 pls = pl_start:pl_step:pl_step*pl_nb_steps;
15 % Define phase cycling
16 nphsc = 4;
17 phasc = [0;1;2;3];

```

These parameters are explained in Section 3.2.1.

The MRF sequence instead needs two function, because is based on an IR-bSSFP. Moreover, there is a flip angle pattern to follow for the pulses. The TR instead is fixed, so, what changes is shown below.

```

1 RFPulses = dlmread('MRF_pulsePattern/FA_pattern.txt'); % Read a flip
    angle pattern document
2 RFPulses = RFPulses(1:nb_echoes);
3 TR = 100e-6.*ones(1,length(RFPulses));
4 t_recovery = 10e-6;
5 % Creating sequence functions
6 IRpulse = Make_S1P(pi, nphsc, cphs, phase1, t_recovery);
7 sequence = Make_randomSSFP(nb_echoes, RFPulses, nphsc, cphs, phase2, TR)
    ;

```

Other parameters for the steady state sequence are the same.

Then, there is the signal acquisition parameters section, where the dwell (time delay between two adjacent sampled point), the FID duration, the vectors related to the time, to the real and to the imaginary part of the signal and other parameters are set. An example is reported below, for the FID sequence:

```

1 %% — — — Setting Signal Acquisition Parameters — — — %%
2 % Define FID acquisition parameters
3 dt = 5*10^-6; % time delay between two adjacent sampled point [s]
4 FID_duration = dt*4096; %[s]
5 FID_points = int32(FID_duration/dt);
6 t = linspace(0,FID_duration,FID_points);
7 u = linspace(0,0,FID_points); % Re
8 v = linspace(0,0,FID_points); % Im
9 FID = [u;v];
10 % Define SNR
11 SNR = 100;
12 % Define scans
13 ds = 0; % dummy scans
14 ns = 8; % number of sampled scan.

```

If you want add noise or dummy scans you can select the values in this section. The number of scans are also specified.

At this point, there is the part related to the experiment. It changes regarding the sequence, but there is always a relaxation of the sample, a preallocation of the magnetization vector and then, using different specific functions, the experiment is simulated. An example of the code is reported for the MRF sequence:

```

1 % Control statement to avoid errors
2 if ac_wind > tau
3     error('ac_wind must be <= tau');
4 end
5 % Relax sample
6 sample = RelaxSample(sample);
7 % Prealloc magnetization vector
8 MAG = zeros(3, sample.NMc);
9 for j = 1:sample.NMc
10     MAG(:,j) = sample.Mc(j).M;
11 end
12 % MRF experiment
13 for nscan=1:(ns+ds)
14     % Apply the IR pulse and free evolve for t_recovery
15     [sample,MAG] = Sequence2Sample(sample,MAG,IRpulse,nscan);
16     % Apply the Preamble pulse of SSFP
17     [sample,FID] = PULSEtrain2Sample(sample,MAG,sequence,nscan
18         ,...
19         nb_points,ac_wind,dwell,FID,ds,rx);
20     % Recycle delay
21     FE_rec = createFreeEvolutionMatrix(sample,rd);
22     rec = createRecVec(sample,rd);
23     for k=1:sample.NMc
24         MAG(:,k) = FE_rec(:,:,k)*MAG(:,k)+rec(:,k);
25     end
26 end
27 % Plotting
28 plot(TR_index,sqrt(FID(1,:).*FID(1,:)+FID(2,:).*FID(2,:))/ns);
29 xlabel('TR index');
30 ylabel('Signal Intensity (a.u.)');
31 % Saving
32 save(strcat(save_folder,'MRF'),'TR_index','FID');
```

At the end, the signal is plotted and the data are saved in the specific folder.

Bibliography

- [1] D. Ma, V. Gulani, N. Seiberlich, K. Liu, J. L. Sunshine, J. L. Duerk, and M. A. Griswold, “Magnetic resonance fingerprinting,” *Nature*, vol. 495, pp. 187–192, Mar. 2013.
- [2] B. B. Mehta, S. Coppo, D. F. McGivney, J. I. Hamilton, Y. Chen, Y. Jiang, D. Ma, N. Seiberlich, V. Gulani, and M. A. Griswold, “Magnetic resonance fingerprinting: A technical review,” *Magn Reson Med.*, vol. 81, pp. 25–46, Jan. 2019. DOI: 10.1002/mrm.27403.
- [3] R. Wood, K. Bassett, and V. Foerster. (2011). “1.5 tesla magnetic resonance imaging scanners compared with 3.0 tesla magnetic resonance imaging scanners: Systematic review of clinical effectiveness: Pilot project [internet]. ottawa (on): Canadian agency for drugs and technologies in health; introduction,” [Online]. Available: <https://www.ncbi.nlm.nih.gov/books/NBK174468/>.
- [4] I. I. Rabi, J. R. Zacharias, S. Millman, and P. Kusch, “A new method of measuring nuclear magnetic moment,” *Phys. Rev.*, vol. 53, pp. 318–318, 4 Feb. 1938. DOI: 10.1103/PhysRev.53.318. [Online]. Available: <https://link.aps.org/doi/10.1103/PhysRev.53.318>.
- [5] N. media AB. (2020). “The nobel prize in physics 1944.,” [Online]. Available: <https://www.nobelprize.org/prizes/physics/1944/summary/>.
- [6] E. M. Purcell, H. C. Torrey, and R. V. Pound, “Resonance absorption by nuclear magnetic moments in a solid,” *Phys. Rev.*, vol. 69, pp. 37–38, 1-2 Jan. 1946. DOI: 10.1103/PhysRev.69.37. [Online]. Available: <https://link.aps.org/doi/10.1103/PhysRev.69.37>.
- [7] F. Bloch, W. W. Hansen, and M. Packard, “Nuclear induction,” *Phys. Rev.*, vol. 69, pp. 127–127, 3-4 Feb. 1946. DOI: 10.1103/PhysRev.69.127. [Online]. Available: <https://link.aps.org/doi/10.1103/PhysRev.69.127>.
- [8] N. media AB. (2020). “The nobel prize in physics 1952.,” [Online]. Available: <https://www.nobelprize.org/prizes/physics/1952/summary/>.
- [9] P. A. M. Dirac, *The Principles of Quantum Mechanics*, ser. International series of monographs on physics. Clarendon Press, 1981, ISBN: 9780198520115.

- [10] E. L. Hahn, "Spin echoes," *Phys. Rev.*, vol. 80, pp. 580–594, 4 Nov. 1950. DOI: 10.1103/PhysRev.80.580. [Online]. Available: <https://link.aps.org/doi/10.1103/PhysRev.80.580>.
- [11] R. Ernst, G. Bodenhausen, and A. Wokaun, *Principles of Nuclear Magnetic Resonance in One and Two Dimensions*, ser. International Series of Monographs on Chemistry. Oxford University Press, 1990, ISBN: 9780198556473.
- [12] R. Kaiser, E. Bertholdi, and R. R. Ernst, "Diffusion and field gradient effects in nmr fourier spectroscopy," *J. Chem. Phys.*, vol. 60, 1974. DOI: 10.1063/1.1681477. [Online]. Available: <http://dx.doi.org/10.1063/1.1681477>.
- [13] M. Hürlimann, "Diffusion and relaxation effects in general stray field nmr experiments," *Journal of Magnetic Resonance*, vol. 148, no. 2, pp. 367–378, 2001, ISSN: 1090-7807. DOI: <https://doi.org/10.1006/jmre.2000.2263>. [Online]. Available: <http://www.sciencedirect.com/science/article/pii/S1090780700922638>.
- [14] Y.-Q. Song, "Categories of coherence pathways for the cpmg sequence," *Journal of Magnetic Resonance*, vol. 157, no. 1, pp. 82–91, 2002, ISSN: 1090-7807. DOI: <https://doi.org/10.1006/jmre.2002.2577>. [Online]. Available: <http://www.sciencedirect.com/science/article/pii/S1090780702925772>.
- [15] D. L. Logan, *A First Course in the Finite Element Method*. Cl-Engineering, 2010, ISBN: 978-0495668251.
- [16] D. Hoult and R. Richards, "The signal-to-noise ratio of the nuclear magnetic resonance experiment," *Journal of Magnetic Resonance (1969)*, vol. 24, no. 1, pp. 71–85, 1976, ISSN: 0022-2364. DOI: [https://doi.org/10.1016/0022-2364\(76\)90233-X](https://doi.org/10.1016/0022-2364(76)90233-X). [Online]. Available: <http://www.sciencedirect.com/science/article/pii/002223647690233X>.
- [17] D. P. Weitekamp, J. R. Garbow, J. B. Murdoch, and A. Pines, "High-resolution nmr spectra in inhomogeneous magnetic fields: Application of total spin coherence transfer echoes," *Journal of the American Chemical Society*, vol. 103, no. 12, pp. 3578–3579, 1981. DOI: 10.1021/ja00402a057. [Online]. Available: <https://doi.org/10.1021/ja00402a057>.
- [18] C. A. Meriles, D. Sakellariou, H. Heise, A. J. Moulé, and A. Pines, "Approach to high-resolution ex situ nmr spectroscopy," *Science*, vol. 293, no. 5527, pp. 82–85, 2001, ISSN: 0036-8075. DOI: 10.1126/science.1061498. eprint: <https://science.sciencemag.org/content/293/5527/82.full.pdf>. [Online]. Available: <https://science.sciencemag.org/content/293/5527/82>.
- [19] B. Shapira and L. Frydman, "Spatial encoding and the acquisition of high-resolution nmr spectra in inhomogeneous magnetic fields," *Journal of the American Chemical Society*, vol. 126, no. 23, pp. 7184–7185, 2004. DOI: 10.1021/ja048859u. [Online]. Available: <https://doi.org/10.1021/ja048859u>.

- [20] A. Jerschow, "Multiple echoes initiated by a single radio frequency pulse in nmr," *Chemical Physics Letters*, vol. 296, no. 5, pp. 466–470, 1998, ISSN: 0009-2614. DOI: [https://doi.org/10.1016/S0009-2614\(98\)01032-X](https://doi.org/10.1016/S0009-2614(98)01032-X). [Online]. Available: <http://www.sciencedirect.com/science/article/pii/S000926149801032X>.
- [21] D. Topgaard, D. Sakellariou, and A. Pines, "Nmr spectroscopy in inhomogeneous b0 and b1 fields with non-linear correlation," *Journal of Magnetic Resonance*, vol. 175, no. 1, pp. 1–10, 2005, ISSN: 1090-7807. DOI: <https://doi.org/10.1016/j.jmr.2005.03.006>. [Online]. Available: <http://www.sciencedirect.com/science/article/pii/S1090780705000698>.
- [22] C. A. Meriles, D. Sakellariou, and A. Pines, "Broadband phase modulation by adiabatic pulses," *Journal of Magnetic Resonance*, vol. 164, no. 1, pp. 177–181, 2003, ISSN: 1090-7807. DOI: [https://doi.org/10.1016/S1090-7807\(03\)00157-5](https://doi.org/10.1016/S1090-7807(03)00157-5). [Online]. Available: <http://www.sciencedirect.com/science/article/pii/S1090780703001575>.
- [23] D. Sakellariou, C. A. Meriles, and A. Pines, "Advances in ex-situ nuclear magnetic resonance," *Comptes Rendus Physique*, vol. 5, no. 3, pp. 337–347, 2004, Highly polarized nuclear spin systems and dipolar interactions in NMR, ISSN: 1631-0705. DOI: <https://doi.org/10.1016/j.crhy.2004.03.016>. [Online]. Available: <http://www.sciencedirect.com/science/article/pii/S1631070504000684>.
- [24] S. Antonijevic and S. Wimperis, "High-resolution nmr spectroscopy in inhomogeneous b0 and b1 fields by two-dimensional correlation," *Chemical Physics Letters*, vol. 381, no. 5, pp. 634–641, 2003, ISSN: 0009-2614. DOI: <https://doi.org/10.1016/j.cplett.2003.09.116>. [Online]. Available: <http://www.sciencedirect.com/science/article/pii/S000926140301697X>.
- [25] W. Roetzel, X. Luo, and D. Chen, "Chapter 6 - optimal design of heat exchanger networks," in *Design and Operation of Heat Exchangers and their Networks*, W. Roetzel, X. Luo, and D. Chen, Eds., Academic Press, 2020, pp. 231–317, ISBN: 978-0-12-817894-2. DOI: <https://doi.org/10.1016/B978-0-12-817894-2.00006-6>. [Online]. Available: <http://www.sciencedirect.com/science/article/pii/B9780128178942000066>.
- [26] V. Demas, D. Sakellariou, C. A. Meriles, S. Han, J. Reimer, and A. Pines, "Three-dimensional phase-encoded chemical shift mri in the presence of inhomogeneous fields," *Proceedings of the National Academy of Sciences*, vol. 101, no. 24, pp. 8845–8847, 2004, ISSN: 0027-8424. DOI: 10.1073/pnas.0403016101. eprint: <https://www.pnas.org/content/101/24/8845.full.pdf>. [Online]. Available: <https://www.pnas.org/content/101/24/8845>.
- [27] A. Janowczyk and A. Madabhushi, "Deep learning for digital pathology image analysis: A comprehensive tutorial with selected use cases," *Journal of Pathology Informatics*, vol. 7, no. 29, 2016. [Online]. Available: <https://www.jpathinformatics.org/text.asp?2016/7/1/29/186902>.

- [28] A. C. Yu, C. Badve, and L. E. Ponsky, "Development of a combined mr fingerprinting and diffusion examination for prostate cancer," *Radiology*, vol. 283, no. 3, pp. 729–738, Jun. 2017. DOI: 10.1148/radiol.2017161599.
- [29] D. Look and D. Locker, "Time saving in measurement of nmr and epr relaxation times," *Review of Scientific Instruments*, vol. 41, pp. 250–251, Feb. 1970. DOI: 10.1063/1.1684482.
- [30] N. Stikov and M. Boudreau, "On the accuracy of t1 mapping: Searching for common ground," *Magn Reson Med.*, vol. 73, no. 2, Feb. 2015. DOI: 10.1002/mrm.25135.
- [31] S. Majumdar and S. Orphanoudakis, "Errors in the measurements of t2 using multiple-echo mri techniques. ii. effects of static field inhomogeneity," *Magn Reson Med.*, vol. 3, no. 4, Aug. 1986. DOI: 10.1002/mrm.1910030410.
- [32] A. Crawley and R. Henkelman, "A comparison of one-shot and recovery methods in t1 imaging," *Magnetic resonance in medicine*, vol. 7, no. 1, pp. 23–34, May 1988, ISSN: 0740-3194. DOI: 10.1002/mrm.1910070104. [Online]. Available: <https://doi.org/10.1002/mrm.1910070104>.
- [33] C. Testa and L. Brizi, *Lecture notes of the course "Physics in Neuroscience and Medicine"*. 2017.
- [34] J. Perlo, F. Casanova, and B. Blümich, "Profiles with microscopic resolution by single-sided nmr," *Journal of Magnetic Resonance*, vol. 176, no. 1, pp. 64–70, 2005, ISSN: 1090-7807. DOI: <https://doi.org/10.1016/j.jmr.2005.05.017>. [Online]. Available: <https://www.sciencedirect.com/science/article/pii/S1090780705001825>.
- [35] K. Scheffler and L. Stefan, "Principles and applications of balanced ssfp techniques," *European radiology*, vol. 13, 2003. DOI: 10.1007/s00330-003-1957-x.
- [36] J. Assländer, "Pseudo steady-state free precession for mr-fingerprinting," *Magnetic resonance in medicine*, vol. 77, pp. 1151–1161, 2017. DOI: 10.1002/mrm.26202.
- [37] B. Rieger, "Magnetic resonance fingerprinting using echo-planar imaging: Joint quantification of t1 and t2* relaxation times.," *Magnetic resonance in medicine*, vol. 78, 2017. DOI: 10.1002/mrm.26561.
- [38] Y. Jiang, D. Ma, N. Seiberlich, V. Gulani, and M. A. Griswold, "Mr fingerprinting using fast imaging with steady state precession (fisp) with spiral readout.," *Magnetic resonance in medicine*, vol. 74, no. 6, 2015. DOI: 10.1002/mrm.25559.
- [39] J. Hennig, "Echoes - how to generate, recognize, use or avoid them in mr-imaging sequences. part i: Fundamental and not so fundamental properties of spin echoes," *Concepts in Magnetic Resonance*, vol. 3, no. 3, pp. 125–143, Jul. 1991. DOI: 10.1002/cmr.1820030302.
- [40] J. I. Hamilton, Y. Jiang, Y. Chen, D. Ma, W.-C. Lo, M. Griswold, and N. Seiberlich, "Mr fingerprinting for rapid quantification of myocardial t1, t2, and proton spin density magn reson med.," *Magn Reson Med.*, vol. 77, no. 4, pp. 1446–1458, Apr. 2017. DOI: 10.1002/mrm.26216.

- [41] B. Zhao, K. Setsompop, H. Ye, S. F. Cauley, and L. L. Wald, "Maximum likelihood reconstruction for magnetic resonance fingerprinting," *IEEE Transactions on Medical Imaging*, vol. 35, no. 8, pp. 1812–1823, 2016. DOI: 10.1109/TMI.2016.2531640.
- [42] B. Zhao, "Model-based iterative reconstruction for magnetic resonance fingerprinting," in *2015 IEEE International Conference on Image Processing (ICIP)*, 2015, pp. 3392–3396. DOI: 10.1109/ICIP.2015.7351433.
- [43] D. McGivney, E. Pierre, and D. Ma, "Svd compression for magnetic resonance fingerprinting in the time domain.," *IEEE Trans Med Imaging.*, vol. 33, no. 12, pp. 2311–2322, 2014. DOI: 10.1109/TMI.2014.2337321.
- [44] E. J. Candès, J. K. Romberg, and T. Tao, "Stable signal recovery from incomplete and inaccurate measurements," *Communications on pure and applied mathematics*, vol. 59, no. 8, pp. 1207–1223, Aug. 2006. DOI: 10.1002/cpa.20124.
- [45] Z. Yu, T. Zhao, J. Assländer, R. Lattanzi, D. K. Sodickson, and M. A. Cloos, "Exploring the sensitivity of magnetic resonance fingerprinting to motion," *Magn Reson Imaging.*, vol. 54, pp. 241–248, Dec. 2018. DOI: 10.1016/j.mri.2018.09.002.
- [46] D. McGivney, A. Deshmane, D. Ma, C. Badve, A. Sloan, V. Gulani, and M. Griswold, "Bayesian estimation of multicomponent relaxation parameters in magnetic resonance fingerprinting.," *Magnetic resonance in medicine*, vol. 80, no. 1, pp. 159–170, 2018. DOI: 10.1002/mrm.27017.
- [47] S. F. Cauley, K. Setsompop, and D. Ma, "Fast group matching for mr fingerprinting reconstruction.," *Magn Reson Med.*, no. 74, pp. 523–528, 2015.
- [48] O. Cohen and M. S. Rosen, "Algorithm comparison for schedule optimization in mr fingerprinting.," *Magnetic resonance imaging*, vol. 41, pp. 15–21, 2017. DOI: 10.1016/j.mri.2017.02.010.
- [49] J. Hamilton, K. L. Wright, and Y. Jiang, "Pulse sequence optimization for improved mrf scan efficiency," in *23rd Annual Meeting of ISMRM, Toronto, Canada*, 2015, p. 3386.
- [50] J. H. Duyn, Y. Yang, J. A. Frank, and J. W. van der Veen, "Simple correction method for k-space trajectory deviations in mri.," *Magn Reson.*, vol. 132, no. 1, pp. 150–153, 1998. DOI: 10.1006/jmre.1998.1396.
- [51] H. Tan and C. H. Meyer, "Estimation of k-space trajectories in spiral mri.," *Magn Reson Med.*, vol. 61, no. 6, pp. 1396–1404, 2009. DOI: 10.1002/mrm.21813.
- [52] M. Barbieri, L. Brizi, V. Bortolotti, P. Fantazzini, S. Sykora, and C. Testa, "A flexible software for nmr pulse sequence simulations, first applications to mr-fingerprinting: Quantification of myelin water fraction in white matter and diffusion coefficient measurement," *ISMRM Workshop series 2017, Magnetic Resonance Fingerprinting*, p. 11, 2017.
- [53] O. Bieri and K. Scheffler, "Fundamentals of balanced steady state free precession mri," *Journal of magnetic resonance imaging (JMRI)*, vol. 38, no. 1, pp. 2–11, 2013. DOI: 10.1002/jmri.24163.

- [54] C. Ganter, "Off-resonance effects in the transient response of ssfp sequences," *Magnetic resonance in medicine*, vol. 52, no. 2, pp. 368–375, 2004. DOI: 10.1002/mrm.20173.
- [55] G. Borgia, R. Brown, and P. Fantazzini, "Uniform-penalty inversion of multiexponential decay data: Data spacing, t2 data, systematic data errors, and diagnostics," *Journal of Magnetic Resonance*, vol. 147, no. 2, pp. 273–285, Dec. 2000.
- [56] R. Brown, G. Borgia, and P. Fantazzini, "Uniform-penalty inversion of multiexponential decay data," *Journal of Magnetic Resonance*, vol. 132, no. 1, pp. 65–77, May 1998.
- [57] R. Stollberger, P. Wach, G. McKinnon, E. Justich, and F. Ebner, "Rf-field mapping in vivo," English, Society of Magnetic Resonance in Medicine; 7th Annual Scientific Meeting and Exhibition ; Conference date: 23-05-1988 Through 28-05-1988, 1988.
- [58] C. Cunningham, J. Pauly, and K. Nayak, "Saturated double-angle method for rapid b1+ mapping," *Magnetic Resonance Medicine*, vol. 55, no. 6, pp. 1326–1333, Jun. 2006. DOI: 10.1002/mrm.20896.
- [59] R. J. Hyndman and A. B. Koehler, "Another look at measures of forecast accuracy," *International Journal of Forecasting*, vol. 22, no. 4, pp. 679–688, 2006. DOI: 10.1016/j.ijforecast.2006.03.001.
- [60] R. Pontius, O. Thontteh, and H. Chen, "Components of information for multiple resolution comparison between maps that share a real variable," *Environmental Ecological Statistics*, vol. 15, no. 2, pp. 111–142, 2008. DOI: 10.1007/s10651-007-0043-y.
- [61] F. Zhao, Z. Ping, S. Zhao, Y. Jian, and W. Kuhn, "Characterization of elastomer networks by nmr parameters part ii 1: Influence of accelerators on nr vulcanizates," *KGK Kautschuk Gummi Kunststoffe*, vol. 60, pp. 685–688, Dec. 2007.
- [62] F. Casanova, J. Perlo, and B. Blümich, *Single-Sided NMR*. Springer-Verlag Berlin Heidelberg, 2011, ISBN: 978-3-642-16307-4.
- [63] A. D. Elster. (2020). "Questions and answers in mri," [Online]. Available: <http://mriquestions.com/index.html>.
- [64] Magritek Ltd, *Prospa Programming Manual (V 3.11)*. 2012.